CHARACTERIZATION OF AN ELECTROMAGNETIC TUNED VIBRATION ABSORBER

Lawrence B. Tentor

Dissertation submitted to the Faculty of the
Virginia Polytechnic Institute and State University
in partial fulfillment of the requirements for the degree of

Doctorate of Philosophy
in
Mechanical Engineering

Dr. Alfred Wicks, Chair
Dr. Mehdi Ahmadian
Dr. Harley H. Cudney
Dr. Daniel J Inman
Dr. Harry Robertshaw

August 2001
Blacksburg, Virginia

Copyright 2000-2001, Lawrence B. Tentor

Keywords: Tuned Vibration Absorber, Electromagnetic Fields

Characterization of an Electromagnetic Tuned Vibration Absorber

Lawrence B. Tentor

(ABSTRACT)

Tuned vibration absorbers (TVA) have been discussed in literature since the early twentieth century. These devices are implemented to suppress the system's vibration by transferring energy to the absorber mass. This research examines an electromagnetic tuned vibration absorber that can have its tuned frequency altered by gap and current variation. The advantage of an adjustable TVA is that the system can be tuned to various excitation frequencies to cancel vibration. This research examines a unique embodiment using permanent magnets and an electromagnetic absorber to alter the system dynamics. The focus is to allow changes in tuned frequency to cancel system vibrations. This research develops the electromagnetic theory, presents absorber system simulations, and tests the dynamic absorber's response.

The electromagnetic field is investigated to determine the field between a stationary magnet and the absorber electromagnet. This field can be numerically calculated as the superposition of four constituent fields. With the electromagnetic field determined, the force to displacement relation between the stationary magnet and the absorber electromagnet is calculated. The best fit is determined to be an inverse square relationship. Once the spring force relation is determined, the damping mechanisms are discussed and experiments proposed to isolate the different damping mechanisms. In the simulations, it is found that by having an adjustable electromagnetic TVA the natural frequency can be adjusted 2-3% with a +10 amp input and over 50% for a variable gap. The advantage of the variable gap is that it may be adjusted once and then no additional energy is needed, while the advantage of the variable current is that the system may be rapidly altered.

The experiments are undertaken to test the constructed absorber for the spring and damping force. The tests confirm the spring force relation and quantify the high damping present in the tested configuration. Then the absorber system transfer functions are recorded. The absorber is then applied to a single degree of freedom system to verify its cancellation results by a gap variation.

CONTENTS

LIST OF FIGURES III

ACKNOWLEDGMENTS VII

CHAPTER 1. INTRODUCTION 1

PROBLEM EXAMINED: MAGNETIC TUNED VIBRATION ABSORBER 3
DISSERTATION OUTLINE 5

CHAPTER 2. TVA FUNDAMENTALS & LITERATURE REVIEW 7

TVA FUNDAMENTALS 7
Primary System (Single DOF) 7
Primary System with TVA (Combined System) 8
PASSIVE TUNED VIBRATION ABSORBERS 13
SEMI-ACTIVE TUNED VIBRATION ABSORBERS 15
Semi-Active Variable Inertia TVAs 15
Semi-Active Variable Stiffness TVAs 15
Semi-Active Variable Damping 17
ACTIVE TUNED VIBRATION ABSORBERS 18
SUMMARY 20

CHAPTER 3. ELECTROMAGNETIC FIELD FORMULATION 21

SYSTEM CONFIGURATION 21
MAGNETIC FLUX DENSITY DERIVATION 23
Magnetic Flux Density from Elemental Loop 24
Magnetic Flux Density from Current Carrying Coil 27
Magnetic Flux Density from Core within Current Carrying Coil 29
Magnetic Flux Density from Permanent Magnet Attached to Core 32
Magnetic Flux Density from Stationary Permanent Magnet 36
Total Magnetic Flux Density 39
SUMMARY 42

CHAPTER 4. ELECTROMAGNETIC FORCE FORMULATION 43

FORCE DERIVATION FROM MAGNETIC FLUX DENSITY 43
FORCE ON VIBRATION ABSORBER 44
Force Level with Current Variation 48
Dual-Sided Absorber Force 49
Force Levels with Variable Gap Spacing 52
SUMMARY 55

CHAPTER 5. DAMPING MECHANISMS 56

MECHANICAL DAMPING 56

Experimental Test 57
ELECTROMAGNETIC DAMPING 58
Experimental Test 61
DAMPING SUMMARY 61
CHAPTER 6. SYSTEM SIMULATION 63
LINEAR SYSTEM SIMULATION 63
NONLINEAR SYSTEM SIMULATION 65
Variable Base Excitation 66
Variable Current 69
Variable Gap 73
Higher Order Harmonics 79
SIMULATION SUMMARY 82
CHAPTER 7. SYSTEM DESIGN AND INITIAL TESTING 83
SYSTEM DESIGN 83
FORCE RELATIONSHIP 84
DAMPING RELATIONSHIP 90
Damping Experiments for Mechanical Springs 91
Damping Experiments for Beam with Magnets 93
SUMMARY 96
CHAPTER 8. TVA DESIGN EQUATIONS AND TUNING 98
DESIGN EQUATIONS FOR MINIMUM RESPONSE 98
SYSTEM TESTING FOR VARIABLE GAPS 107
CONCLUSIONS 114
CHAPTER 9. SYSTEM DYNAMIC TESTING 115
SDOF EXPERIMENTS 115
Variable Gap 116
Simulations with Experimental Force Relationship 120
SDOF System with Current Variations 124
2-DOF EXPERIMENTS 127
SUMMARY 136
CHAPTER 10. CONCLUSIONS 137
THEORETICAL WORK 137
EXPERIMENTAL WORK 138
FUTURE WORK 138
SUMMARY 138
REFERENCES 140

List of figures

Number *Page*

Figure 1: Passive TVA Configuration 1
Figure 2: Semi-active TVA Configuration 2
Figure 3: Active TVA Configuration 3
Figure 4: Investigated configuration 4
Figure 5: Primary System, One Degree of Freedom 7
Figure 6: Primary System Frequency Response Function 8
Figure 7: Combined System 9
Figure 8: Primary & Combined System Frequency Response Function 11
Figure 9: Primary & Combined System Frequency Response Function 12
Figure 10: Variable Stiffness Viscously Damped Combined System 16
Figure 11: Proposed System Configuration 22
Figure 12: Simplified System Diagram 22
Figure 13: Elemental Loop Configuration 24
Figure 14: Radial Magnetic Flux Density from Current Carrying Loop 25
Figure 15: Axial Magnetic Flux Density from Current Carrying Loop 26
Figure 16: Magnetic Flux Density Field from Current Carrying Loop 26
Figure 17: Radial Magnetic Flux Density from Current Carrying Coil 28
Figure 18: Axial Magnetic Flux Density from Current Carrying Coil 28
Figure 19: Vector Field of Magnetic Flux Density from Current Carrying Coil 29
Figure 20: Radial Magnetic Flux Density from Core within Current Carrying Coil 31
Figure 21: Axial Magnetic Flux Density from Core within Current Carrying Coil 31
Figure 22: Vector Field of Magnetic Flux Density from Core within Current Carrying Coil 32
Figure 23: Radial Magnetic Flux Density from Permanent Magnet Attached to Core 34
Figure 24: Axial Magnetic Flux Density from Permanent Magnet Attached to Core 35
Figure 25: Vector Field of Magnetic Flux Density from Permanent Magnet Attached to Core36
Figure 26: Radial Magnetic Flux Density from Separated Permanent Magnet 37
Figure 27: Axial Magnetic Flux Density from Separated Permanent Magnet 38
Figure 28: Vector Field of Magnetic Flux Density from Separated Permanent Magnet 39
Figure 29: Total Radial Magnetic Flux Density 40
Figure 30: Total Axial Magnetic Flux Density 41
Figure 31: Vector Field of Total Magnetic Flux Density 41
Figure 32: Force relationship for no current with variable gap 46
Figure 33: Standard Deviation of error terms for various polynomial curve fits 46
Figure 34: Force relationship for fixed current with variable gap [1 Amp] 48
Figure 35: Force relationship for fixed current with variable gap [-1 Amp] 49
Figure 36: Dual Sided Absorber Configuration 50
Figure 37: Dual Sided Absorber Force Relationship 51
Figure 38: Dual Sided Absorber Force Relationship, Linear Range 51
Figure 39: Dual Sided Absorber Force Relationship, Duffing's Approximate 53
Figure 40: Dual Sided Absorber Force Relationship, Duffing's Approximate 53
Figure 41: Dual Sided Absorber Force Relationship, Duffing's Approximate 54

Figure 42: Mechanical Spring System Configuration 58
Figure 43: Construction for Eddy Currents in a Cylinder 59
Figure 44: Beam System Diagram for Damping Determination 61
Figure 45: One Degree of Freedom with base motion 63
Figure 46: X/Y Transfer Function for Base motion 64
Figure 47: X/Y Linear System Transfer Function Simulation 65
Figure 48: Absorber Configuration for Simulation 66
Figure 49: First order TF for non-linear system 67
Figure 50: First order TF for non-linear system 68
Figure 51: First order TF for non-linear system 68
Figure 52: First order TF for non-linear system 69
Figure 53: First order TF for non-linear system 70
Figure 54: First order TF for non-linear system 71
Figure 55: First order TF for non-linear system 71
Figure 56: First order TF for non-linear system 72
Figure 57: Gap Variation for Simulation 73
Figure 58: First order TF for non-linear system 74
Figure 59: First order TF for non-linear system 74
Figure 60: First order TF for non-linear system 75
Figure 61: First order TF for non-linear system 75
Figure 62: First order TF for non-linear system 76
Figure 63: First order TF for non-linear system 76
Figure 64: First order TF for non-linear system 77
Figure 65: First order TF for non-linear system 77
Figure 66: First order TF for non-linear system 78
Figure 67: First order TF for non-linear system 78
Figure 68: Pure Tone Excitation and Response for non-linear system 80
Figure 69: Harmonic TF for non-linear system 80
Figure 70: Harmonic TF for non-linear system 81
Figure 71: Harmonic TF for non-linear system 81
Figure 72: Mechanical Drawings 83
Figure 73: Apparatus Photograph 84
Figure 74: Force vs Displacement Experiment 85
Figure 75: SDOF Force to Displacement Experiment Model 85
Figure 76: Experimental Data and Curve Fit Selections, no current 87
Figure 77: Curve Fit Residual Standard Deviations for Various Polynomials 87
Figure 78: Experimental Force Relationship 89
Figure 79: Dual-Sided Absorber and Curve Fit Selections 90
Figure 80: Mechanical Spring System Configuration 91
Figure 81: Transfer Function for Bearing with Mechanical Springs [1] 92
Figure 82: Transfer Function for Bearing with Mechanical Springs [2] 93
Figure 83: Beam System Diagram 95
Figure 84: Time Response for Beam Systems 95
Figure 85: Transformed Data Curve Fit 96
Figure 86: Combined System 98
Figure 87: Frequency Response Function for SDOF and standard fixed TVA 101

Figure 88: Frequency Response Functions for SDOF and TVA with varied stiffness.....101
Figure 89: Frequency Response Functions for SDOF and TVA with varied stiffness.....103
Figure 90: Frequency Response Functions for SDOF and TVA with varied stiffness.....104
Figure 91: Frequency Response Functions for SDOF and TVA with varied damping.....105
Figure 92: Frequency Response Functions for SDOF and TVA with varied stiffness & damping 106
Figure 93: Frequency Response Functions for SDOF and TVA with varied stiffness & damping 106
Figure 94: Experimental and theoretic stiffness for various gaps. 108
Figure 95: Transfer Function: x_1/u SDOF.....109
Figure 96: Frequency Response Functions for 2-DOF varied gap – 11.0mm gap.....110
Figure 97: Frequency Response Functions for 2-DOF varied gap – 15.0 mm gap.....110
Figure 98: Frequency Response Functions for 2-DOF varied gap – 20.0 mm gap.....111
Figure 99: Frequency Response Functions for 2-DOF varied gap – 22.0 mm gap.....111
Figure 100: Frequency Response Functions for 2-DOF varied gap – 24.0 mm gap.....112
Figure 101: Frequency Response Functions for 2-DOF varied gap – 26.0 mm gap.....112
Figure 102: Frequency Response Functions for 2-DOF varied gap – 28.0 mm gap.....113
Figure 103: Frequency Response Functions for 2-DOF varied gap – 30.0 mm gap.....113
Figure 104: Single DOF Absorber System 116
Figure 105: X/Y TF for Smallest Gap 117
Figure 106: X/Y TF Coherence [x_0 = 10.3 mm].....117
Figure 107: X/Y TF for Medium Gap 118
Figure 108: X/Y TF Coherence for Medium Gap 118
Figure 109: X/Y TF for Wide Gap.....119
Figure 110: X/Y TF Coherence for Wide Gap 119
Figure 111: X/Y TF for Smallest Gap Simulation [c=1.0Ns/m].....121
Figure 112: X/Y TF for Smallest Gap Simulation [c=3.0Ns/m].....121
Figure 113: X/Y TF for Smallest Gap Simulation [c=5.0Ns/m].....122
Figure 114: X/Y TF for Medium Gap Simulation.....122
Figure 115: X/Y TF for Wide Gap Simulation 123
Figure 116: X/Y TF for No Current 125
Figure 117: X/Y TF Coherence for No Current.....126
Figure 118: X/Y TF for +5 Amps Current.....126
Figure 119: X/Y TF Coherence for +5 Amps Current 127
Figure 120: 2-DOF System.....128
Figure 121: Experiment TF for SDOF and 2-DOF system 128
Figure 122: Experiment Coherence for SDOF and 2-DOF system.....129
Figure 123: Experiment TF for SDOF and 2-DOF system 129
Figure 124: Experiment Coherence for SDOF and 2-DOF system.....130
Figure 125: Experiment TF for SDOF and 2-DOF system 130
Figure 126: Experiment Coherence for SDOF and 2-DOF system.....131
Figure 127: Experiment TF for SDOF and 2-DOF system 131
Figure 128: Experiment Coherence for SDOF and 2-DOF system.....132
Figure 129: Experiment TF for SDOF and 2-DOF system 132
Figure 130: Experiment Coherence for SDOF and 2-DOF system.....133
Figure 131: Experiment TF for SDOF and 2-DOF system 133
Figure 132: Experiment Coherence for SDOF and 2-DOF system.....134

Figure 133: Experiment TF for SDOF and 2-DOF system 134
Figure 134: Experiment Coherence for SDOF and 2-DOF system..... 135

Acknowledgments

The author wishes to thank those that helped him along the way to arrive at this research. I want to thank Dr. Wicks for his technical knowledge, encouragement, and guidance along the way.

I thank all my committee members for their efforts to guide, review, and critique this research. I thank all the graduate students that have helped solve problems and given insight along the way, including Rich Lomenzo, Eric Swanson, and David Coe. I thank Mike Pastor for providing encouragement and strategy board game diversions along the way. I also thank all the underwater hockey players over the years that have helped provide diversions.

I thank Kami Razvan for his encouragement, sense of humor and for providing consulting work to fund my time as a graduate student.

I especially appreciate my wife's encouragement and patience as I completed the research

CHAPTER 1. INTRODUCTION

Tuned Vibration Absorbers (TVA) have been used since 1911 to attenuate structural vibration.[1] These devices aid in vibration reduction by adding a mass, a spring, and possibly a damper. Figure 1 shows the standard TVA configuration. The combined systems' displacement (x_1) has an anti-resonance point at which frequency the primary structure will have a minimized response. These devices attempt to cancel a single frequency or attenuate narrow-band vibration. There is an extensive body of knowledge on Tuned Vibration Absorbers or Tuned Dampers (TD); some of the relevant papers will be examined and contrasted to the current work in Chapter 2.

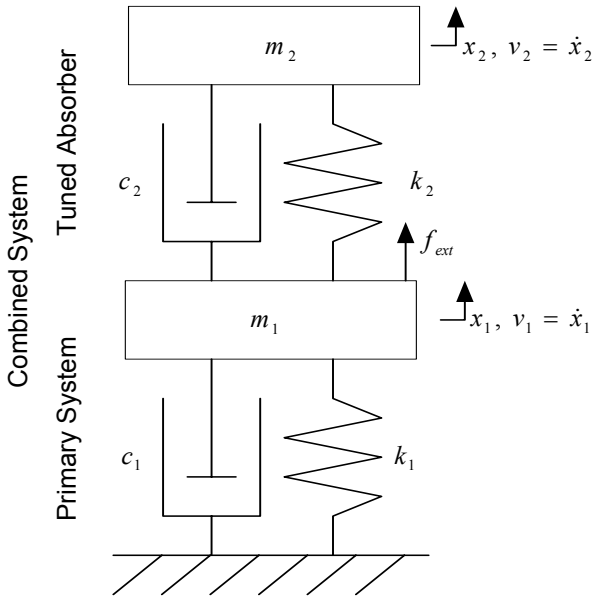

Figure 1: Passive TVA Configuration

Frequently, TVAs are used to suppress running speed imbalance responses from rotating machinery. These devices can be very effective passive solutions under two conditions:

a) the system dynamics are invariant, and

b) the running speed is within a narrow frequency range.

When the system undergoes operational speed variations, condition (b) is not fulfilled, and the combined system's performance suffers. For the traditional tuned absorber, as the excitation frequency shifts from the anti-resonance point, the response increases and eventually reaches responses larger than that of the primary system alone.

Two methods exist to solve these limitations, a semi-active system and an active system. A semi-active system is defined by a system that an alteration can be made and no additional energy is necessary to have this change persist. An active system requires continuous energy expenditures to keep the system with the same characteristics. Both active and semi-active TVAs have been used to attenuate rotating machinery vibrations.[2] If the tuned absorber has a variable stiffness element (semi-active), then the minimum amplitude response can also shift. This system is depicted in Figure 2. If these shifts are coordinated, the minimum response can remain at the varying excitation frequency. This research addresses the quasi steady-state vibration reduction by electromagnetic stiffness variations. The stiffness variation is proposed with electromagnetic pole forces, varied with current input and gap space setting.

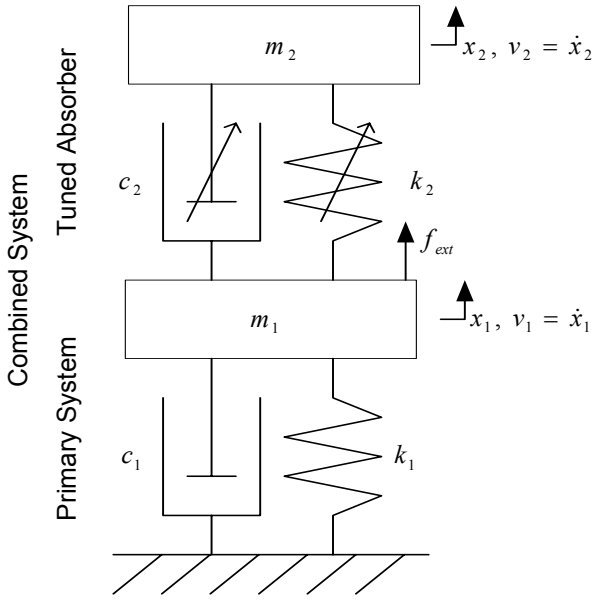

Figure 2: Semi-active TVA Configuration

The active TVA extensions that have been implemented are known as a Proof Mass Actuators (PMA) or Electromechanical Actuators (EMA). A force generator placed in parallel with the spring, as seen in Figure 3, allows further control. This configuration allows a controllable reaction force between the primary system and the absorber mass. These devices may be used for active structural control. The force generator is typically controlled to minimize a sensor response. This design can add energy to the primary system with its active force element. With many active systems a stability problem based on the selected control law can result.

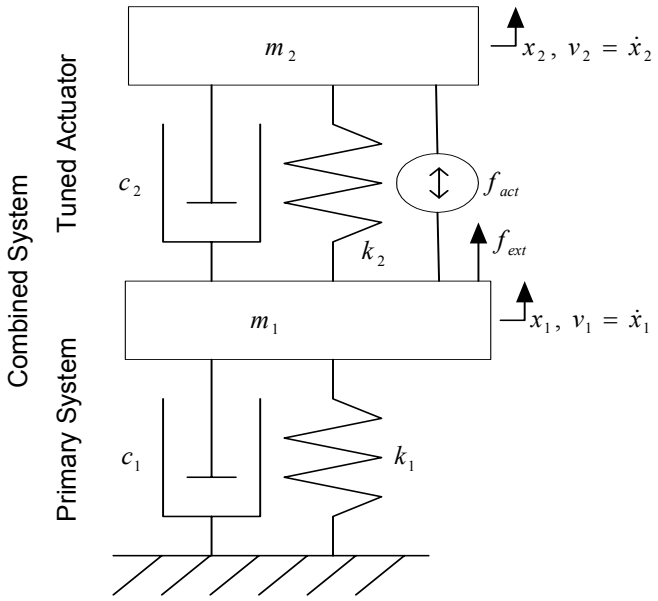

Figure 3: Active TVA Configuration

Problem Examined: Magnetic Tuned Vibration Absorber

Electromagnetic forces have been implemented in various configurations to affect a TVAs response. The proposed configuration, Figure 4, uses forces between magnetic poles within a magnetic circuit. This configuration has an electromagnet suspended between two permanent magnets using electromagnetic springs. This arrangement offers a chance to alter the effective spring constant by the coil current (active) and the proximity from the stationary permanent magnets (semi-active). A number of alternative designs have been discussed in literature.

A prior active configuration, the proof mass actuator (PMA) has been implemented with a wire-wound coil in a radial magnetic field, also known as a voice coil configuration.[3,4] A voice coil harnesses forces on a current carrying conductors while perpendicular to a magnetic field. This enables an active force element to be integrated in the TVA.

Nagaya has implemented related actuator designs similar to the actuator implemented for this research. Nagaya and Arai studied a design for permanent magnet levitation with electromagnetic forces.[5] Their application involves eliminating tabletop vibrations. Nagaya and Sugiura continued the work and presented a feedback linear spring model for a levitated permanent magnet.[6]

This dissertation builds on their research by inverting the electromagnets and the permanent magnets and providing for gap variations between the stationary magnets. The investigated configuration has only one electromagnet, the moving mass. This work examines system forces and dynamic responses with varied DC currents and varied gaps in a vibration absorber configuration.

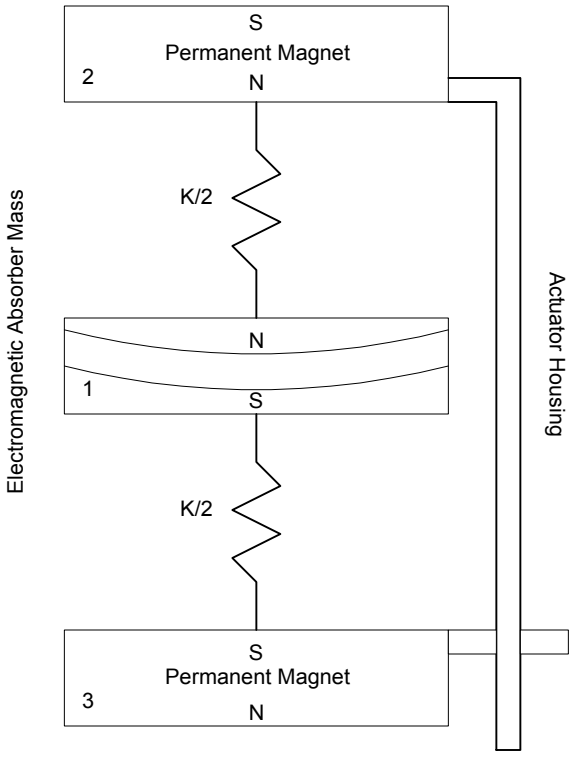

Figure 4: Investigated configuration

Another design was patented by Waterman for a concept using a soft ferromagnetic secondary mass and two electromagnetic horseshoe magnets.[7] These electromagnets can provide an attraction force and reduce the stiffness. This dissertation differs from Waterman's work since it relies on forces between magnetic poles, rather than the attractive force between a magnet and a ferromagnetic material. One benefit is that the force can be increased and decreased with the investigated configuration. Also the implemented configuration can be used semi-actively with the variable gap setting.

Leibovich's design was patented for force generation from a permanent magnet actuator.[8] His embodiment, similar in character to Nagaya and Sugiura's research[6], has a permanent magnet as the mobile mass. This research differs in its implementation of an electromagnet as the tuned mass.

This dissertation proposes, models, simulates, and constructs a variable stiffness electromagnetic tuned vibration absorber. The dissertation embodiment is unique in the configuration that the electromagnetic forces are implemented to provide variable stiffness. Electromagnetic forces provide the mechanism for variable stiffness though both current variations and gap variation to provide lower response at various frequencies. This research does not address the control law implementation for the absorber, but rather characterizes the absorber under various conditions.

The research contributions are a nonlinear magnetic field quasi-static model applied to a variable stiffness TVA embodiment, and experimental testing to demonstrate system response. This nonlinear dynamic model will be developed and examined for various configurations. Once modeled, a proof of concept actuator was constructed to verify the response.

Dissertation Outline

This chapter has given the overall picture of the work examined and an overview of simple TVAs. The following chapter addresses TVA fundamentals, the current state of technology, and reviews the literature on various vibration absorbers. Chapter 3 constructs the electromagnetic field derivation. Chapter 4 calculates the force equations given the electromagnetic field derived. Chapter 5 discusses the system damping mechanisms. Chapter 6 outlines the non-linear system simulations of the theoretical response given the derived theory.

Chapter 7 describes the physical system tested and runs initial tests to examine the spring force and damping force present. Chapter 8 examines design issues for a tuned vibration absorber. Chapter 9 presents the experimental findings and confirms the shifting range for lowering the vibration. Chapter 10 overviews this work's contributions and discusses future work. Each chapter's summary provides the review of how the chapter's contribution helps characterize the absorber.

CHAPTER 2. TVA FUNDAMENTALS & LITERATURE REVIEW

TVA Fundamentals

The following sections provide a review of tuned mass absorbers (TVAs), tuned dampers (TD), and proof mass actuators (PMAs). First, a one degree-of-freedom (1-DOF) system is chosen as the primary system, and its freqnecy response function is examined. Then the impact of adding a TVA to the primary system is examined.

Primary System (Single DOF)

The primary system of interest will be simplified to a one degree of freedom, mass-spring-damper system. This is shown in Figure 5.

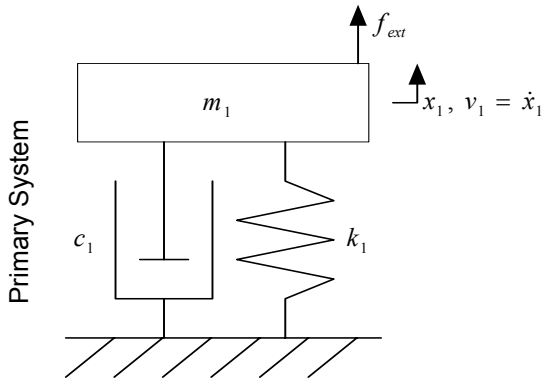

Figure 5: Primary System, One Degree of Freedom

The system's equation of motion is

$$m_1\ddot{x}_1 + c_1\dot{x}_1 + k_1x_1 = f_{ext}(t) \tag{1}$$

By manipulating the equation in the frequency domain, the frequency response is found as

$$\frac{X_1}{F_{EXT}} = \frac{1/k_1}{1-\left(\frac{\omega}{\omega_{n,1}}\right)^2 + 2\zeta_1\left(\frac{\omega}{\omega_{n,1}}\right)j} \tag{2}$$

(2 is presented in normalized frequency form with respect to the undamped natural frequency. The frequency response graph is shown in Figure 6. It is seen that there is one resonance, and operation close in frequency may have unacceptably high response based on the damping level present.

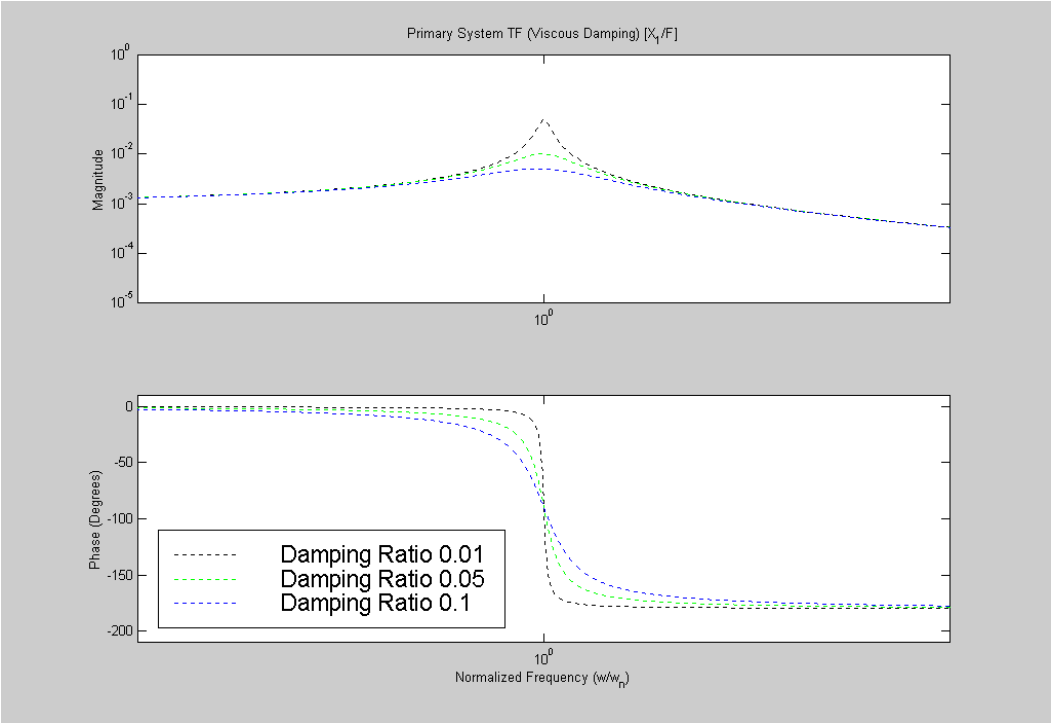

Figure 6: Primary System Frequency Response Function

If this SDOF system were excited with a rotating imbalance at startup, a large, potentially damaging response would occur while the rotating system passed through this resonance. This is one case where it would be advantageous to have a tunable vibration absorber. Next the effects of a passive TVA will be examined.

Primary System with TVA (Combined System)

By adding a connected mass-spring-damper system the combined system's response will be different from the primary systems. If the tuned absorber is chosen for the excitation frequency, the primary mass will have lower response for this pure tone. Figure 7 depicts the combined system.

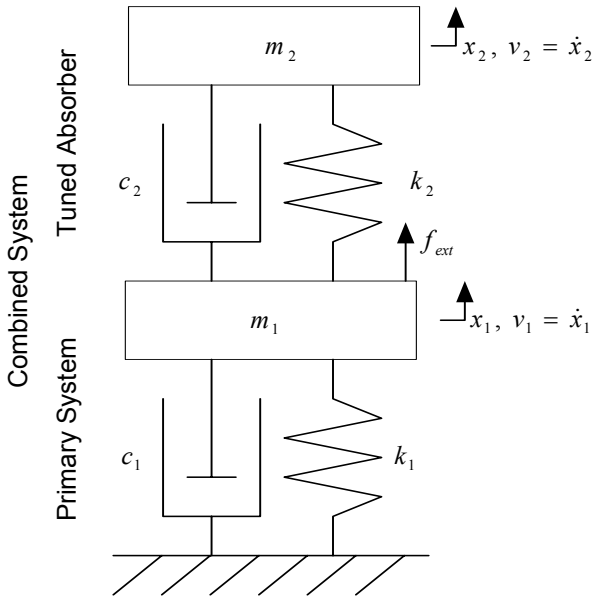

Figure 7: Combined System

The matrix equation of motion becomes:

$$\begin{bmatrix} m_1 & 0 \\ 0 & m_2 \end{bmatrix}\begin{Bmatrix} \ddot{x}_1 \\ \ddot{x}_2 \end{Bmatrix}+\begin{bmatrix} c_1+c_2 & -c_2 \\ -c_2 & c_2 \end{bmatrix}\begin{Bmatrix} \dot{x}_1 \\ \dot{x}_2 \end{Bmatrix}+\begin{bmatrix} k_1+k_2 & -k_2 \\ -k_2 & k_2 \end{bmatrix}\begin{Bmatrix} x_1 \\ x_2 \end{Bmatrix}=\begin{Bmatrix} f_{ext} \\ 0 \end{Bmatrix} \tag{3}$$

This system can be reduced by Laplace Transforms, using matrix notation:

$$X = \left(Ms^2 + Cs + K\right)^{-1} F_{EXT} \tag{4}$$

At the tuned frequency it is desired that the combined system will have an anti-resonance point. At this frequency the TVA's inertia opposes the excitation force. This leads to minimum displacement and therefore the minimum energy enters the primary system. This is due to the high impedance at this anti-resonance. If the primary system resonance is not desirable one may add a TVA to provide shifted resonant frequencies that are outside the disturbance frequency. Equation (5) is the frequency response for the primary mass of the combined system.

$$\frac{X_1}{F_{EXT}} = \frac{\frac{1}{k_1} * \left(\left(\frac{\omega_{n,2}}{\omega_{n,1}} \right)^2 - \left(\frac{\omega}{\omega_{n,1}} \right)^2 - 2j\zeta_2 \left(\frac{\omega_{n,2}}{\omega_{n,1}} \right) \left(\frac{\omega}{\omega_{n,1}} \right) \right)}{\left\{ \left(\frac{\omega}{\omega_{n,1}} \right)^4 - \left(\left(\frac{\omega_{n,2}}{\omega_{n,1}} \right)^2 + 4\zeta_1\zeta_2 \left(\frac{\omega_{n,2}}{\omega_{n,1}} \right) + \frac{k_2}{k_1} + 1 \right) \left(\frac{\omega}{\omega_{n,1}} \right)^2 + \left(\frac{\omega_{n,2}}{\omega_{n,1}} \right)^2 + \right.} \\ \left. \left\{ j \left(- \left(2\zeta_1 + 2\zeta_2 + \frac{c_2}{\sqrt{k_1 m_1}} \right) \left(\frac{\omega}{\omega_{n,1}} \right)^3 + \left(2\zeta_1 \left(\frac{\omega_{n,2}}{\omega_{n,1}} \right)^2 + 2\zeta_2 \left(\frac{\omega_{n,2}}{\omega_{n,1}} \right) \right) \left(\frac{\omega}{\omega_{n,1}} \right) \right) \right\} \tag{5}$$

Equation (6) is the simplified FRF for the case when the primary system resonance is to be cancelled. This occurs if the TVA's natural frequency is set to the primary system's natural frequency ($\left(\frac{\omega_{n,2}}{\omega_{n,1}} \right) = 1$) This is applicable when the original resonance is no longer desired. Figure 8 shows the combined FRF in comparison to the primary system. It uses the lightest damping formerly presented for the primary system and has a 5% damping for the TVA sub-system. Although the original resonance is cancelled, two nearby resonances are created.

$$\frac{X_1}{F_{EXT}} = \frac{\frac{1}{k_1} * \left(1 - \left(\frac{\omega}{\omega_{n,1}} \right)^2 - 2j\zeta_2 \left(\frac{\omega}{\omega_{n,1}} \right) \right)}{\left\{ \left(\frac{\omega}{\omega_{n,1}} \right)^4 - \left(4\zeta_1\zeta_2 + \frac{k_2}{k_1} + 2 \right) \left(\frac{\omega}{\omega_{n,1}} \right)^2 + 1 + \right.} \\ \left. \left\{ j \left(- \left(2\zeta_1 + 2\zeta_2 + \frac{c_2}{\sqrt{k_1 m_1}} \right) \left(\frac{\omega}{\omega_{n,1}} \right)^3 + \left(2\zeta_1 + 2\zeta_2 \right) \left(\frac{\omega}{\omega_{n,1}} \right) \right) \right\} \tag{6}$$

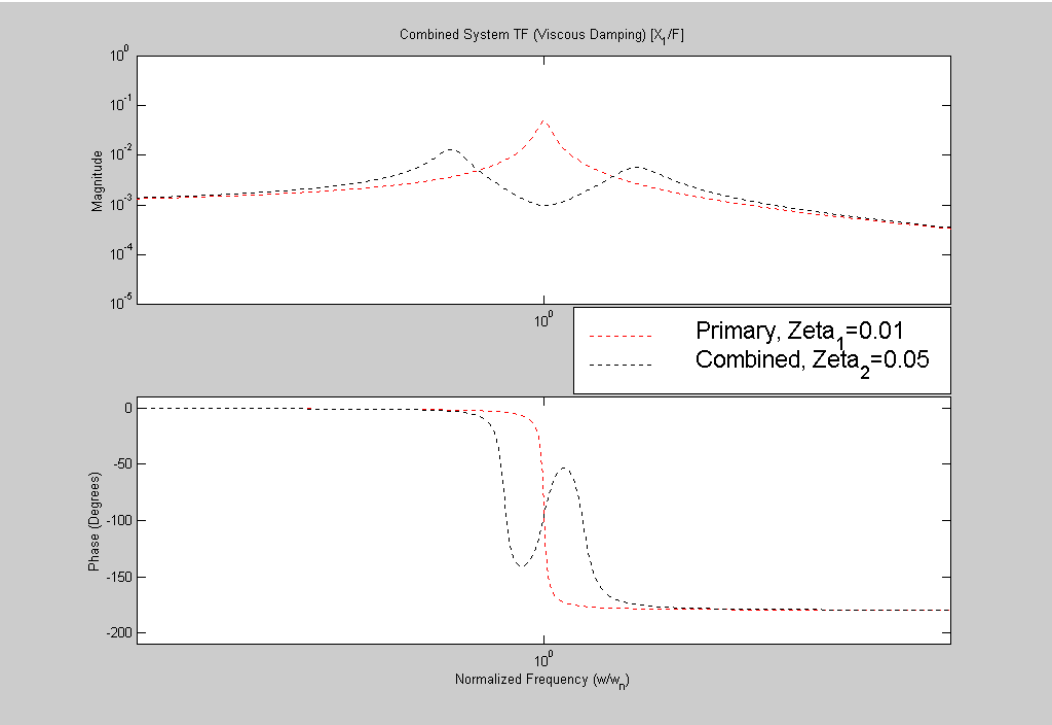

Figure 8: Primary & Combined System Frequency Response Function

Figure 9 presents the combined system with lower damping (1%) for the TVA. Less response is evident near the anti-resonance with the 1% damping, than with 5% damping. Yet examining the phase response one notices that it is more sensitive to small frequency changes. It is noted that increased TVA damping causes an increased response near anti-resonances.

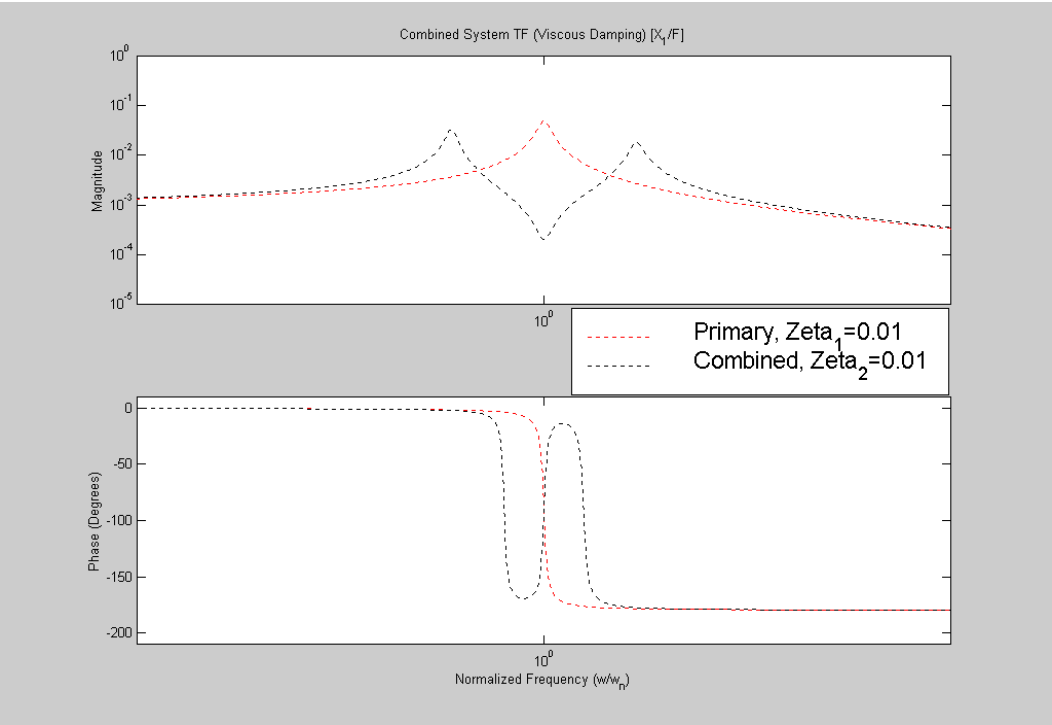

Figure 9: Primary & Combined System Frequency Response Function

One system advantage is the reduction near the tuned frequency. Another advantage is it is an elegant, robust, simple mechanical system. One disadvantage is that the reduction band is limited. The system has gone from one resonance to two nearby resonances in the combined system. If the excitation frequency may change under operation this can lead to unacceptably large displacements. A variable stiffness TVA could address these issues.

The absorber's displacement range is related to the system stiffness ratio and mass ratio between the primary system and the vibration absorber. In the case with cancellation at the original resonance, the stiffness ratio ($\frac{k_2}{k_1}$) appears in Equation (6). In Equation (6) we set $\left(\frac{\omega_{n,2}}{\omega_{n,1}}\right)=1$, so that through manipulation the stiffness ratio and mass ratio are equivalent in this case. The smaller this ratio the larger the displacement for the tuned absorber mass. This can enter as a design limitation in implementation of TVAs. One adjustment is to add damping to the TVA; yet as discussed, this causes increased response at the tuned frequency for the combined system.

Passive Tuned Vibration Absorbers

The passive TVA device was first patented in 1911 by Frahn.[1] The TVA's advantages include the ease of installation, simple design, and effectiveness over narrow frequency band vibration. The TVA is selected such that the combined system has an anti-resonance at the desired cancellation frequency. An undamped TVA allows the best suppression at a specified fixed design frequency. This is effective if the excitation frequency remains constant. The disadvantage is that if the excitation frequency shifts, the response of the combined system may be larger than the primary system alone.

The narrow operation band can adversely affect a system that changes over time, or that operates at varied frequencies. The tuned absorber reduces vibration around the tuned frequency, yet it will make vibration worse at the combined system's two new natural frequencies. In 1928, Ormondroyd and den Hartog, discussed adding damping to the passive vibration absorber.[9] This helps reduce the response across a wider frequency range, yet does not completely cancel the vibration anywhere. The rest of this section reviews some of the more recent literature on TVAs.

Thomson provides introductory vibration theory and discusses the basics of passive vibration absorbers and demonstrates the change in frequency for various mass ratios.[10] Korenev and Reznikov published a comprehensive book on many aspects of dynamic vibration absorbers.[11] They present extensive analysis of harmonic excitation with both stable and unstable frequencies. The frequency response invariant points are explained; these frequencies have the same magnitude response irrespective of the viscous damping coefficient. They discuss transient vibrations, vibration under random excitations, and multi-mass vibration absorbers. They devote a complete section to continuous systems with dynamic absorbers attached. Einstein and Wernerowski also examined a multi-mass absorber system.[12] With the additional elements, this enables the attenuation of added frequencies.

Sun, Jolly, and Norris in their survey paper discuss passive absorbers in the first section.[13] They examine an impedance coupling model for selecting TVA parameters. This approach is convenient in that it requires only the driving point impedance and not the entire structural model. They also discuss

passive absorber design variations: pendulum-type, rotary TVAs, and an ER-fluid rotating dynamic absorber. This paper provides an excellent overview of the current body of knowledge and an extensive reference section.

Soom and Lee furthered our knowledge of passive absorbers by examining the optimal parameters settings for various conditions.[14] They examined minimizing the single-frequency response, minimizing the frequency response across a range, minimizing the velocity, and minimizing the mean square displacement or velocity. They also examined how nonlinear stiffness elements affected these cost functions.

Özgüven and Çandir sought the optimum parameters of two vibration absorbers tuned to the first two beam resonances.[15] They demonstrated that the optimum parameters for the first resonance TVA are dependent on the second resonance TVA, while not the reverse. This demonstrates the dynamic coupling in a multiple degree of freedom system.

Kobayashi and Aida discuss a Houde damper implemented with magnetic damping.[16] A Houde damper is an auxiliary mass and a damping element added to a primary structure; no spring element is present. Their research examines how magnets can be used in conjunction with a moving conductor to dissipate mechanical energy. They were successful in attenuating pipe vibrations. Yamashita and Seto also implement magnetic damping.[17] They list four advantages:

i) Good linearity of damping characteristics, no mechanical contact and no friction,
ii) Stability of damping for changing time and temperature,
iii) Clean, no oil to leak and no dust, and
iv) It can be used in space.

They construct and test a dual dynamic absorber using magnetic damping. Extending the research Yamashita, Sawatari and Seto design a system of five dual dynamic absorbers to control the resonance peak of a piping system.[18] They model the piping system by the transfer matrix method and find seven resonance peaks that they successfully eliminate. These three papers demonstrate the use of magnetic damping in passive TVA construction.

The literature review of passive approaches shows the extensive use of TVA and a number of limitations. The passive TVA boundaries are extended by various methods using semi-active and active actuator configurations. These configurations are discussed next.

Semi-Active Tuned Vibration Absorbers

Semi-active TVAs are systems implemented such that small energy expenditures can alter the system parameters. Systems can have variable inertia, variable damping, variable stiffness, or variable initial conditions. The primary attraction to semi-active systems is the small energy expenditure needed to reduce vibration.

Semi-Active Variable Inertia TVAs

Takita and Seto investigated using a variable length pendulum to adaptively tune the absorber.[19] By adjusting the moment arm of the pendulum mass the tuned frequency shifts. This was a creative implementation to provide a tuning mechanism for the anti-resonance. Moyka also examined a semi-active system with variable inertia.[20] Altering the pendulum length using a stepper motor varied the effective inertia. They demonstrated the frequency response functions for various pendulum lengths on a cantilevered beam primary system.

Semi-Active Variable Stiffness TVAs

A system that could alter its stiffness provides a unique opportunity. Given knowledge of the excitation frequency alone, it could provide minimum response at any frequency within its tuning range. The system is depicted in Figure 10. Since attenuation is more effective with less damping at the tuned frequency, the absorber damping should be minimized.

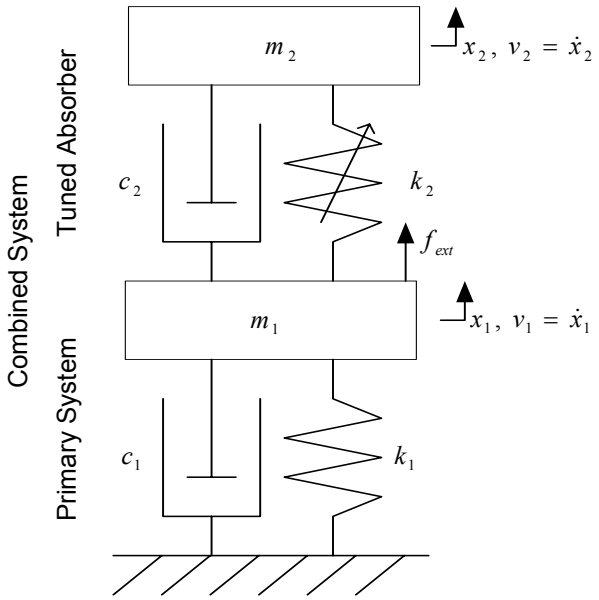

Figure 10: Variable Stiffness Viscously Damped Combined System

Variable stiffness TVAs have been discussed in a number of papers. Wang and Lai have developed control theory during rotational system startup using variable stiffness.[2] Their research focus is on developing a control law that minimizes the system energy for a simulated beam structure with a rotating machinery attached. They do not address the practicality of implementing such a variable stiffness actuator. Walsh and Lamancusa investigated control of rotating imbalance during constant acceleration and constant rotational velocity to minimize RMS response.[21] They use an adjustable stiffness compound leaf spring provide a variable stiffness element. The spring stiffness is determined using finite element techniques. This dissertation research examines the forces provided from an electromagnetic actuator, while leaving the control law aside.

Hubbard and Margolis discussed a semi-active spring concept.[22] They discussed varying the time rate of change of the compliance force. They discuss the variable spring constant's equivalence to a force generator in which the rate of change is controlled. They propose two implementations: a discretely variable spring and damper configuration, and a pneumatic spring. They conclude that the performance improvements may be justified.

A number of methods to provided stiffness variation have been investigated. Ryan, Franchek, and Bernhard present a variable stiffness TVA that changes the helical spring length for stiffness alteration.[23] The preceding paper provides direct variation in the stiffness element via mechanical means. Slavicek and Bollinger have produced a variable stiffness by using nonlinear stiffness characteristics of plastic elements.[24] The current research examines electromagnetic stiffness alteration. Buhr, Franchek and Bernhard present a control law for tuning a variable stiffness vibration absorber to attenuate a pure tone.[25]

Thus variable stiffness, when properly tuned, will benefit the primary mass vibration reduction. This dissertation research characterizes and tests a nonlinear variable stiffness TVA using electromagnetic forces.

Semi-Active Variable Damping

Many researchers have addressed semi-active variable damping. Karnopp, Crosby, and Harwood implement a semi-active electro-hydraulic damper.[26] They find by computer simulation that semi-active systems can approach the results from a fully active system. The primary advantage of a semi-active system is that it only requires signal processing and low level power signals; rather than full power electronics for an active system. Hrovat, Barak, and Rabin demonstrate semi-active hydraulically controlled damping modulation to damp wind induced vibration in tall buildings.[27]

In 1992, Tanaka and Kirushima published their work on impact vibration control using a semi-active damper.[28] They focus on controlling the transient vibrations at impact rather than steady state. They propose a semi-active damper, driven by releasing a damper mass from an initial displacement to suppress transient vibrations. They referred to this as variable initial conditions.

These three papers address the issue of isolation and suspension with semi-active methods, rather than using an auxiliary TVA. Rakheja and Sankar discussed vibration isolation from a semi-active 'on-off' damper.[29] The damping is controlled by a variable sized orifice. The results of the two-state damper are compared to a passive damper. Another group that studied semi-active suspension implemented a quadratic performance index using knowledge from stochastic optimal control theory.[30] In 1988, Miller reported passive, semi-active, and active suspension system tests on a quarter car model.[31] Ride

comfort, road holding, and suspension travel were investigated with random input velocity to simulate road roughness.

Kobayashi and Aida developed a damper using variable magnetic damping.[16] Variable damping helps TVAs dissipate energy most effectively. Yet as presented in the prior section, damping reduces the attenuation near the anti-resonance.

This research will not attempt to control the damping. It will examine the different damping mechanisms present in the mechanical TVA constructed. Chapter 7 examines the mechanical damping and the electromagnetic damping in the TVA designed.

Active Tuned Vibration Absorbers

To provide additional features, active TVAs, or Proof Mass Actuators (PMA), were introduced that have an arbitrary force generation mechanism in parallel with the spring and damper. This adds flexibility to incorporate control theory to provide cancellation forces. This force has frequently been implemented with a voice coil actuator design. The majority of literature in this area focuses on control law issues. Although this research does not address the TVA control law; a sampling of the papers in this area are discussed

Stephens, Rouch, and Tewani develop a theory using a damped dynamic vibration absorber with an active control element.[32] Their work focuses on transfer function with various feedback laws. The control law implemented consisted of a linear combination of the primary structure velocity and acceleration. Seto, Sawatari, and Takita present work on the linear quadratic (LQ) optimal control theory applied to active TVAs.[33] Seto and Sawatari proposed a design method for active dynamic absorbers using the LQ optimum control theory.[34] It is experimentally shown that the random response of the vibration-controlled system is attenuated by five times that of an uncontrolled. In this paper they use an electromagnetic voice coil actuator design, to provide additional internal forces.

Burdisso and Heilmann contrasted a single-mass active dynamic absorber and a dual-mass active dynamic absorber for broadband control.[35,36] Both systems were controlled with a feedforward

filtered-X LMS algorithm. The dual-mass configuration presented requires less control force than the single-mass active TVA.

A survey paper by von Flotow, Beard, and Bailey covers a number of adaptively tuned TVA designs.[37] It discusses TVAs implemented in the aircraft industry, installed on the DC-9 and MD-80. Waterman presents a variable stiffness electromagnetic actuator based on the attraction of ferromagnetics.[7] The focus of this dissertation is different in that the attraction and repulsion are from magnetic poles, rather than using the ferromagnetic attraction. Bonesho and Bollinger developed the theory for variable damping and variable stiffness, while applying it to machine tools.[38,39]

Sato examines a unique configuration using a variable speed rotor that may be partially filled with a liquid.[40] The variable speed controls the cancellation frequency. This embodiment is shown effective if the rotor speed is adjusted with the excitation frequency. The dissertation embodiment has similar goals to the Sato's actuator, with a different approach based on different principles.

Okada, Matsuda, and Hashitani present a novel circuit to provide sensing and actuation in a voice coil design.[41] The velocity is estimated based on the driving voltage and current. This self-sensing active TVA is successfully experimentally demonstrated.

Sun, Jolly, and Norris prepared a comprehensive survey paper of these devices.[13] Chang and Soong present an approach for optimal design of an active TVA system.[42] Their application is inclusion of an active force element in large-scale civil engineering structures. Nishimura, et al. investigated work on an active TVA for a TVA.[43]

Olgac and Holm-Hansen develop the delayed resonator concept to provide active control of a TVA.[44,45] The delayed resonator provides an interesting approach; it uses properly selected time delayed position feedback. They examine a number of tuning methods to quickly attenuate a range of vibration frequencies. They examine the system stability and response with simulations.

Sommerfeldt and Tichy develop an adaptive control system applied to minimize the force transmitted through a two-stage vibration isolation mount.[46,47] They investigate a two-stage vibration mounts to

reduce force transmission. They implement an adaptive least-mean-squares (LMS) algorithm for provided control. Zimmerman, Horner, and Inman describe a proof-mass actuator designed for structural control.[4] This actuator, along with its onboard sensors and microprocessor was tested for space structures. Experiments demonstrated that rate-feedback could be used to damp transverse vibrations of a cantilever beam. The preceding two publications used a moving coil actuator, while this dissertation will implement an electromagnetic pole actuator.

Hyde and Anderson developed an active actuator using the same fluid for damping and as an hydraulic lever for a voice coil.[48]

Okada and Okashita examined a moving coil active damper.[49] Their work focus on using state feedback to increased damping. This dissertation examines the damping present and the cause, yet does not look to actively increase damping.

Summary

The papers referenced in this review cover many aspects of tuned vibration absorbers. They have been examined as three categories based on control mechanisms: passive, semi-active, and active. This dissertation research focuses on characterizing an absorber that could be used in both semi-active and active control. Altering the gap spacing is a semi-active means to alter the system stiffness, while providing a DC current is an active method. This research demonstrates how the variable gap and variable current alter the system's transfer function.

This absorber type could be implemented to lessen the vibration for a rotating machinery platform. Small speed variations in the machinery will cause the excitation frequency to vary and this absorber can adjust based on the running speed. The TVA control laws are not addressed in this research.

CHAPTER 3. ELECTROMAGNETIC FIELD FORMULATION

This chapter develops the electromagnetic field equations. The system configuration is first presented to provide the basis of the derivations. A set of simulation parameters is specified so the resulting component fields may be graphed. Then the magnetic flux density field is determined from fundamental equations for the proposed configuration. These fields are developed, presented, and discussed. The following chapter derives the force equations given the magnetic flux density. Nagaya and Arai's derivation has been adapted to handle the proposed configuration.[5]

System Configuration

Figure 11 depicts the proposed system configuration with a moving electromagnet absorber placed between two stationary permanent magnets. The permanent magnets provide a passive restoring force to center the absorber. The force level may be varied by supplying the electromagnet current or by altering the stationary magnets position. The electromagnetic fields are calculated as the intermediary step to determine the force level between the absorber and the stationary magnet.

The simplified system is pictured in Figure 12. The spring force is influenced by the design parameters, current input, and the gap variation. The electromagnetic fields produce the spring force and also influences the absorber damping force. This research begins by theoretically quantifying the electromagnetic fields, converting these to the spring force (Chapter 4), with the goal of providing spring force variations to reduce a primary system's vibration (Chapters 6-8). This research also examines the damping forces under different conditions, while not attempting to directly control this parameter (Chapters 5 & 7).

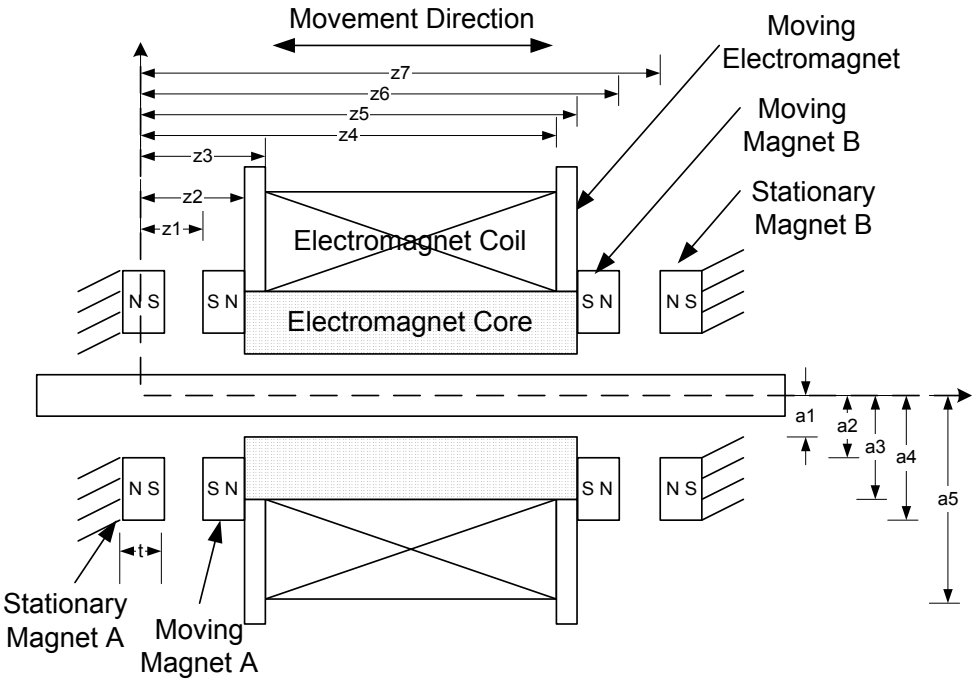

Figure 11: Proposed System Configuration

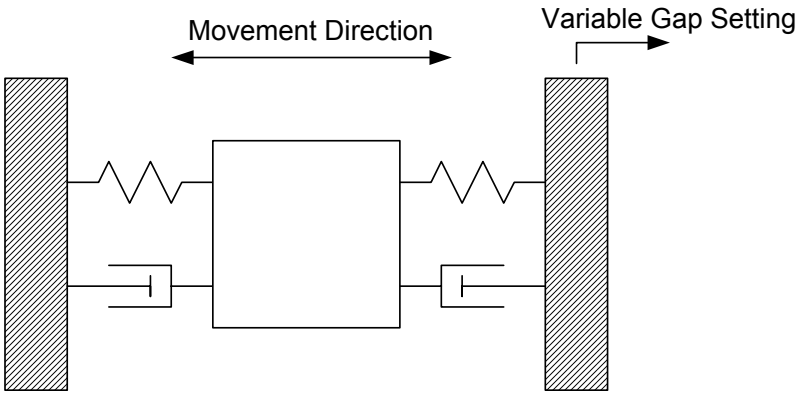

Figure 12: Simplified System Diagram

Table 1 lists the values used for the simulations throughout the development. The simulations provide a means to examine the magnetic flux density produced by the different component parts. The magnetic flux development will focus on only the left side of Figure 11; knowing that the right side will react similarly.

Table 1: Simulation Numerical Parameters

Description	Symbol	Value
Magnetization strength	J_0	0.405 T
Coil turns	N	50
Current	I	1.0 A
Permeability of free space	μ_0	$4\pi \times 10^{-7}$ (Wb/ATm)
Permanent magnet thickness	t	10.0 mm (0.394 in)
Inner Core Radius	a_1	6.4 mm (0.25 in)
Inner Permanent Magnet Radius	a_2	7.938 mm (0.3125 in)
Outer Core Radius/ Inner Coil Radius	a_3	12.7 mm (0.50 in)
Outer Permanent Magnet Radius	a_4	25.0 mm (0.984 in)
Outer Coil Radius	a_5	25.0 mm (0.984 in)
Right magnet edge	z_1	80 mm
Core lead edge	z_2	90 mm
Coil lead edge	z_3	90 mm
Coil far edge	z_4	109 mm
Leakage	υ	0.809

Magnetic Flux Density Derivation

The magnetic flux density in the proposed configuration is found by evaluating the constituent contributions then applying the superposition principle. The component magnetic flux fields are due to the current carrying coil, the core within the current carrying coil, the permanent magnet and core, and the stationary magnets. The field of interest is that between the two permanent magnets on the left of Figure 11. The first derivation is the magnetic flux density from a simple loop, this is the foundation of the magnetic flux density from the coil.

Magnetic Flux Density from Elemental Loop

The loop is depicted in Figure 13. The loop radius is a, I is the loop current, and r & z are the cylindrical coordinates, Θ is unnecessary since the field is symmetric. A complete derivation is found in Craik.[50]

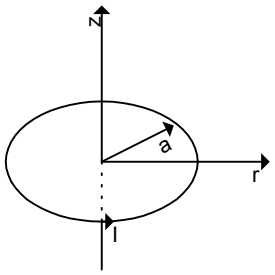

Figure 13: Elemental Loop Configuration

The magnetic flux density can be expressed as the radial and axial elements.

$$B_{r,loop}(r,z,I) = \mu_0 I f_r(a,r,z) \tag{7}$$

$$B_{z,loop}(r,z,I) = \mu_0 I f_z(a,r,z) \tag{8}$$

The functions f_r and f_z are solely based on the elemental loop geometry. These functions incorporate the complete elliptical integrals of the first and second kind.

$$f_r(a,r,z) = \frac{1}{2\pi}\frac{z}{r\sqrt{(a+r)^2+z^2}} \times \left[\frac{a^2+r^2+z^2}{(a-r)^2+z^2}E(k') - K(k')\right] \tag{9}$$

$$f_z(a,r,z) = \frac{1}{2\pi}\frac{1}{\sqrt{(a+r)^2+z^2}} \times \left[\frac{a^2-r^2-z^2}{(a-r)^2+z^2}E(k') + K(k')\right] \tag{10}$$

The elliptical integrals are defined as

$$K(k') = \int_0^{\pi/2} \frac{d\Theta}{\sqrt{1-k'^2\sin^2\Theta}}, \text{ Complete Elliptical Integral of the First Kind} \tag{11}$$

$$E(k') = \int_0^{\pi/2} \sqrt{1-k'^2\sin^2\Theta}\, d\Theta, \text{ Complete Elliptical Integral of the Second Kind} \tag{12}$$

$$k'^2 = \frac{4ar}{[(a+r)^2+z^2]}, \text{ Elliptical Integral Modulus} \tag{13}$$

The elliptical integral values are frequently calculated from approximate numeric methods for the level of accuracy necessary.

For this example the outer permanent magnet radius is used for the loop radius. Figure 14 shows that the radial field is strongest adjacent to the loop and goes to zero at a far distance from the loop. It also coincides with the expectation along the axial center line that the radial flux will be zero. Figure 15 depicts the change of axial field direction from the loop interior to the loop exterior. Figure 16 combines these two graphs into a vector plot, depicting the strong field close to the loop interior and how the flux lines form a path around the wire loop.

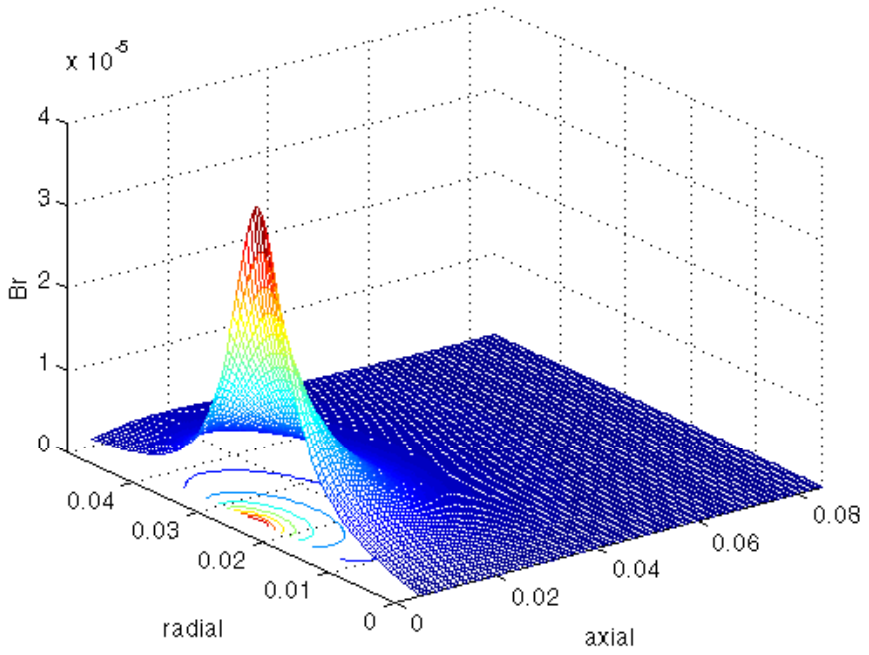

Figure 14: Radial Magnetic Flux Density from Current Carrying Loop

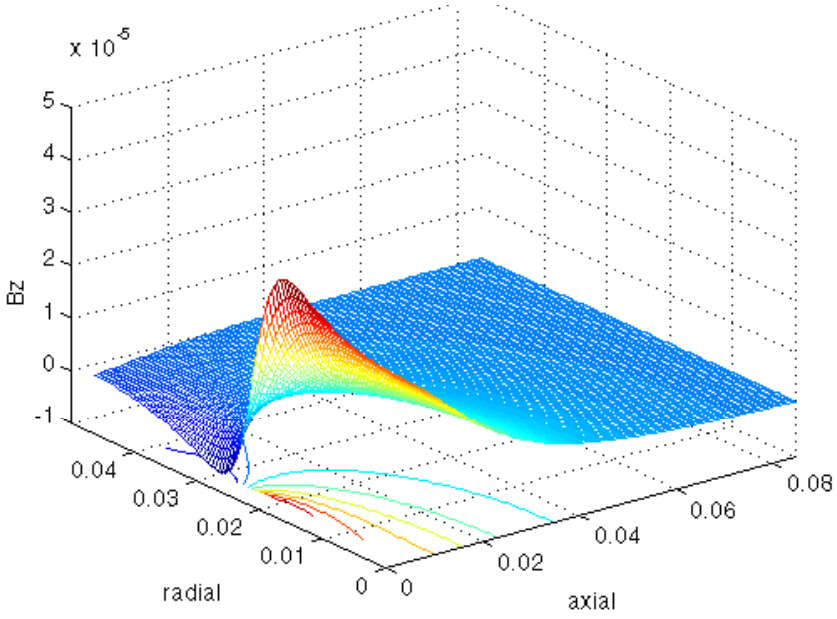

Figure 15: Axial Magnetic Flux Density from Current Carrying Loop

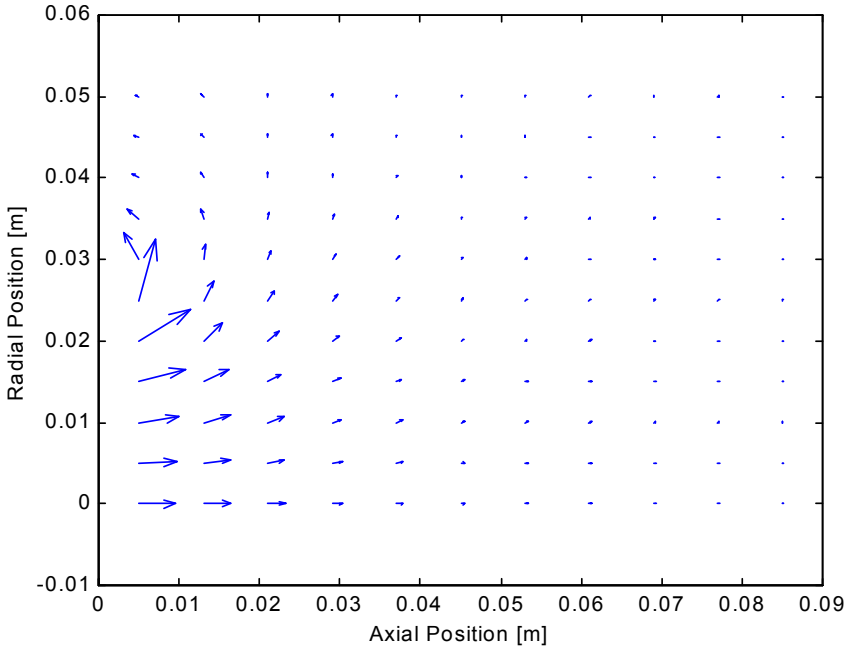

Figure 16: Magnetic Flux Density Field from Current Carrying Loop

Magnetic Flux Density from Current Carrying Coil

The first component field of interest is that caused by the coil. This is calculated by summing the individual loops contributions from a simple elemental loop. The extension for taking in account the entire coil involves the integration of Equation (9) & (10).

$$B_{esr}(r,z,I) = \mu_0 i F_{esr}(r,z) \tag{14}$$

$$B_{esz}(r,z,I) = \mu_0 i F_{esz}(r,z) \tag{15}$$

The current density, i, is calculated using N (the number of wire turns) and I (the coil current) in addition to the geometric parameters.

$$i = \frac{NI}{\left[(a_5 - a_3)(z_4 - z_3)\right]} \tag{16}$$

The geometric function is integrated over the bounds of the coil,

$$F_{esr}(r,z) = \int_{a_3}^{a_5}\int_{Z_3}^{Z_4} f_r(a,r,z-\xi)\,d\xi\,da \tag{17}$$

$$F_{esz}(r,z) = \int_{a_3}^{a_5}\int_{Z_3}^{Z_4} f_z(a,r,z-\xi)\,d\xi\,da \tag{18}$$

For the simulation parameters, the graphs are depicted in Figure 17 & Figure 18. The origin is located at the axis shown in Figure 11, while the coil is located beyond the gap by the distance $(z_3 - z_1)$. Examining Figure 17, moving along the center line, the radial magnetic flux is zero. Following the radial magnetic flux closest to the coil a peak exists while over the coil and then the flux decreases towards zero in either radial direction. Figure 18 shows the axial magnetic flux density. The axial magnetic flux is constant close to the coil interior. It is also seen that the magnetic flux density on the coil interior and coil exterior have opposite signs, as would be expected to complete the flux paths. Figure 19 shows the vector field produced.

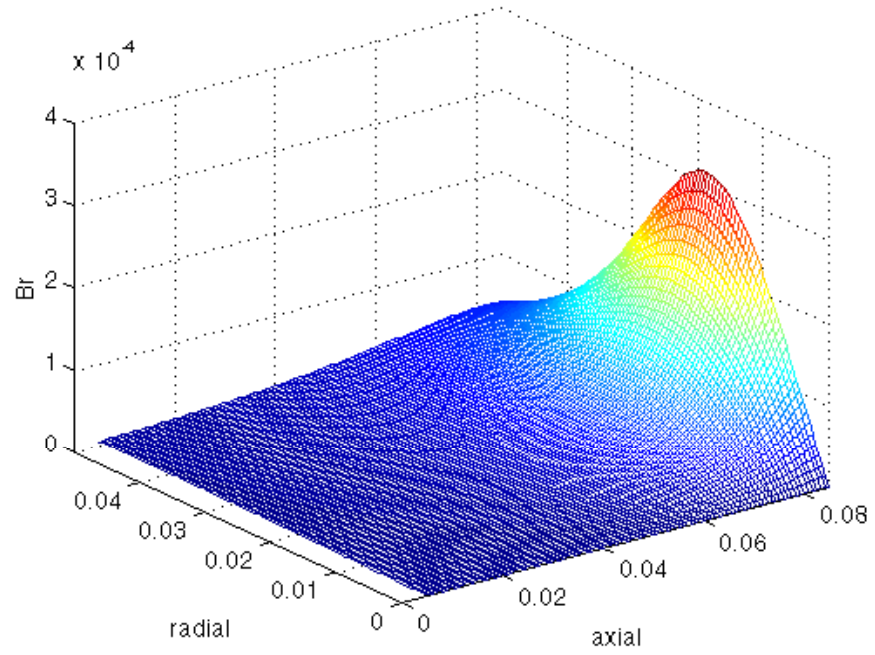

Figure 17: Radial Magnetic Flux Density from Current Carrying Coil

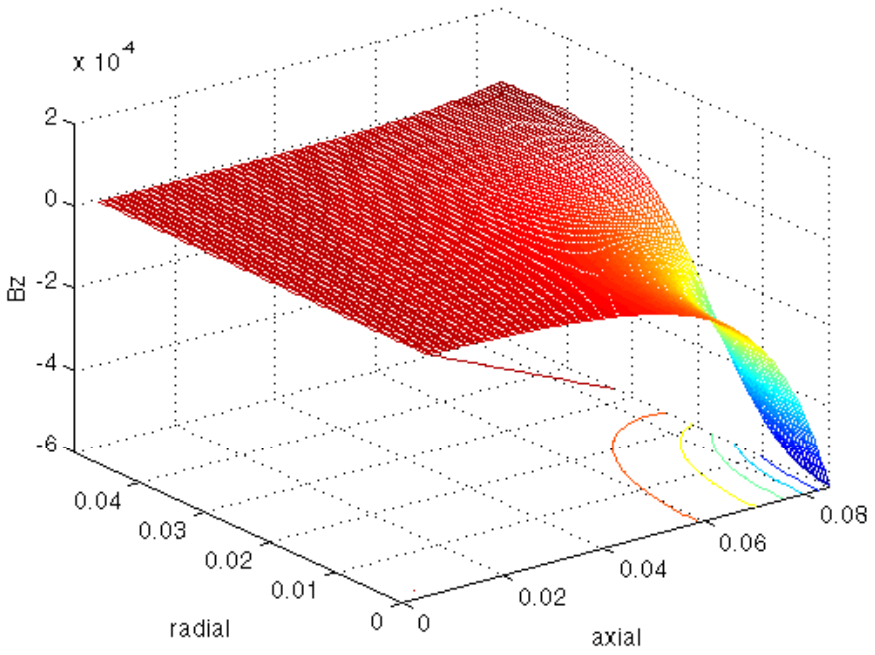

Figure 18: Axial Magnetic Flux Density from Current Carrying Coil

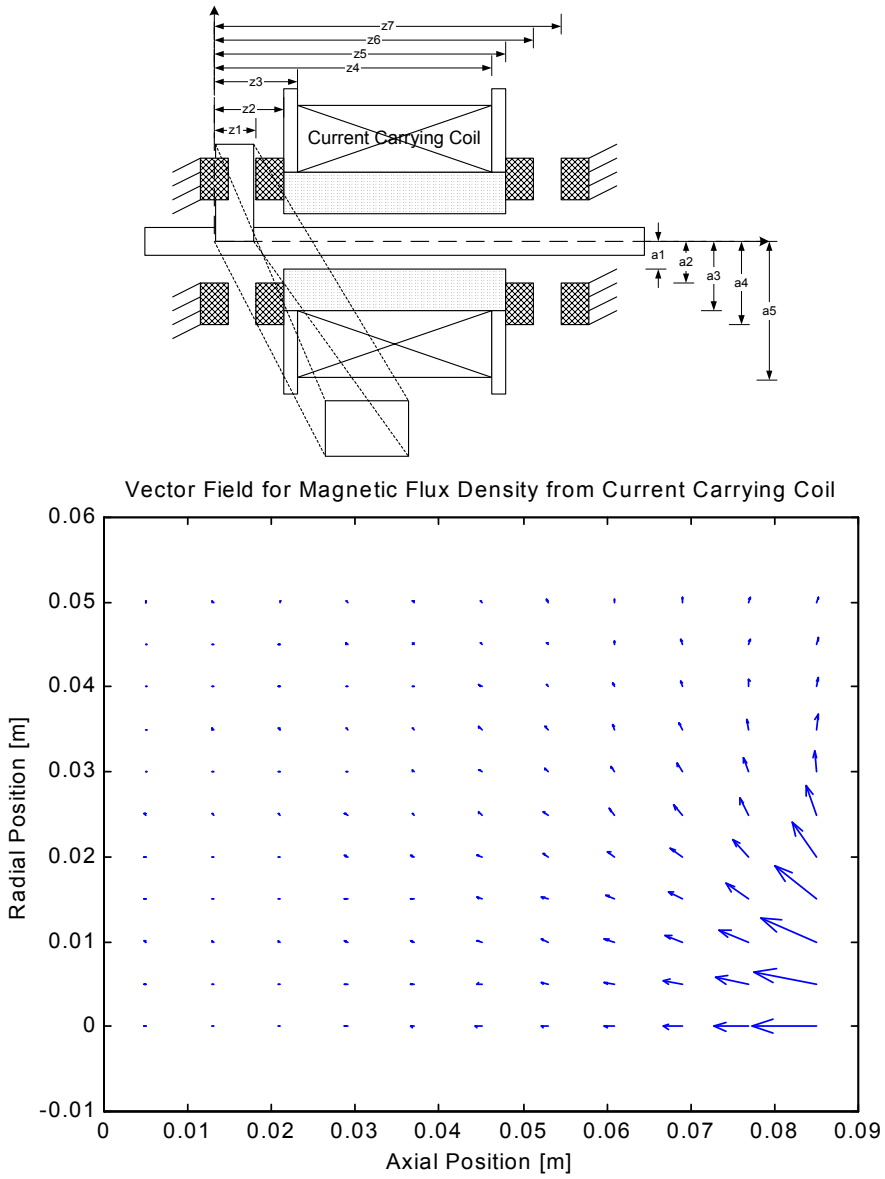

Figure 19: Vector Field of Magnetic Flux Density from Current Carrying Coil

Magnetic Flux Density from Core within Current Carrying Coil

The next constituent field evaluated is that from the core material present. The magnetic field from the current will interact with the core to provide a stronger magnetic field if the core is a ferromagnetic material. A simplifying assumption is that the magnetic field is uniform though out the core. The average of three locations will be used to represent that strength of the field without a core present. Using the apparent permeability, μ', the magnetic field is calculated as

$$H_0(z) = B_0(I)/\mu' \tag{19}$$

Given that the core has a large permeability, the magnetic strength is expressed as

$$J_{ce}(I) = B_0(I)/n \tag{20}$$

Where n is the demagnetizing factor and B_0 is the mean value of B_z. The magnetic flux density can then be expressed as

$$B_{ecr}(r,z,I) = J_{ce}(I)F_{ecr}(r,z) \tag{21}$$

$$B_{ecz}(r,z,I) = J_{ce}(I)F_{ecz}(r,z) \tag{22}$$

$$F_{ecr}(r,z) = \int_{Z_2}^{Z_5}\left[f_r(a_3,r,z-\xi) - f_r(a_1,r,z-\xi)\right]d\xi \tag{23}$$

$$F_{ecz}(r,z) = \int_{Z_2}^{Z_5}\left[f_z(a_3,r,z-\xi) - f_z(a_1,r,z-\xi)\right]d\xi \tag{24}$$

Figure 20 shows that for an annulus core, the radial flux lines are strongest over the core material. This appears in the graph as the radial flux peak location between the core's radial position of 6.4 mm and 12.7 mm. Figure 21 shows that the axial magnetic flux changes signs between the inside and outside of the core material. This is seen along the axial maximum position by the large negative value it the small radial position and the small positive value along the maximum radial position. The change of sign is expected so that the flux path completes itself.

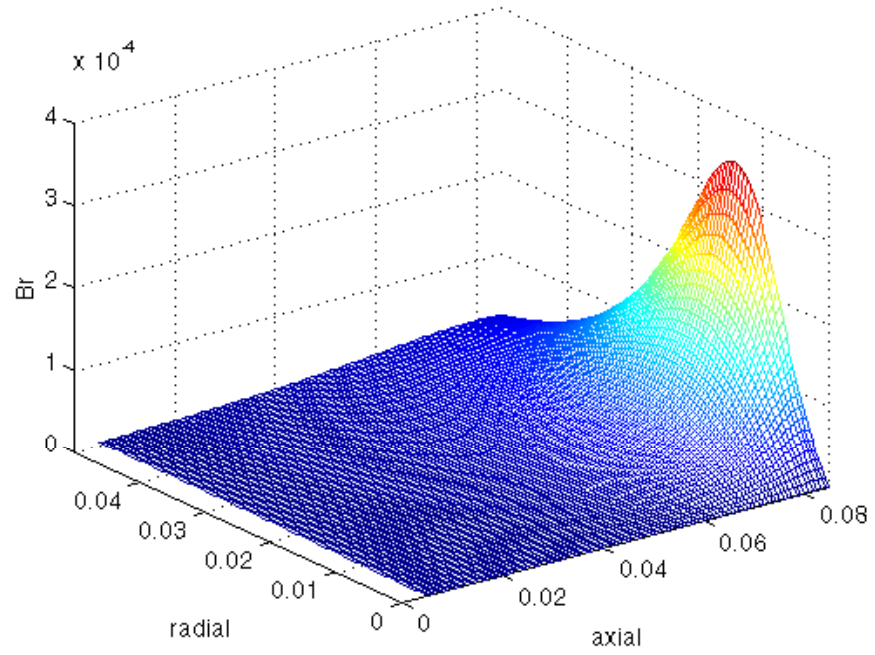

Figure 20: Radial Magnetic Flux Density from Core within Current Carrying Coil

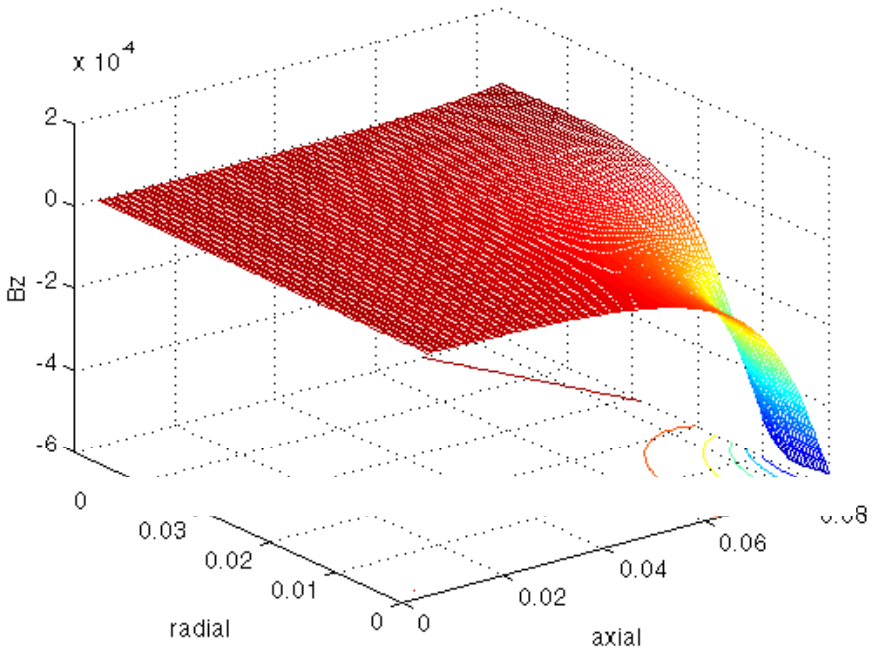

Figure 21: Axial Magnetic Flux Density from Core within Current Carrying Coil

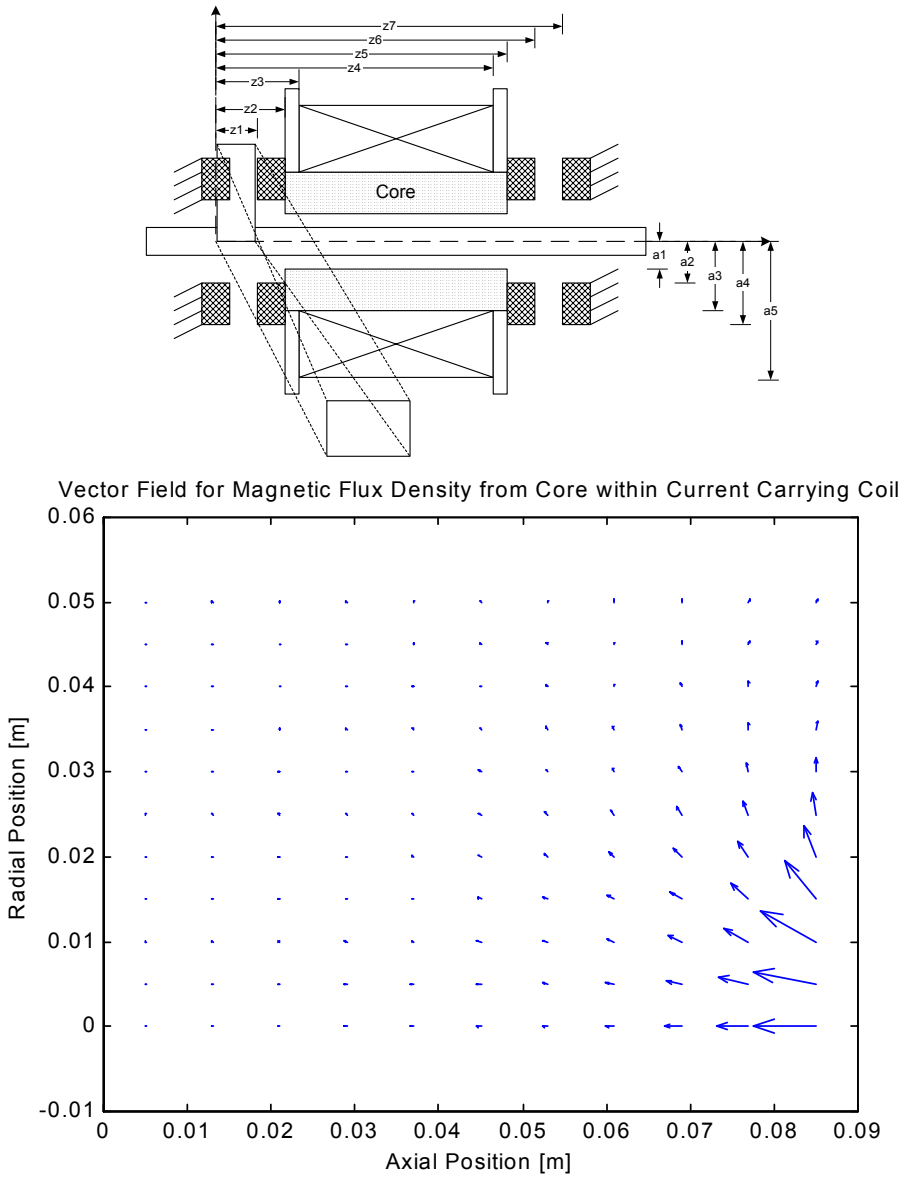

Figure 22: Vector Field of Magnetic Flux Density from Core within Current Carrying Coil

Magnetic Flux Density from Permanent Magnet Attached to Core

The third flux contribution to examine is the moving permanent magnet. Since the core and the permanent magnet are in contact, the permanent magnet magnetizes the core. The magnetic flux from the permanent magnet is

$$\Phi_p = 2\pi J_0 G_p \tag{25}$$

The magnetic flux from the core is

$$\Phi_{cp} = 2\pi J_{cp} G_{cp} \tag{26}$$

Where the geometry dictates,

$$G_P = \sqrt{G_{\mathrm{Pr}}^2 + G_{Pz}^2} \tag{27}$$

$$G_{cP} = \sqrt{G_{c\,\mathrm{Pr}}^2 + G_{cPz}^2} \tag{28}$$

$$G_{\mathrm{Pr}} = \int_{a_2}^{a_4}\int_{Z_1}^{Z_2}\left[f_r(a_4, r, Z_1 - \xi) - f_r(a_2, r, Z_1 - \xi)\right] r\,d\xi\,dr \tag{29}$$

$$G_{Pz} = \int_{a_2}^{a_4}\int_{Z_1}^{Z_2}\left[f_z(a_4, r, Z_1 - \xi) - f_z(a_2, r, Z_1 - \xi)\right] r\,d\xi\,dr \tag{30}$$

$$G_{c\,\mathrm{Pr}} = \int_{a_1}^{a_3}\int_{Z_2}^{Z_5}\left[f_r(a_3, r, Z_1 - \xi) - f_r(a_1, r, Z_1 - \xi)\right] r\,d\xi\,dr \tag{31}$$

$$G_{cPz} = \int_{a_1}^{a_3}\int_{Z_2}^{Z_5}\left[f_z(a_3, r, Z_1 - \xi) - f_z(a_1, r, Z_1 - \xi)\right] r\,d\xi\,dr \tag{32}$$

The electromagnetic leakage between the surfaces provide a reduction in flux:

$$\Phi_{cp} = (1 - \nu)\Phi_p \tag{33}$$

$$J_{cP} = \frac{G_P (1 - \nu) J_0}{G_{cP}} \tag{34}$$

The magnetic flux density at an arbitrary point P is

$$B_{\mathrm{Pr}}(r, z) = J_0 \cdot F_{\mathrm{Pr}}(r, z) + J_{cP} \cdot F_{ecr}(r, z) \tag{35}$$

$$B_{Pz}(r, z) = J_0 \cdot F_{Pz}(r, z) + J_{cP} \cdot F_{ecz}(r, z) \tag{36}$$

$$F_{\mathrm{Pr}}(r, z) = \int_{Z_1}^{Z_2}\left[f_r(a_4, r, z - \xi) - f_r(a_2, r, z - \xi)\right] d\xi \tag{37}$$

$$F_{Pz}(r, z) = \int_{Z_1}^{Z_2}\left[f_z(a_4, r, z - \xi) - f_z(a_2, r, z - \xi)\right] d\xi \tag{38}$$

Figure 23 demonstrates the radial magnetic flux from the permanent magnet/core combination. The permanent magnet near edge is positioned at 80 mm. As expected the radial field reverses between the interior and exterior of the permanent magnet. Figure 24 demonstrates the axial magnetic flux and how on both the interior and exterior it is in the same direction, yet over the permanent magnet it is

the opposite direction, thereby completing the flux path. Figure 25 shows the vector field eminating from the magnet and encircling the magnet on the outside and through the interior.

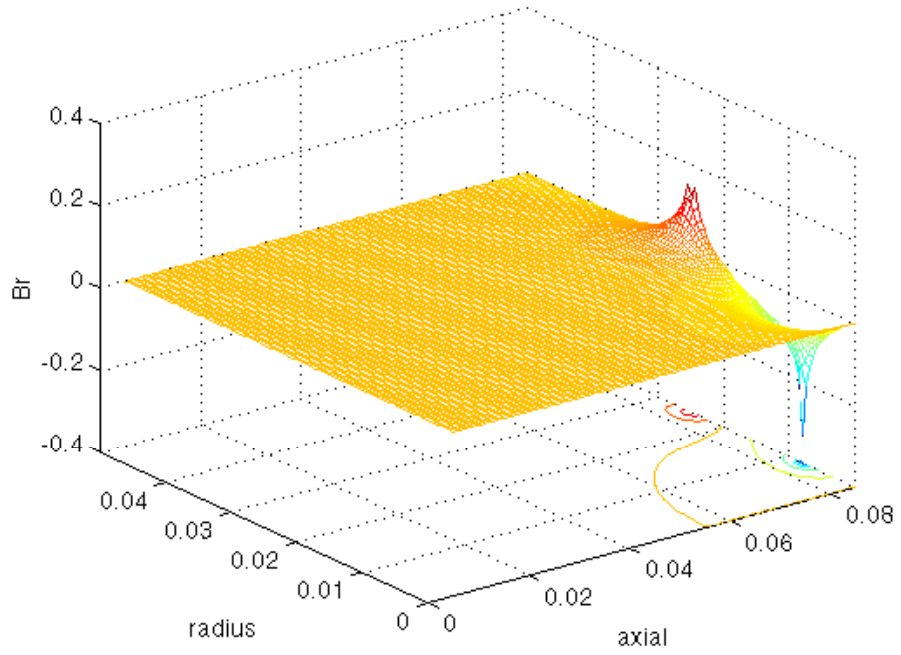

Figure 23: Radial Magnetic Flux Density from Permanent Magnet Attached to Core

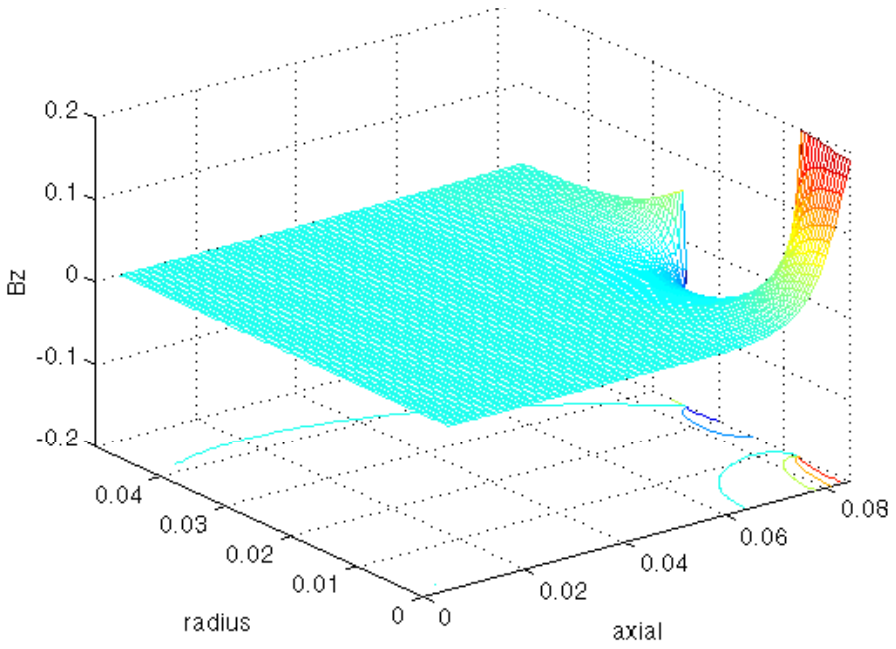

Figure 24: Axial Magnetic Flux Density from Permanent Magnet Attached to Core

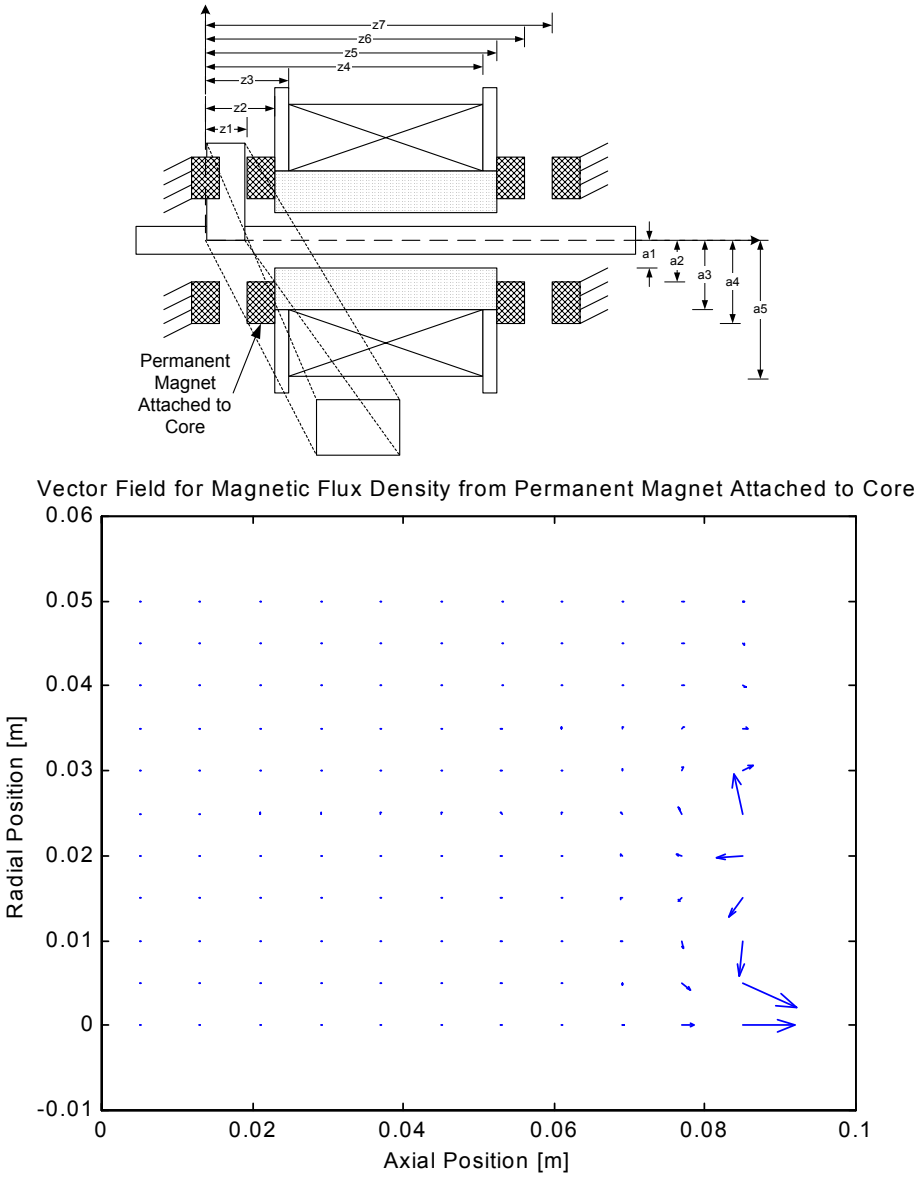

Figure 25: Vector Field of Magnetic Flux Density from Permanent Magnet Attached to Core

Magnetic Flux Density from Stationary Permanent Magnet

The final component contribution is that of the stationary permanent magnet. In this situation the magnet center is bisected by the axial origin. The magnetic flux density from the separated magnet are

$$B_{mr}(r,z) = -J_0 \cdot F_{mr}(r,z) \tag{39}$$

$$B_{mz}(r,z) = -J_0 \cdot F_{mz}(r,z) \tag{40}$$

$$F_{mr}(r,z) = \int_{-t/2}^{t/2} \left[f_r(a_4, r, z-\xi) - f_r(a_2, r, z-\xi) \right] d\xi \tag{41}$$

$$F_{mz}(r,z) = \int_{-t/2}^{t/2} \left[f_z(a_4, r, z-\xi) - f_z(a_2, r, z-\xi) \right] d\xi \tag{42}$$

Figure 26 shows the radial flux produced from a single magnet, similar to Figure 23, simply the magnet placement has changed. Figure 27 shows the axial magnetic flux produced from a single magnet. Note how the interior and exterior have axial flux in the same direction while the flux path is completed as it returns to the magnet above the annulus. Figure 28 depicts the vector field produced from the stationary permanent magnet.

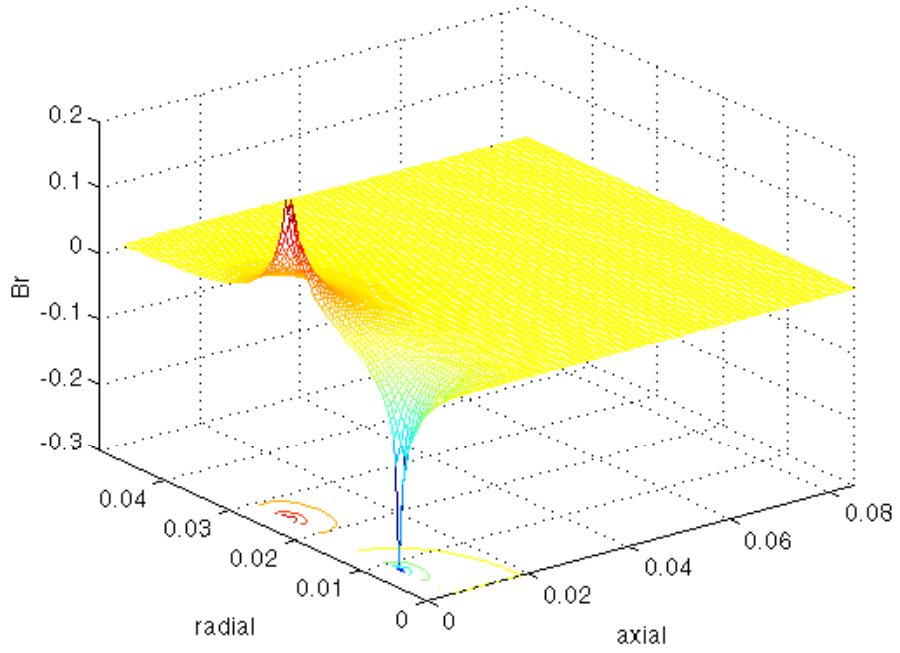

Figure 26: Radial Magnetic Flux Density from Separated Permanent Magnet

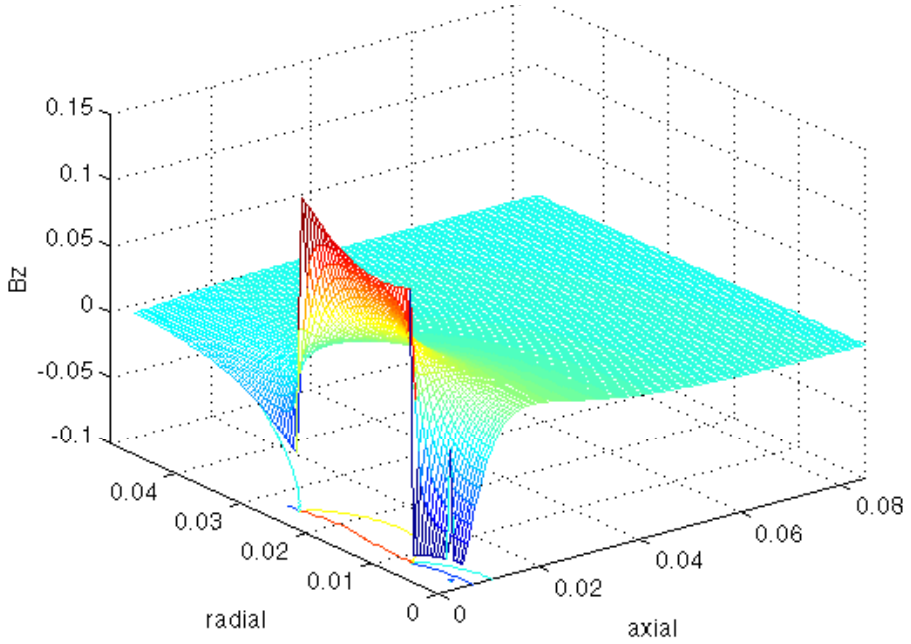

Figure 27: Axial Magnetic Flux Density from Separated Permanent Magnet

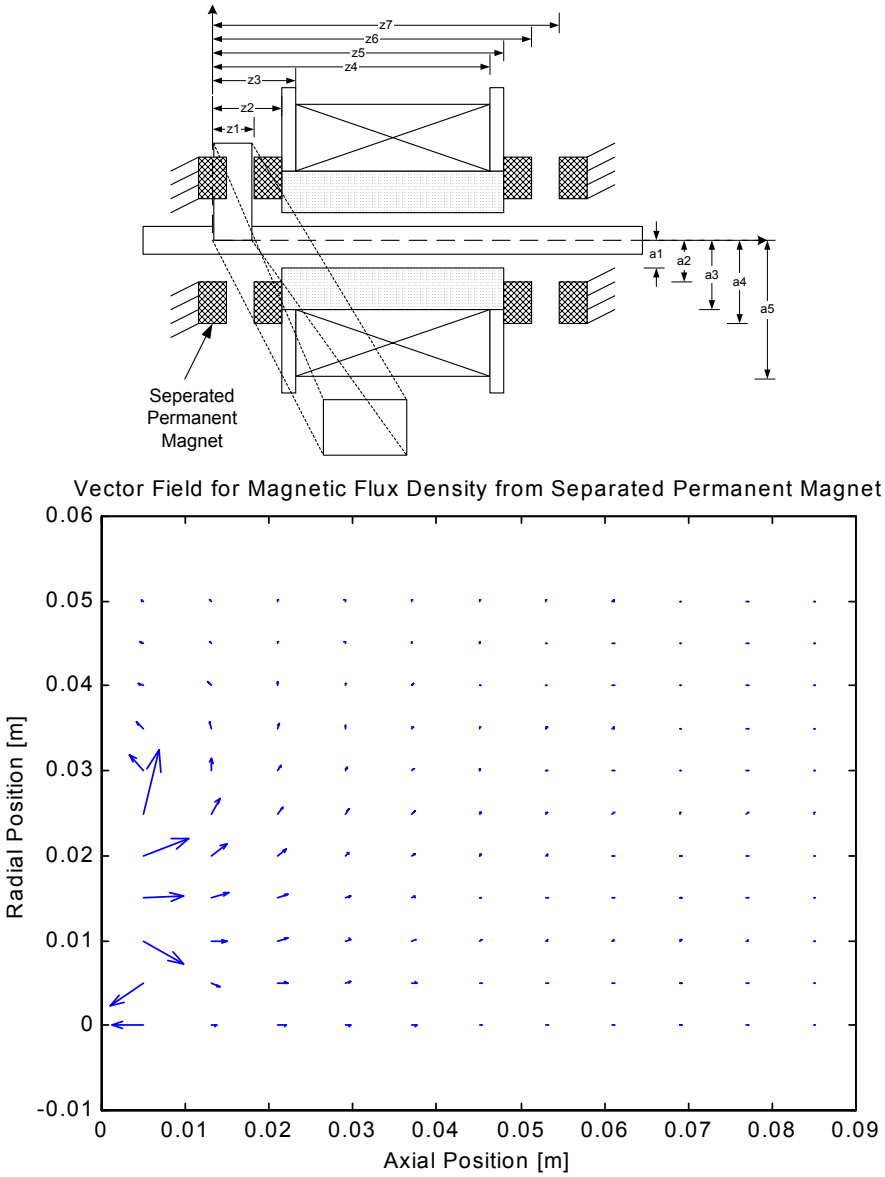

Figure 28: Vector Field of Magnetic Flux Density from Separated Permanent Magnet

Total Magnetic Flux Density

This segment combines the electromagnetic fields produced by the four constituent components. The magnetic flux may be summed from each of the components.

$$B_r(r,z,I) = +B_{ecr}(r,z,I) + B_{esr}(r,z,I) + B_{mr}(r,z) + B_{\mathrm{Pr}}(r,z) \tag{43}$$

$$B_z(r,z,I) = +B_{ecz}(r,z,I) + B_{esz}(r,z,I) + B_{mz}(r,z) + B_{Pz}(r,z) \tag{44}$$

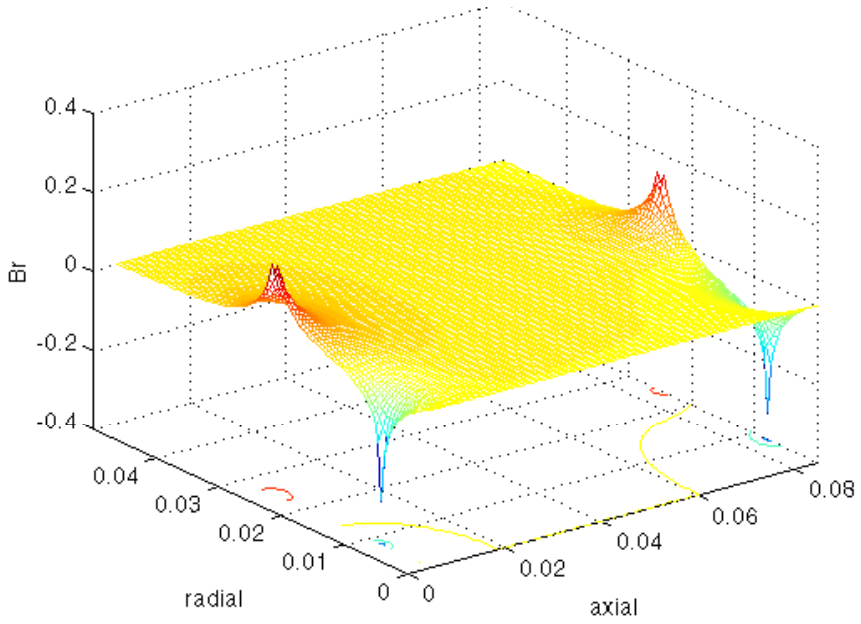

Figure 29: Total Radial Magnetic Flux Density

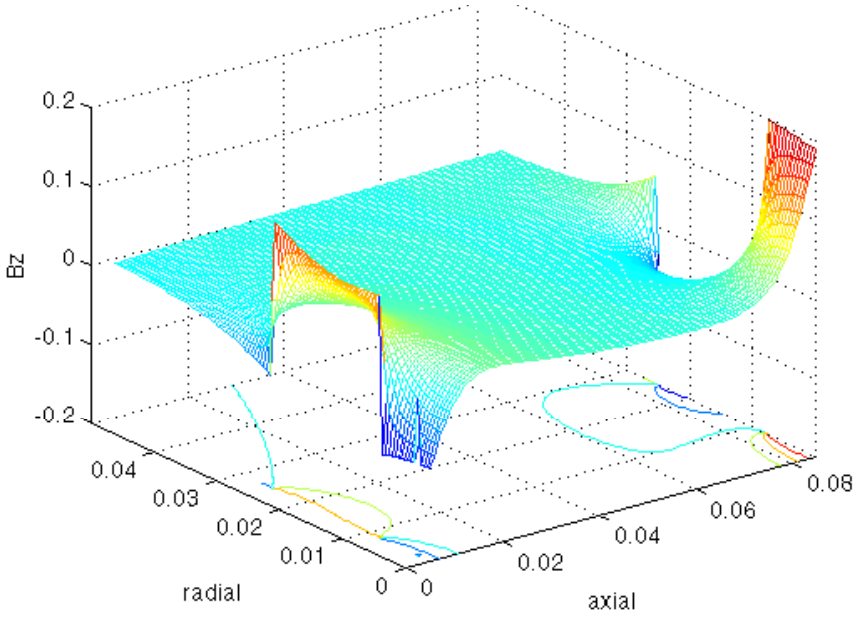

Figure 30: Total Axial Magnetic Flux Density

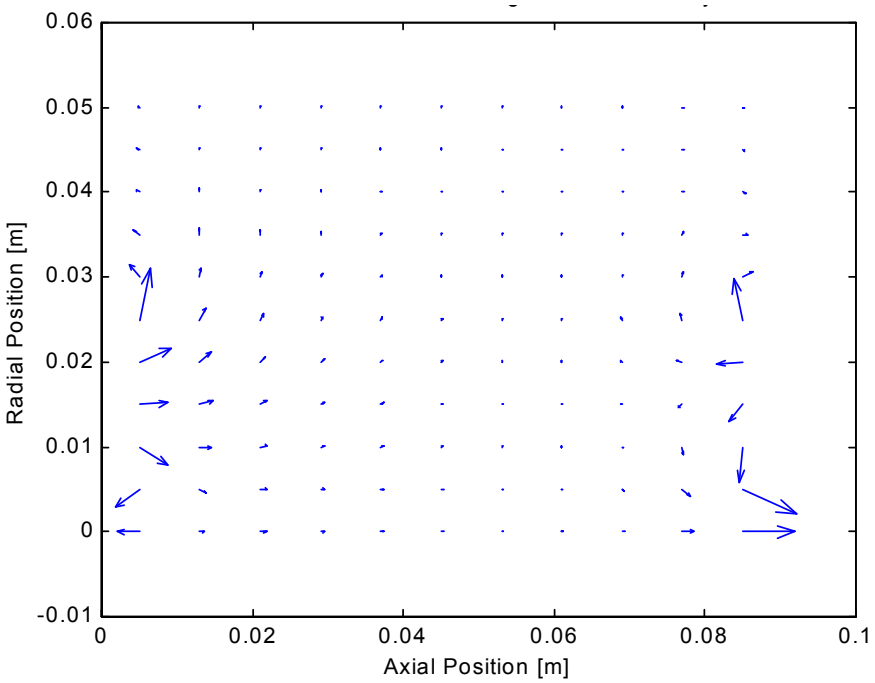

Figure 31: Vector Field of Total Magnetic Flux Density

Figure 29 depicts the total radial magnetic flux density between the stationary magnet and the absorber mass. Figure 30 depicts the total axial magnetic flux density between the stationary magnet and the absorber mass. Figure 31 shows the complete vector field. This numeric representation of the field may be used to calculate the force in the next chapter.

Summary

This chapter has developed the full electromagnetic field relations between the absorber electromagnet and the stationary permanent magnet. This relationship consists of the superposition of the four constituent fields: the coil, core, absorber permanent magnet and the stationary permanent magnet. These equations also takes advantage of the fact that the system is axial symmetric.

Now that the full field is known the force between the stationary permanent magnet and the absorber can be examined for different gaps. The electromagnetic fields may be summed with various gaps to examine how the fields interact. These fields will be examined in the following chapter to arrive at the force to gap relationship.

The electromagnetic field has been solved so that the force between the absorber and stationary magnets may be calculated. This field equation will allow the force to distance function to be identified and simulated so that the system response can be found using the nonlinear spring relation. The electromagnet field is dominated by the permanent magnet strength, yet the small variation with current will allow small changes in the transfer function of the combined system.

CHAPTER 4. ELECTROMAGNETIC FORCE FORMULATION

This chapter develops the theoretical force relationships between the absorber and the stationary magnet. It takes the component electromagnetic fields developed in Chapter 3 while varying the current or gap to calculated the total electromagnetic field. Using this total electromagnetic field the chapter determines the force relationship using tensor notation.

Force Derivation from Magnetic Flux Density

This section evaluates the force on a volume, given the magnetic flux density. It begins with a review of the Lorentz force material covered in Woodson and Melcher.[51] This law relates the force on a moving charge while it passes though an electromagnetic field.

The Lorentz force gives the magnetic force on a charge q moving with velocity $\vec{v}$ as

$$\vec{f} = q\vec{v} \times \vec{B} \tag{45}$$

From this we may calculate the force density $\vec{F}$ as

$$\vec{F} = \lim_{\delta V \to 0} \frac{\sum_i \vec{f}_i}{\delta V} = \lim_{\delta V \to 0} \frac{\sum_i q_i \vec{v}_i \times \vec{B}_i}{\delta V} \tag{46}$$

Assuming that all particles experience the same flux density, $\vec{B}$, the definition of free current density can be used to write

$$\vec{F} = \vec{J}_f \times \vec{B} \tag{47}$$

This derivation relies on the fact that the averaging process makes Equation (46) and (47) consistent. Using the constituent relation,

$$\vec{B} = \mu\vec{H} \tag{48}$$

and Ampere's law for magnetic field systems, Equation (47) becomes

$$\vec{F} = \mu\left(\nabla \times \vec{H}\right) \times \vec{H} \tag{49}$$

Alternatively this expression may be expressed as

$$\vec{F} = \mu\left(\vec{H}\cdot\nabla\right)\vec{H} - \frac{\mu}{2}\nabla\left(\vec{H}\cdot\vec{H}\right) \tag{50}$$

Using tensor notion this equation may be expressed with Maxwell's stress tensor as

$$F_m = \frac{\partial T_{mn}}{\partial x_n} \tag{51}$$

The tensor elements are

$$T_{mn} = \mu H_n H_m - \frac{\mu}{2}\delta_{mn} H_k H_k \tag{52}$$

The stress tensor may alternatively be expressed in cylindrical coordinates r, Θ, and z.

$$T_{PQ} = \begin{bmatrix} T_{rr} & T_{r\Theta} & T_{rz} \\ T_{\Theta r} & T_{\Theta\Theta} & T_{\Theta z} \\ T_{zr} & T_{z\Theta} & T_{zz} \end{bmatrix} \tag{53}$$

In our case

$$T_{PQ} = \frac{1}{\mu_0}\begin{bmatrix} (B_r^2 - B_\Theta^2 - B_z^2)/2 & B_r B_\Theta & B_r B_z \\ B_\Theta B_r & (B_\Theta^2 - B_z^2 - B_r^2)/2 & B_\Theta B_z \\ B_z B_r & B_z B_\Theta & (B_z^2 - B_r^2 - B_\Theta^2)/2 \end{bmatrix} \tag{54}$$

Through manipulation the force component may be expressed as a surface integral or this stress tensor.

$$f_m = \oint_S T_{mn} n_n da \tag{55}$$

This allows the force calculation given the magnetic flux field encircling the object. This relation may now be used to find the force between the electromagnetic absorber and the stationary permanent magnet.

Force on Vibration Absorber

This general relation may now be applied to the current case in calculating the levitation force R_f as

$$R_f = -F_z = \oint_S (T_{zr} n_r + T_{z\Theta} n_\Theta + T_{zz} n_z) dS \tag{56}$$

To simplify the expression consider the point $S(0, Z_m)$, along the actuator axis, where the axial magnetic flux density is zero $(B_z = 0)$, for convenience. Taking the plane, including the point S and being normal to the z-axis, the components of the vector become $n_r = n_\Theta = 0$. Since the magnetic

field is symmetrical about the z-axis, the magnetic flux densities in the tangential direction become $B_\Theta = 0$. This yields

$$R_f = -\frac{\pi}{\mu_0}\int_0^\infty r(B_z^2 - B_r^2)dr \tag{57}$$

The force is calculated from the integral across the entire plane, as seen by the bounds of integration. The other surface integral segments encircling the volume may be taken at a large distance and this will result in zero magnetic flux and therefore no force contribution. As long as the magnetic field is small at the maximum radius selected one may approximate the entire plane. By reviewing the fields shown in the prior chapter one sees that they are a small contributions once beyond twice the permanent magnet radius. Therefore this integral may be numerically evaluated using the determined electromagnetic fields.

Using the simulation parameters while changing the displacement one can find the force verses displacement relationship for zero current. The reference point is the center of the fixed magnet. This is depicted in Figure 32 with three curve fits. Polynomial curve fits were calculated. The sixth and seventh order polynomial fits are depicted as close representations. The inverse square is a simpler model with a high relation to the theoretic force. Figure 33 depicts the standard deviation of the error terms for different polynomial orders. As expected this decreases as additional terms are added.

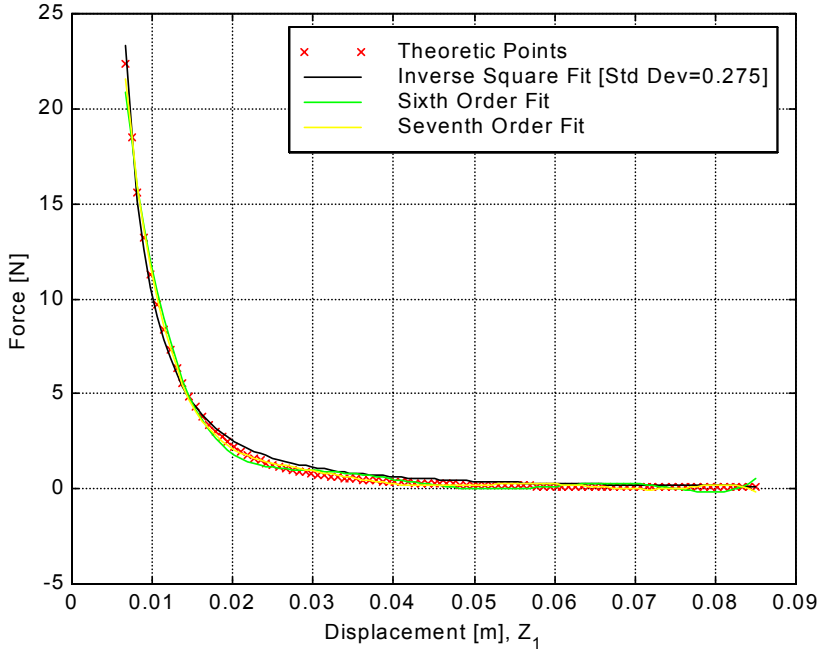

Figure 32: Force relationship for no current with variable gap

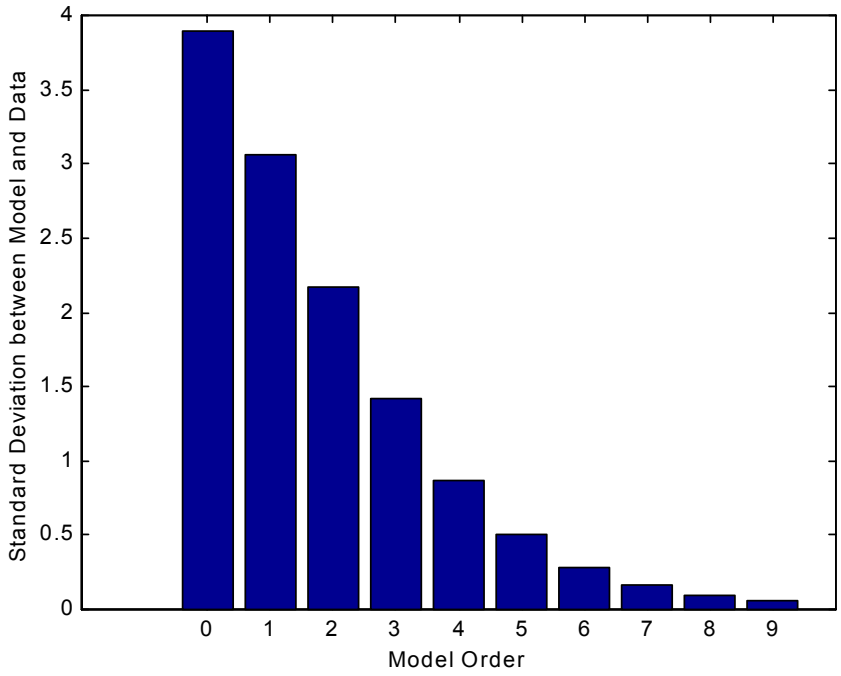

Figure 33: Standard Deviation of error terms for various polynomial curve fits

Although the polynomial fits have less standard deviation with increased order, these fits are very specific to the range selected and at larger distances fail to represent the force and diverge from the smooth extrapolation. This leads to examining alternative models. Table 2 lists the standard deviation of the error terms for the polynomial models and then examines using the models $B_{-1}Z_1^{-1}$ (inverse), $B_{-2}Z_1^{-2}$ (inverse square), and $B_{-3}Z_1^{-3}$ (inverse cube). It is clear from the error terms standard deviation that the inverse square is an appropriate model. The sixth order or larger polynomial has less deviation of the error term, yet it does not properly model the expectation beyond the fit range and also uses seven degrees of freedom to calculate this polynomial. With the inverse square model only one degree of freedom is used and the standard deviation is less than the fifth order polynomial and the model corresponds to the expected extrapolation. The inverse square model will be the preferred model for the remaining modeling.

Table 2: Standard Deviation of error terms

Polynomial Order	Standard Deviation of Error Terms
Constant	3.897
1	3.067
2	2.172
3	1.418
4	0.867
5	0.505
6	0.286
7	0.162
8	0.094
9	0.056
Inverse only	2.064
Inverse square	0.275
Inverse Cube only	1.092

Force Level with Current Variation

The force levels will be examined with varying current into the electromagnetic absorber. Figure 34 depicts the force relationship with +1 amp, while Figure 35 depicts the force relationship with -1 amp. Both of these cases result in appropriate fits with the inverse square fit. The inverse square curve fits are tabulated in Table 3 across various current levels. The 95% confidence bounds cover a 2.2% parameter variation of B_{-2}. The residual's standard deviation shows that the inverse square model is appropriate with the current supply variation. This table shows that with 10 amps it is possible to change the fit coefficient by 7.63%.

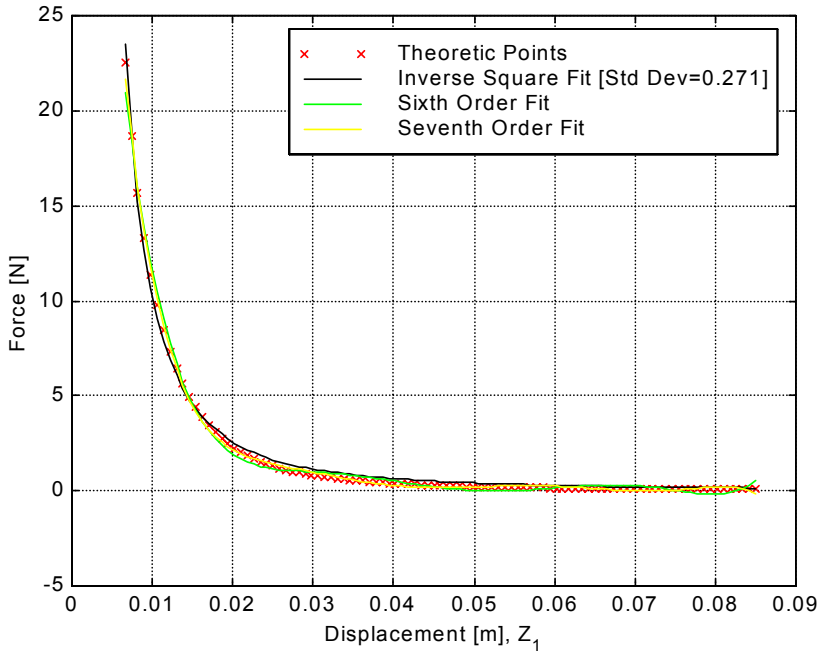

Figure 34: Force relationship for fixed current with variable gap [1 Amp]

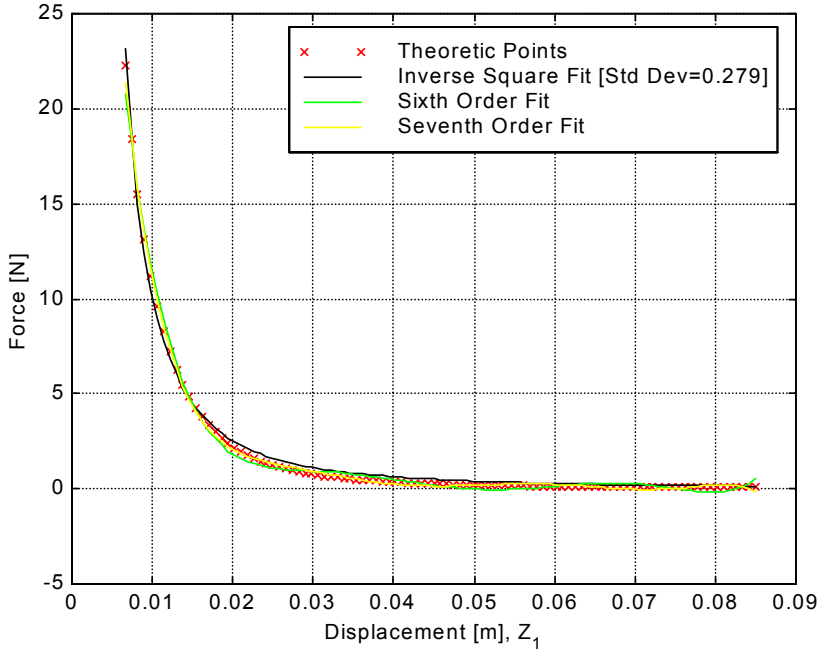

Figure 35: Force relationship for fixed current with variable gap [-1 Amp]

Table 3: Inverse Square Curve Fit Parameters $B_{-2}Z_1^{-2}$ [Leakage = 0.809]

Current [Amps]	Fit Coefficient B_{-2} [$x10^{-3}$ Nm^2]	95% Confidence Bound Range on B_{-2} [$x10^{-3}$ Nm^2]	Standard Dev for Regression Model Residuals (s)	Coefficient Change from Zero Amps [%]
10	1.095	0.0153	0.285	7.63
5	1.057	0.0144	0.267	3.82
3	1.041	0.0144	0.267	2.29
2	1.033	0.0145	0.259	1.53
1	1.025	0.0146	0.271	0.76
0	1.018	0.0148	0.275	0
-1	1.010	0.0150	0.279	-0.76
-2	1.002	0.0153	0.284	-1.53
-3	0.994	0.0156	0.391	-2.29
-5	0.979	0.0164	0.305	-3.82
-10	0.940	0.0190	0.352	-7.64

Dual-Sided Absorber Force

The curve fits to this point are for the force-distance relationship for a single sided actuator, the force between the electromagnetic actuator and one permanent magnet. The configuration of interest is the dual-sided actuator, depicted in Figure 36. To transform the single sided equations we need to alter

the displacement reference point to the center equilibrium position of the dual-sided actuator. The force equation becomes

$$F = Left\ Side\ Force + Right\ Side\ Force$$
$$F = B_{-2}(x_0 + x)^{-2} - B_{-2}(x_0 - x)^{-2} \tag{58}$$

x_0 is the center equilibrium position measured as Z_1, from the stationary magnet center. While x is the displacement from this equilibrium position. x_0 in the test case is 10.3 mm, with the magnet thickness at 10 mm, the maximum x displacement is 5.3 mm.

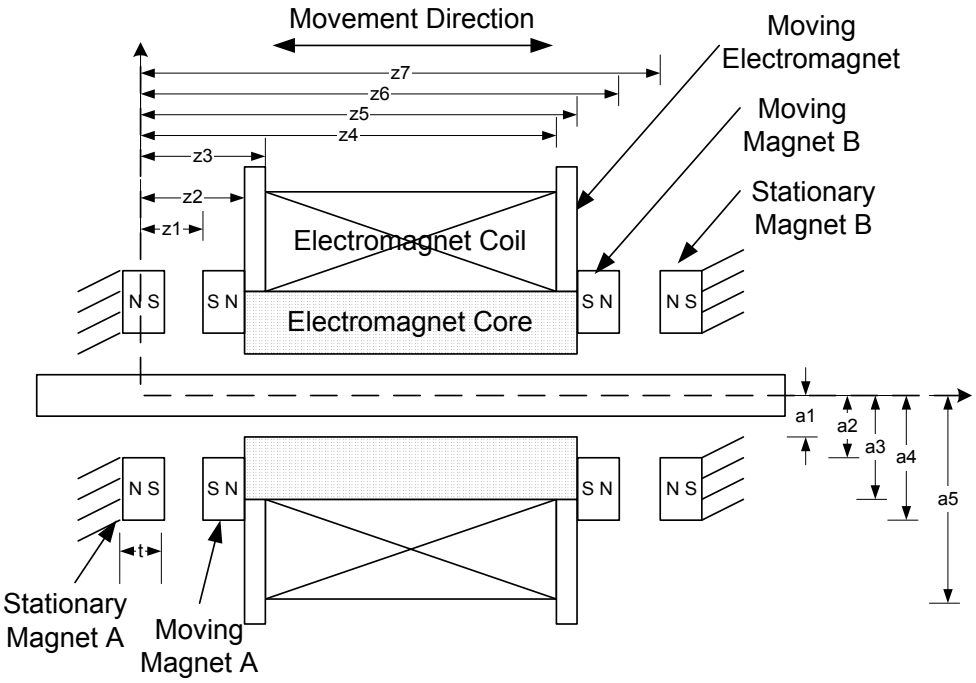

Figure 36: Dual Sided Absorber Configuration

Figure 37 shows the relationship described by Equation (58). The relationship is clearly an odd function [f(x)=-f(-x)] that is linear for small displacements. Although to absorb the primary system's vibration this linear range is expected to be exceeded. Figure 38 is a close up with a smaller area of interest. This shows that the force relationship is very close to linear for quarter of the range of motion. These graphs demonstrate the amount of force variation for various excitation currents.

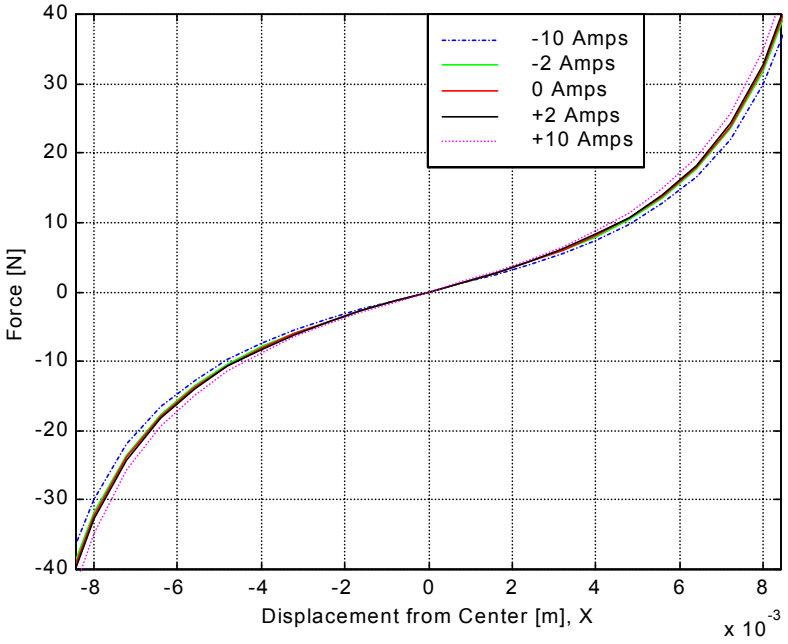

Figure 37: Dual Sided Absorber Force Relationship

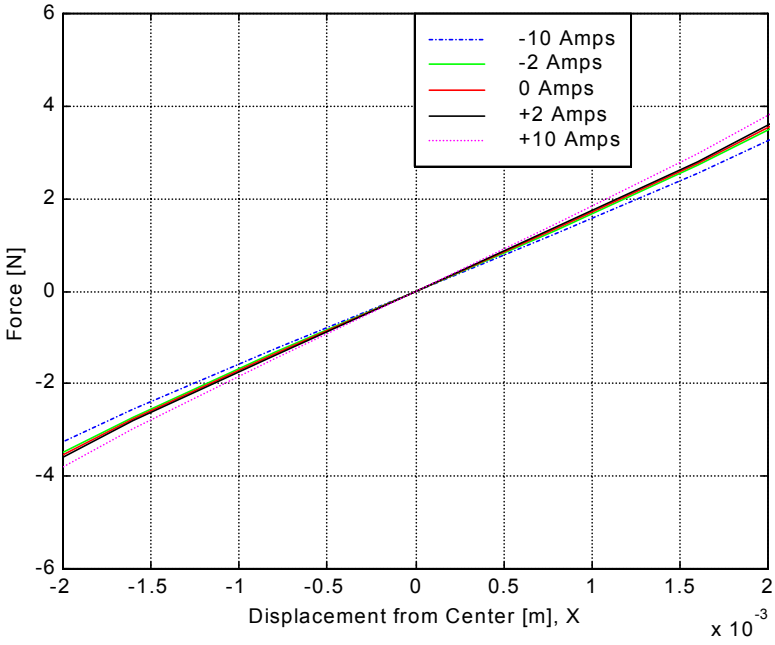

Figure 38: Dual Sided Absorber Force Relationship, Linear Range

Table 4 shows that the force level percentage change is constant for a particular current setting. This force change is directly related to the stiffness change. If the absorber were a linear system it would result in a natural frequency change ($\omega_n = \sqrt{k/m}$), a 7.62% stiffness change would result in a 3.8% natural frequency shift. This small absorber force variation would be adequate to shift the system's transfer function if low damping is present.

Table 4: Force Change for Various Currents

Displacement % of maximum	Displacement [mm]	Force with no Current [N]	Force % Change ±2 Amps	Force % Change ±10 Amps
+90%	+7.58	-27.44	∓1.53%	∓7.62%
+75%	+6.32	-17.51	∓1.53%	∓7.62%
+50%	+4.21	-8.70	∓1.53%	∓7.62%
+25%	+2.10	-3.72	∓1.53%	∓7.62%
0%	0	0	-	-

Force Levels with Variable Gap Spacing

The dual-sided inverse square model is the most appropriate model since a change in gap allows just one parameter to change in Equation (58). Yet this model is not easily contrasted with other known models. Examining the dual-sided force graph, it can be approximated as a Duffing's hardening spring model. The Duffing spring is a linear spring with a cubic term for softening or hardening, as in Equation (59).

$$F_{Duffing} = k_{duffing} x + \mu_{Duffing} x^3 \tag{59}$$

x is the displacement from the center equilibrium location. If $\mu_{Duffing}$ is positive a hardening spring is modeled, if negative a softening spring. These coefficients may be calculated for different gap spacing, yet each gap has unique coefficients.

Figure 39-Figure 41 demonstrate the inverse square relationship and both a linear and Duffing spring fit. The linear fit is calculated across a quarter (¼) of the movement range since this portion visually appears linear (Figure 38). The Duffing spring fit is calculated across the entire movement range. As the gap is widened the Duffing spring approximation deviates from the inverse square relation (Figure 41). Table 5 lists the various Duffing & linear spring constant calculated values for various gaps. It demonstrates that all the spring stiffness estimates soften as the gap is widened.

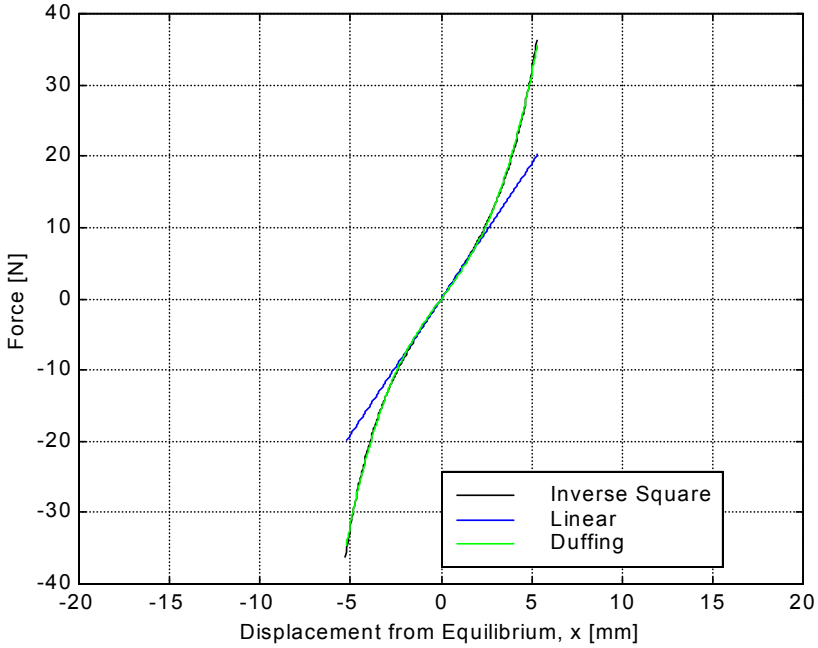

Figure 39: Dual Sided Absorber Force Relationship, Duffing's Approximate

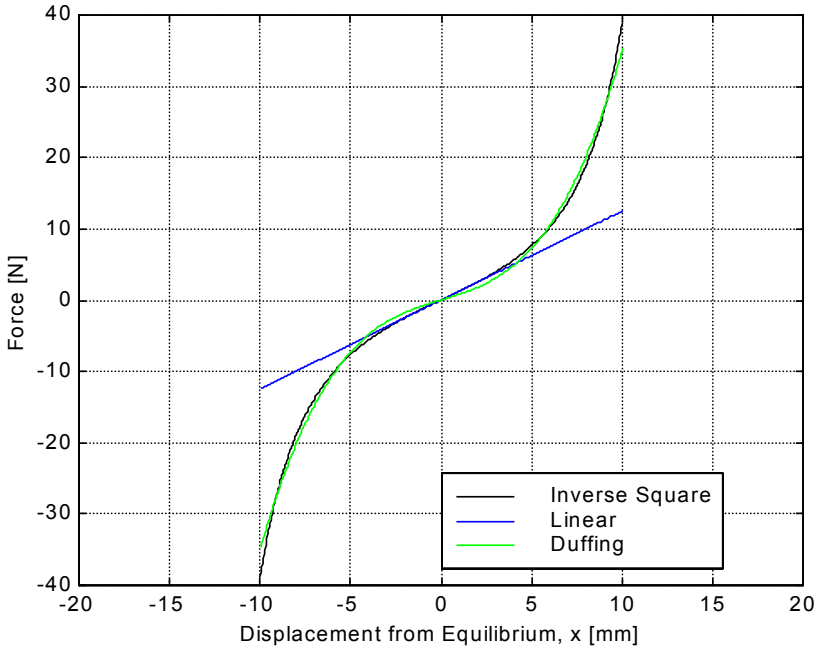

Figure 40: Dual Sided Absorber Force Relationship, Duffing's Approximate

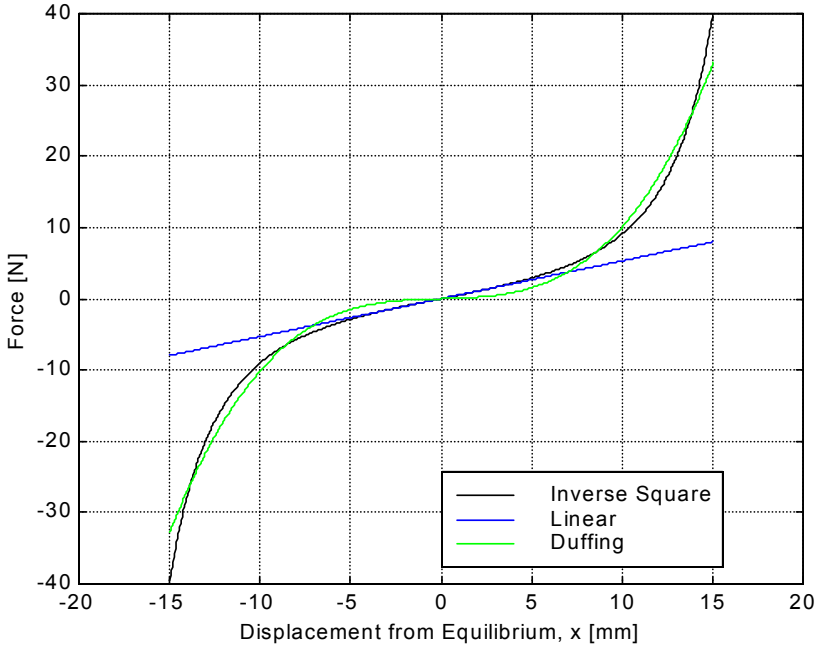

Figure 41: Dual Sided Absorber Force Relationship, Duffing's Approximate

Table 5: Equivalent Spring Stiffness for System

	Duffing Stiffness Elements		Linear
x_0 [mm]	$k_{duffing}$	$\mu_{Duffing}$ [x10^6]	k_{linear} [N/m]
10.3	3430	115	3800
11	2720	89	3130
12	1970	64	2420
13	1440	47	1910
14	1060	36	1530
15	770	27	1250
16	540	22	1030
17	380	17	860
17.2	350	16	830
18	250	14	730
19	160	11	620
19.9	82	9.5	540
20	70	9.4	530

Summary

This chapter takes the electromagnetic fields derived in the prior chapter and determined the force relationship between the absorber mass and the stationary magnet. After the force vs. displacement relation is determined a number of curve fits are examined. The best relation identified is the inverse square relationship for the single sided actuator. For the dual sided actuator the inverse square relation can be used, yet the similarities with a Duffing spring (cubic and linear terms) are presented. These similarities yield a base comparison system that has been investigated in literature. These theoretical relations will be confirmed with experimental tests in Chapter 7. The magnetic spring forces have been developed and the next chapter discusses the damping mechanism.

This chapter has shown the resultant force for the dual-sided absorber may be adjusted with either current variation or gap variation. The current variation has the advantage that it may be rapidly altered, while the gap variation may be altered one time for sustained changes in the transfer function. Both these mechanisms may be used to tune the absorber and lower the resultant vibration of the combined system.

CHAPTER 5. DAMPING MECHANISMS

To properly understand the system dynamics, the damping mechanisms must be examined. This absorber will have a number of damping mechanisms present. Mechanical systems experience varying damping mechanisms, viscous and Coulomb damping will be discussed for this application. The dynamic electromagnetic fields also provides an energy loss mechanism resulting in damping. This chapter presents elementary damping relationship as they relate to this research.

Mechanical Damping

The two primary mechanical damping mechanisms for this experiment are viscous damping and Coulomb damping. Viscous damping will arise when a liquid lubricant is applied to the shaft and bearing. Coulomb damping is caused from the friction between the bearing and the shaft. These mechanical damping mechanisms are quantitatively discussed in this section.

The viscous damping model is a force proportional to the velocity. This is the traditional mechanical damping model and is easily modeled in a differential equation as

$$f_{damp} = c\dot{x} \tag{60}$$

A common method to compare various damping mechanisms is by comparing the energy dissipated per cycle with the viscous model.[52] The viscous model results in the dissipated energy of

$$W_d = \pi c_{eq} \omega X^2 \tag{61}$$

The equivalent viscous damping coefficient, c_{eq}, can be calculated based on other damping mechanisms and used as a comparison metric.

The damping ratio, ζ, is the ratio of the viscous damping coefficient to the critical damping.

$$\zeta = \frac{c}{c_{cr}} = \frac{c}{2\sqrt{km}} \tag{62}$$

When this nondimensional parameter is less than one the time response is oscillatory and when greater than one it becomes nonoscillatory. This value influences the decay envelope of the system time

response. It was mentioned in reviewing the transfer functions than low damping is better for the research absorber since it allows increased attenuation over a smaller frequency band.

The friction between the bearing and the shaft create another form of mechanical damping. The bearing has a Teflon™ insert to minimize this friction. Yet significant mechanical damping is found present in the experimental tests. The equivalent viscous damping coefficient for Coulomb friction is

$$c_{eq} = \frac{4F_d}{\pi\omega X} \tag{63}$$

This provides a method to compare the Coulomb and viscous dissipative sources. The equivalent damping coefficients are found, yet the best way to determine the damping is by an experimental test.

Experimental Test

To properly quantify the mechanical system damping the following experiment is performed. The wire-wound bearing (without end magnets) is mounted on the center rod and two mechanical springs are used replacing the stationary magnets, as in Figure 42. The transfer function is experimentally found for this mechanical system (X/Y) and the equivalent damping ratio can be estimated by a curve fit. This equivalent damping coefficient will then cover all mechanical damping mechanisms. The experimental results are covered in Chapter 7. The electromagnetic damping from the eddy current will be examined next.

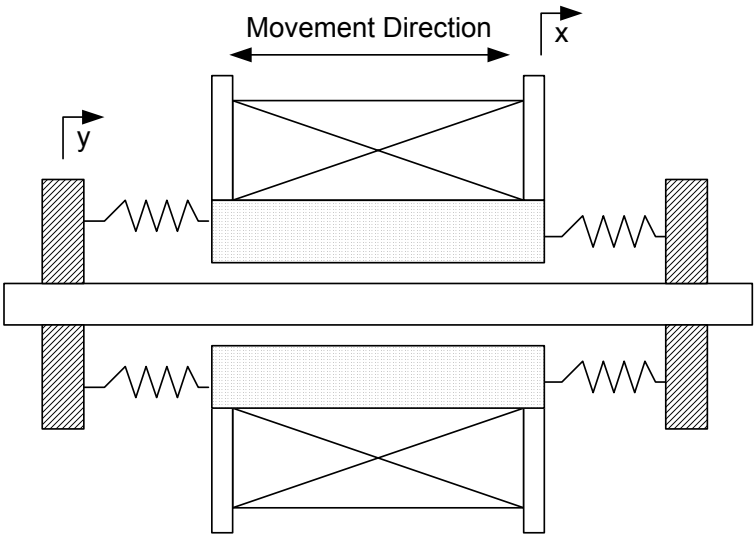

Figure 42: Mechanical Spring System Configuration

Electromagnetic Damping

In 1992, Yamashita and Seto developed a damper using variable magnetic damping.[17] Kobayashi and Aida also implement magnetic damping in a Houde damper.[16] These configuration used a conductive material moving through an electromagnetic field created from permanent magnets to provide a dissipative mechanism. Unlike these researchers this work does not look to maximize the electromagnetic damping, but only quantify it for its effect on the absorber. A fundamental review of electromagnetic damping follows.

Once the research absorber is implemented, time-varying magnetic fields will be present and this requires that Faraday's Law be reviewed.[53] In the nineteenth century, Faraday had found that a time varying magnetic field result in a closed circuit current. The B-field created by this induced current will oppose any change in the external field. Maxwell's equations demonstrate that the electric field created is related to the changing magnetic field as

$$\oint E_l dl = -\int\int \frac{dB_n}{dt} dS \tag{64}$$

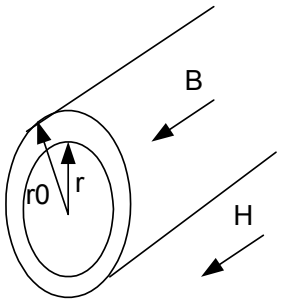

Figure 43: Construction for Eddy Currents in a Cylinder

For a cylinder as in Figure 43 with uniformly distributed parameters

$$2\pi r E(r) = -\pi r^2 \frac{dB}{dt};\ E(r) = -\frac{r}{2}\frac{dB}{dt} \tag{65}$$

The induced current in the cylinder is

$$I(r) = \frac{E(r)}{\rho} = -\frac{r}{2\rho}\frac{dB}{dt} \tag{66}$$

The current induced is frequently called an eddy current. The instantaneous power loss per unit length for a cylinder is

$$P = \frac{1}{\pi R^2}\int_0^R (-\frac{r}{2}\frac{dB}{dt})(-\frac{r}{2\rho}\frac{dB}{dt})2\pi r dr = \frac{R^2\mu^2}{8\rho}\left(\frac{dH}{dt}\right)^2 \tag{67}$$

With the field excited harmonically, Craik reports the average power becomes[53]

$$\overline{P} = \frac{\pi^2 R^2 \mu^2 f^2 H_0^2}{4\rho} \tag{68}$$

The work per unit length over one cycle when H is harmonic is

$$W = \int_0^{1/f} \frac{R^2\mu^2}{8\rho}\left(\frac{dH}{dt}\right)^2 dt = \frac{\pi^2 R^2 \mu^2 H_0^2 f}{4\rho} \tag{69}$$

Equating the work dissipated per cycle the equivalent damping measure can be obtained

$$c_{eq} = \frac{W_d}{2\pi^2 f X^2} = \frac{R^2\mu^2 H_0^2 L}{8\rho X^2} \tag{70}$$

Thus an equivalent viscous damping measure may be used for electromagnetic damping when a field varies harmonically through a cylinder.

In this work, if the center rod is examined for it conductive nature; H has a better approximation than a simple harmonic term. By taking an approximation of H at the center of a single loop used with the rod moving harmonically, an integral equation can be formed. The field along the axis of a single coil is

$$H_z = \frac{a^2 I}{2}[z^2 + a^2]^{-\frac{3}{2}} \tag{71}$$

Its spatial derivative may be calculated as

$$\frac{dH_z}{dz} = \frac{-3a^2 I}{2} z[z^2 + a^2]^{-\frac{5}{2}} \tag{72}$$

By using the chain rule the time derivative can be found

$$\frac{dH_z}{dt} = \frac{dH_z}{dz}\frac{dz}{dt} = \frac{-3a^2 I}{2} z[z^2 + a^2]^{-\frac{5}{2}} \frac{dz}{dt} \tag{73}$$

By calculating the work on a sliver of the rod

$$W = \frac{9R^2\mu^2 a^4 I^2}{32\rho}\int_0^T \left(\frac{\frac{dz}{dt} z}{(z^2 + a^2)^{5/2}} \right)^2 dt \tag{74}$$

The work across the entire length would be

$$W = \frac{9R^2\mu^2 a^4 I^2}{32\rho}\int_{-L/2}^{L/2}\int_0^T \left(\frac{\frac{dz}{dt} z}{(z^2 + a^2)^{5/2}} \right)^2 dtdl \tag{75}$$

This provides an analytical expression for the dissipated work per cycle for a center rod with field variation presented in Equation (71). The damping mechanism will be checked during the system experimental testing using experimental damping measures. An equivalent viscous damping term may then be calculated and used in the system simulation.

Experimental Test

To examine the electromagnetic damping influences a low damping cantilever beam is used as a reference. At the beam end a magnet is mounted. This system is depicted in Figure 44. The time response of this system is then found, this represents the inherent mechanical damping of the beam. Then two magnets are placed above and below the beam magnet. This systems response will have both the mechanical and electromagnetic damping components present. This enables an estimate of the electromagnetic damping contribution. The experiments are reported in Chapter 7.

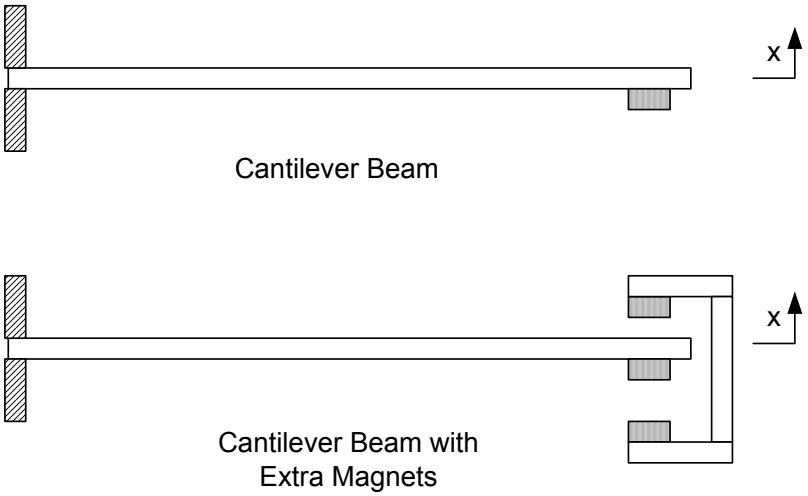

Figure 44: Beam System Diagram for Damping Determination

Damping Summary

This chapter has examined the fundamental damping mechanisms present and how they can be quantified. The most significant contribution is the experimental design to isolate and identify the damping mechanisms. This will provide insight of the electromagnetic and mechanical damping mechanisms contributions. The damping experiments are summarized in Chapter 7.

The damping relations are important to the tuned vibration absorber for maximum attenuation. The more damping the absorber system has, the less attenuation possible as found in Chapter 2. The best

can is the absorber to have no damping and then maximum cancellation is possible. If moderate damping is present the level of cancellation is reduced, yet the attenuation frequency range is enlarged.

CHAPTER 6. SYSTEM SIMULATION

The prior two chapters have examined the spring and damping forces present in the electromagnetic absorber. This chapter examines the absorber dynamic response that results from the force and damping relations. Now that these force relations are known the absorber system is simulated using ordinary differential equations. First a linear absorber is simulated, followed by the nonlinear absorber system.

Linear System Simulation

The general equation of motion is for a single degree of freedom system comes from Newton's Law as

$$\Sigma F = m\ddot{x} = f_{damp} + f_{spring} + f_{ext} \tag{76}$$

First, the response of the linear system with base excitation will be considered. This system is depicted in Figure 45.

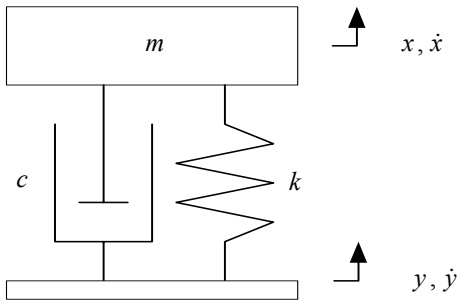

Figure 45: One Degree of Freedom with base motion

The equation of motion for applied base motion is

$$\Sigma F = m\ddot{x} = -c(\dot{x} - \dot{y}) - k(x - y) \tag{77}$$

By rearranging and algebra one arrives at

$$m\ddot{x} + c\dot{x} + kx = c\dot{y} + ky \tag{78}$$

By examining this equation in the frequency domain one determines the transfer function between X and Y as

$$\frac{X}{Y} = \frac{cs + k}{ms^2 + cs + k} \tag{79}$$

By substituting $s = +i\omega$ and rearranging with non-dimensional parameters.

$$\frac{X}{Y} = \frac{1 + 2\zeta\left(\frac{\omega}{\omega_n}\right)i}{\left(1 - \left(\frac{\omega}{\omega_n}\right)^2\right) + 2\zeta\left(\frac{\omega}{\omega_n}\right)i} \tag{80}$$

This function is presented in Figure 46 and this linear transfer function can be used as a reference for the nonlinear system response.

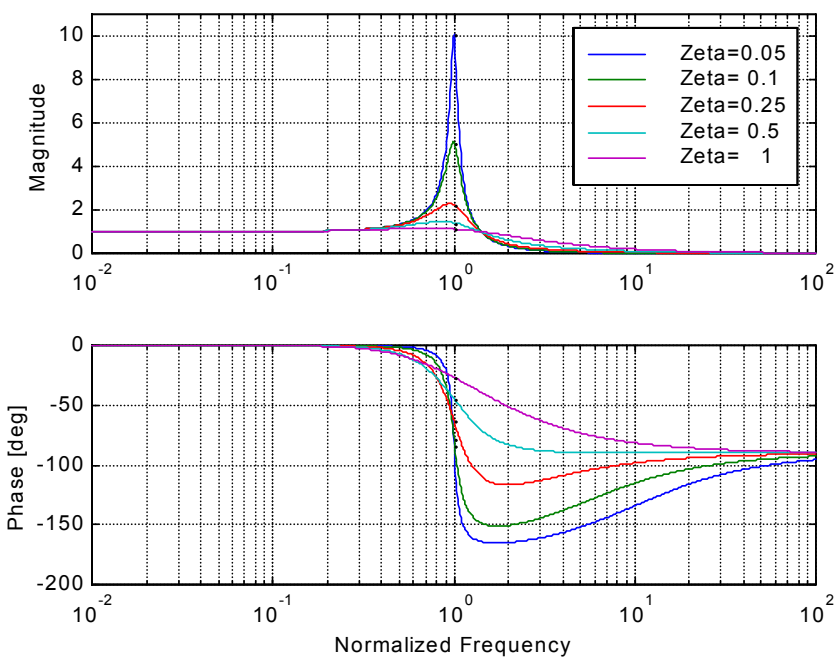

Figure 46: X/Y Transfer Function for Base motion

Alternatively, the system may be simulated using the applicable differential equations, with a selected mass (0.218 kg), moderate damping (c = 3.0 Ns/m), and the linearized stiffness coefficient (3800 N/m). A harmonic base excitation drives the system. Each frequency is simulated and the response analyzed after the transient terms decay. This allows isolation of the first order response and prevents having harmonic frequency multiples effecting the transfer function. Figure 47 shows the

outcome of a sine dwell simulation using a linear spring model for the absorber. The points are the simulated responses from the differential equation, the line is the appropriate curve fit for the SDOF linear transfer function. The curve fit identifies the natural frequency as 21.1 Hz with 5.5% of critical damping. The curve fit is close to the actual natural frequency of 21.0 Hz and 5.2% damping. In the linear case the higher order harmonics are not present.

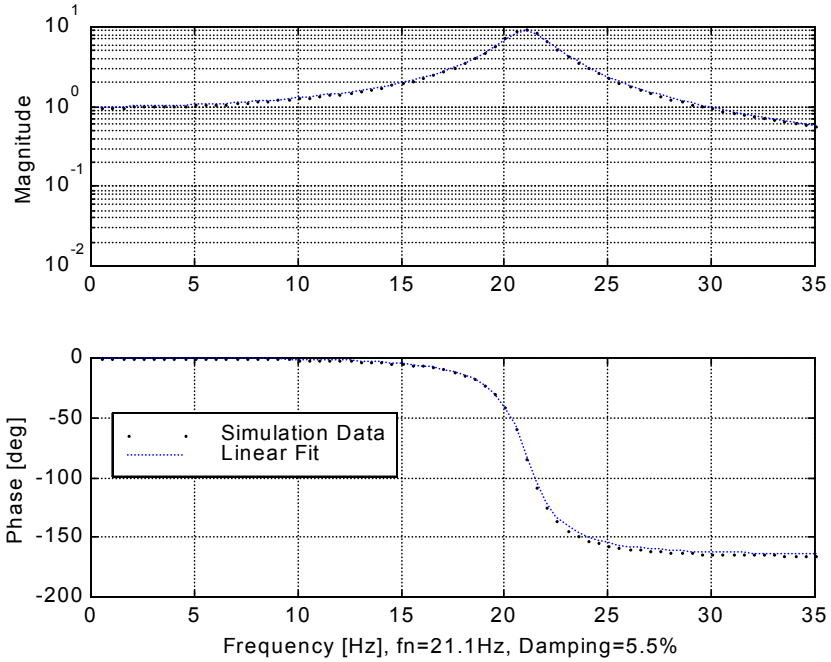

Figure 47: X/Y Linear System Transfer Function Simulation
[m=0.218 kg, c=3.0 Ns/m, k=3800 N/m]

Nonlinear System Simulation

The nonlinear absorber system, pictured in Figure 48, is now examined. The parameters used for the nonlinear simulation are discussed. The simulated mass is 0.129 kg. The damping term is taken as an equivalent viscous damping term. The spring force is selected based on the curve fits from the prior chapter, using the dual-sided inverse square relationship. The simulations were accomplished using sinusoidal base excitation to determine the motion of the absorber mass. The terms used in the simulation are

$$f_{damp}(\dot{z}) = c\dot{z}$$
$$f_{spring}(z) = \beta_{-2}(-(x_0 + z)^{-2} + (x_0 - z)^{-2}) \tag{81}$$

The resulting differential equation is

$$m\ddot{z} + f_{damp}(\dot{z}) + f_{spring}(z) = Y\omega^2 e^{-i\omega t} \tag{82}$$

This system may then be simulated with various base displacements, and spring forces based on changing currents and changing magnetic gap spacing. First the variable base excitation cases will be examined to demonstrate the system nonlinearity.

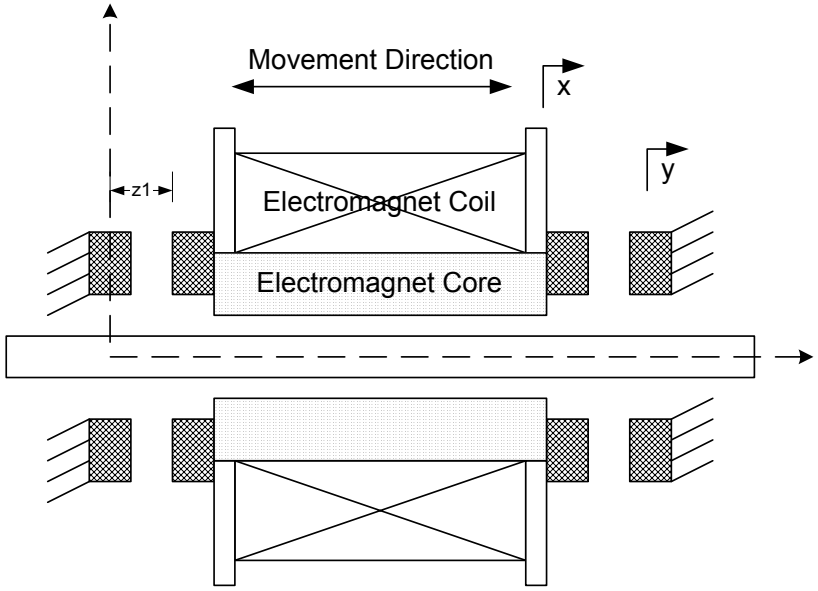

Figure 48: Absorber Configuration for Simulation

Variable Base Excitation

The first simulation will be with the outer magnets set to their closest position due to the physical constraints in the experimental apparatus. This sets the gap on each side of the absorber neutral position to 5.3 mm ($x_0 = 10.3\,\text{mm}$), and the electromagnet curve fit solves for $\beta_{-2} = 1.018\times10^{-3}\,\text{Nm}^2$ (see Table 3). The damping is set to c=1.0 Ns/m, and the base motion excitation amplitude is varied. These simulations are run without a current input.

The following graphs (Figure 49-Figure 52) depict the system's natural frequency shift with larger displacements caused by larger base excitation. The larger base displacement the higher the system's linear equivalent natural frequency becomes. This is due to the nonlinear nature of the spring force;

the electromagnetic absorber spring force actually stiffens with larger displacements as a Duffing spring does (Figure 37). The third graph in the figures displays the motion range so it is known that the range is not exceeded, which would be an invalid simulation, yet can numerically appear based on the simulation step size. In the larger base displacement cases the simulation shows a discontinuity in the transfer functions. This is expected due to the nonlinear spring; a Duffing spring has a similar response. It is due to a jump phenomenon in the transfer function that the differential equation has two amplitude solutions at some points.[54] Moderate to high damping will prevent the jump phenomenon from showing up.

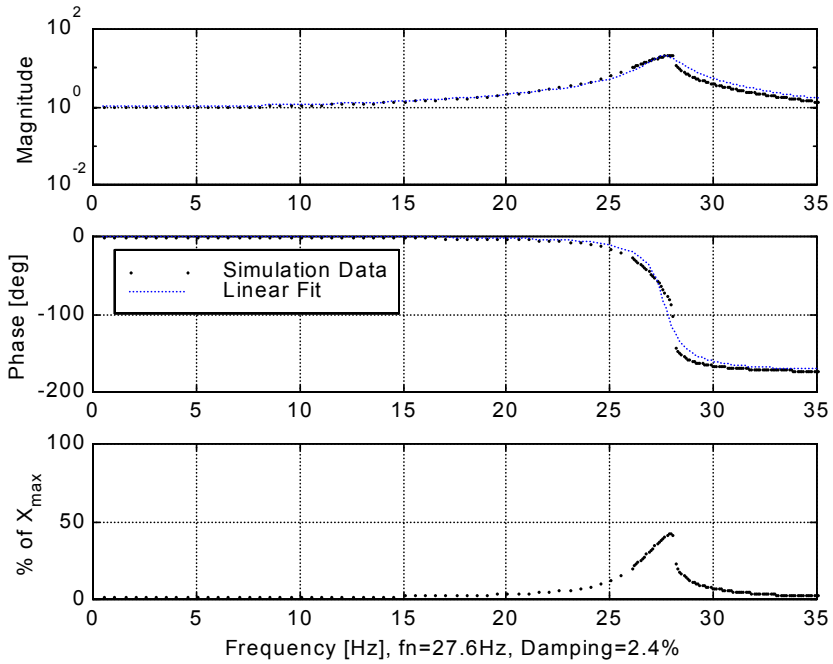

Figure 49: First order TF for non-linear system
[x_0 = 10.3mm, Base Displacement = 0.1mm]

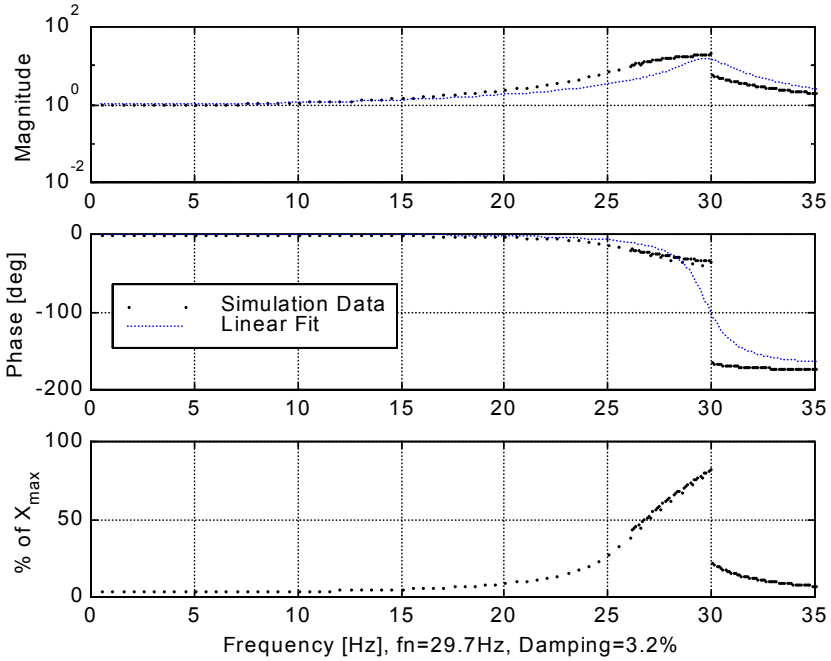

Figure 50: First order TF for non-linear system
[x_0 = 10.3mm, Base Displacement = 0.2mm]

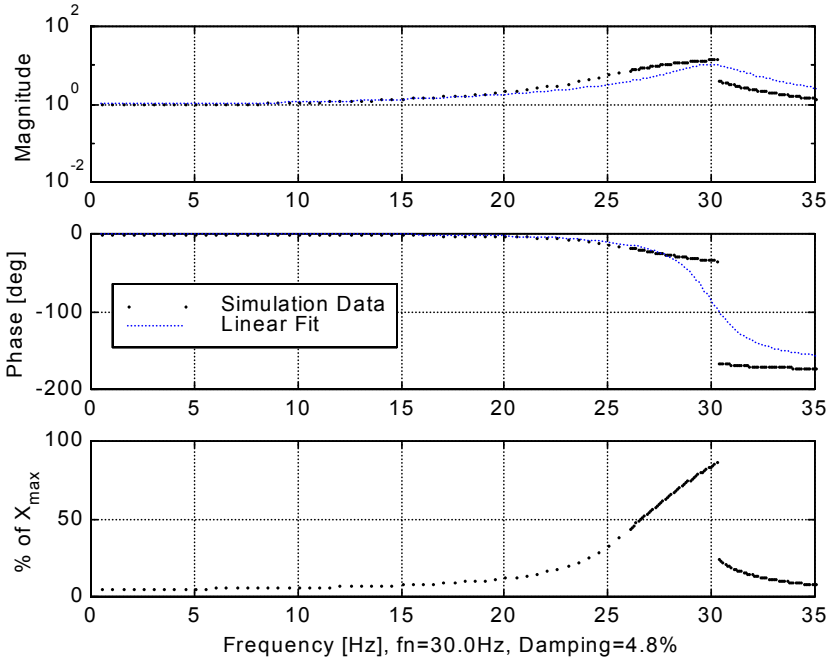

Figure 51: First order TF for non-linear system
[x_0 = 10.3mm, Base Displacement = 0.3mm]

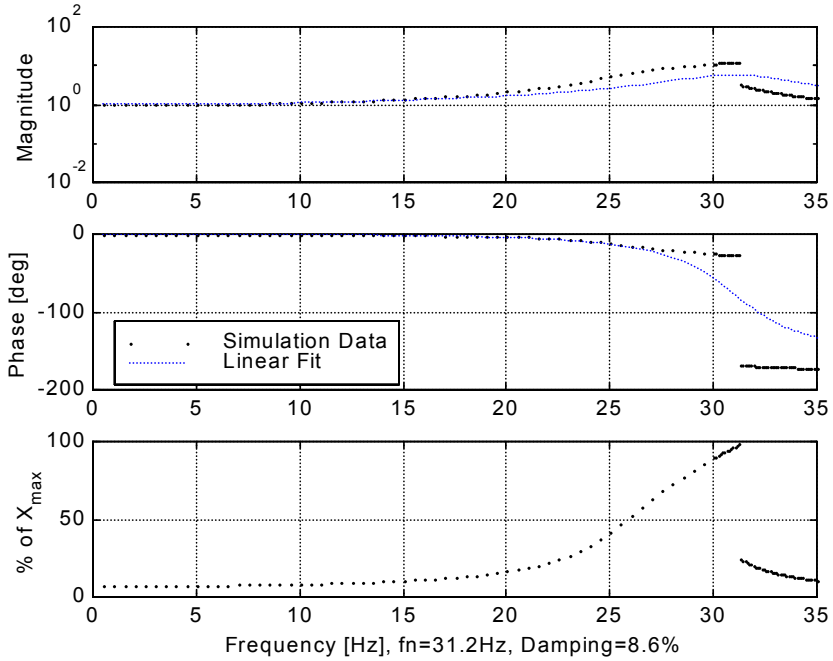

Figure 52: First order TF for non-linear system
[x_0 = 10.3mm, Base Displacement = 0.4mm]

Figure 52 shows the magnitude, phase & percent of displacement for the magnetic absorber without any current. Observing the graph the peak response is at 31.2 Hz. This figure represents only the linear transfer function response. Table 6 organizes the equivalent linear system parameters based on the varying base excitation. This demonstrates the increased linear natural frequency based on the increased base excitation.

Table 6: Theoretical Variation of Parameters Based on Base Excitation

Base Displacement (mm)	Curve Fit Natural Frequency (Hz)	Curve Fit Damping Ratio (%)	Peak Frequency (Hz)
0.1	27.6	2.4	28.0
0.2	29.7	3.2	29.9
0.25	29.4	4.2	29.6
0.3	30.0	4.8	30.2
0.35	30.5	5.4	30.7
0.4	31.2	8.6	31.2

Variable Current

By applying a current to the absorber the natural frequency will shift based on the effective stiffness change. The control advantage with current is that this excitation may be rapidly varied so that quick

changes in the transfer function will result. Figure 52 is the no current baseline for this set of simulations. Figure 53 shows the system response with a –10 Amp current supplied. The peak response shift of 1.3 Hz to 29.9 Hz is seen. Figure 54 demonstrates the system with a +10 Amp current. As expected the peak response frequency has shifted higher to 32.5 Hz. Figure 55 and Figure 56 show the linear frequency response for the –1 Amp and +1 Amp case respectively.

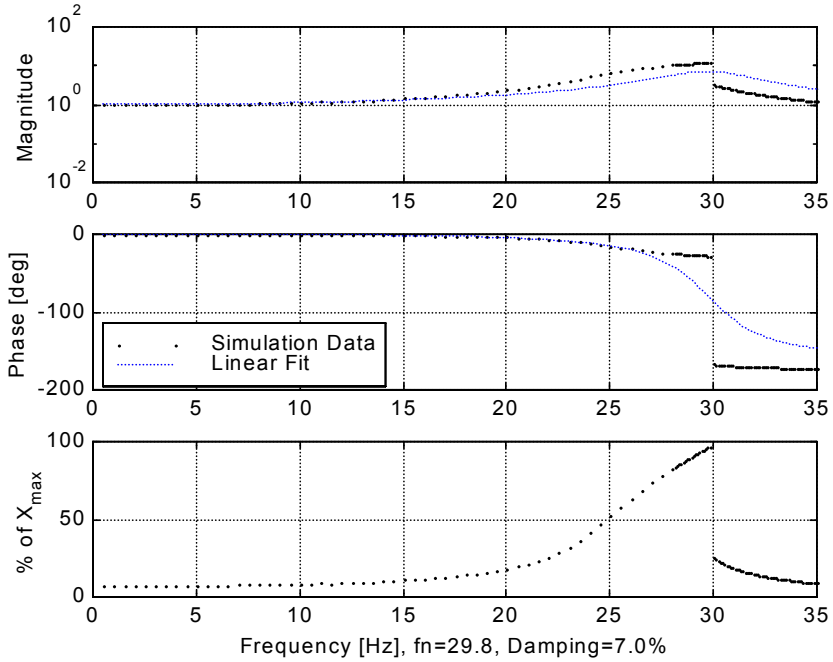

Figure 53: First order TF for non-linear system
[x_0 = 10.3mm, Base Displacement = 0.4mm, Current=-10A]

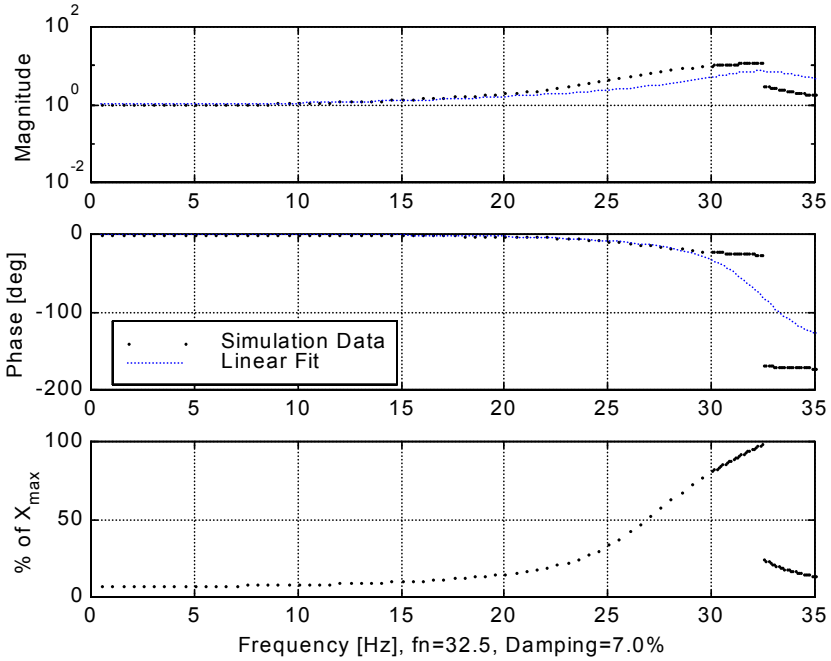

Figure 54: First order TF for non-linear system
[x_0 = 10.3mm, Base Displacement = 0.4m, Current=+10A]

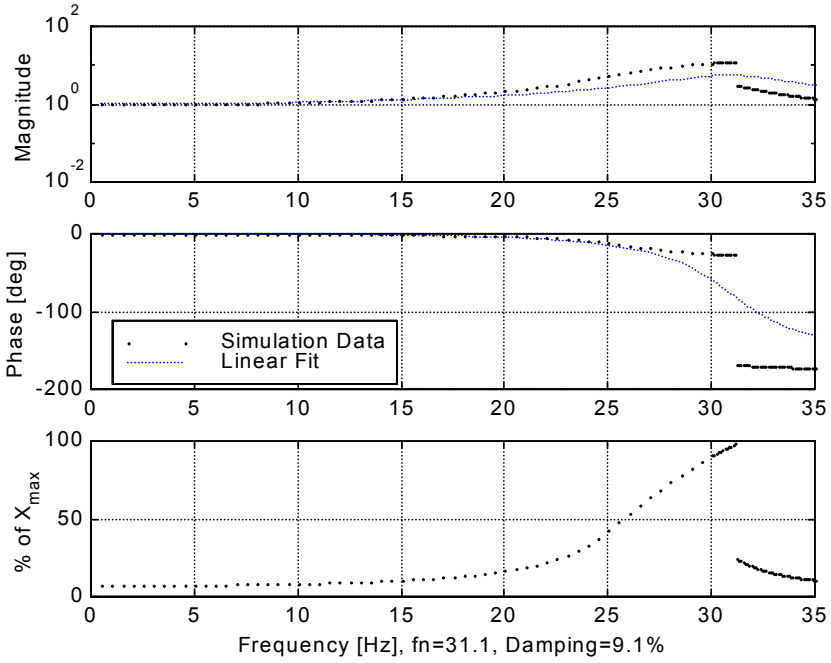

Figure 55: First order TF for non-linear system
[x_0 = 10.3mm, Base Displacement = 0.4mm, Current=-1A]

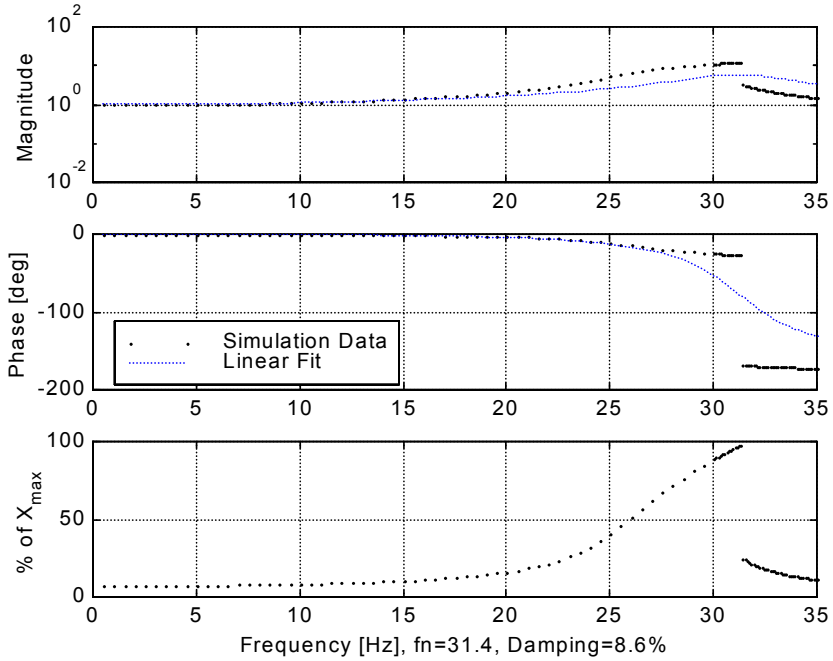

Figure 56: First order TF for non-linear system
[x_0=10.3mm, Base Displacement=0.4mm, Current=+1A]

The transfer function parameters are tabulated in Table 7. This demonstrates the current levels necessary to adjust the natural frequency. The power supplied for this current will be small since the coil resistant will be low and primarily inductive. These current levels are possible, yet the challenge is that the current continues to consume power for as long as it is supplied. In this case the equivalent natural frequency may be altered by 4% with a 10 amp input.

Alternatively the gap spacing can be manipulated that would not require continuous energy expenditure. These simulations follow.

Table 7: Theoretical Variation of Parameters Based on Input Current

Current (Amps)	Curve Fit Natural Frequency (Hz)	Curve Fit Damping Ratio (%)	Peak Frequency (Hz)
-10	29.9	7.0	29.9
-5	31.1	8.9	31.1
-1	31.1	9.1	31.1
0	31.2	8.9	31.2
+1	31.3	8.5	31.3
+5	31.9	7.5	31.8
+10	32.5	6.9	32.5

Variable Gap

By altering the distance between the stationary magnets the effective stiffness can also be altered. The system responses for various gaps are depicted in Figure 58 - Figure 67. x_0 is the z1 measurement that places the absorber in equilibrium. The movement gap on each side will be x_0 minus half the stationary magnets thickness. These figures show that by doubling the x_0 the natural frequency can be reduced by 60%. At the smallest x_0 of 10.3 mm the natural frequency is 31.2 Hz and the largest x_0 shown is 19.9 mm with a natural frequency of 10.2 Hz.

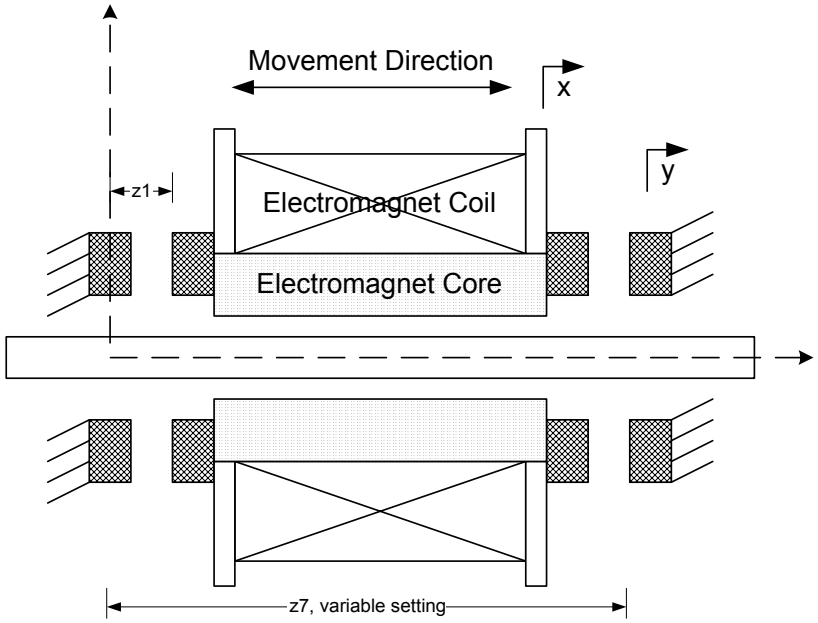

Figure 57: Gap Variation for Simulation

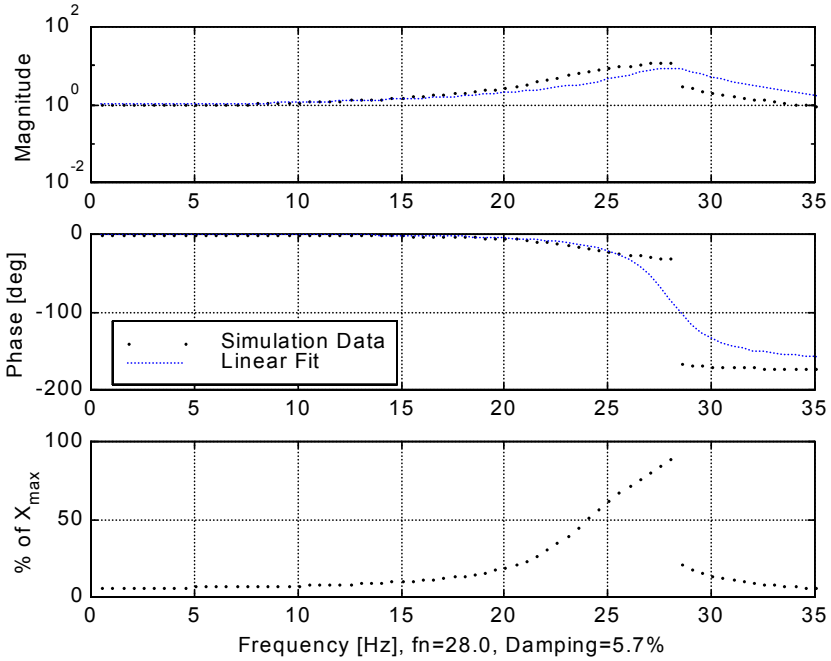

Figure 58: First order TF for non-linear system
[x_0 = 11 mm, Base Displacement = 0.4mm]

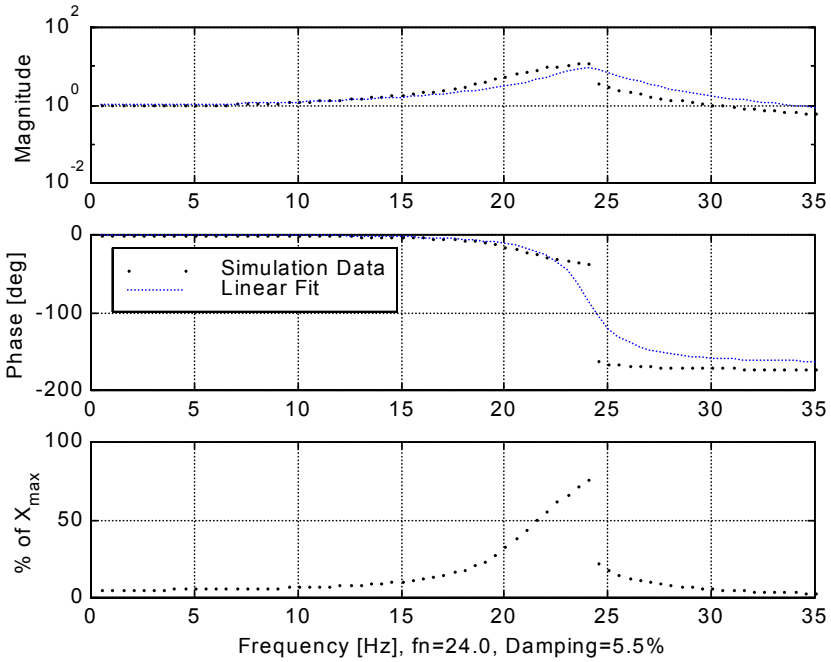

Figure 59: First order TF for non-linear system
[x_0 = 12 mm, Base Displacement = 0.4mm]

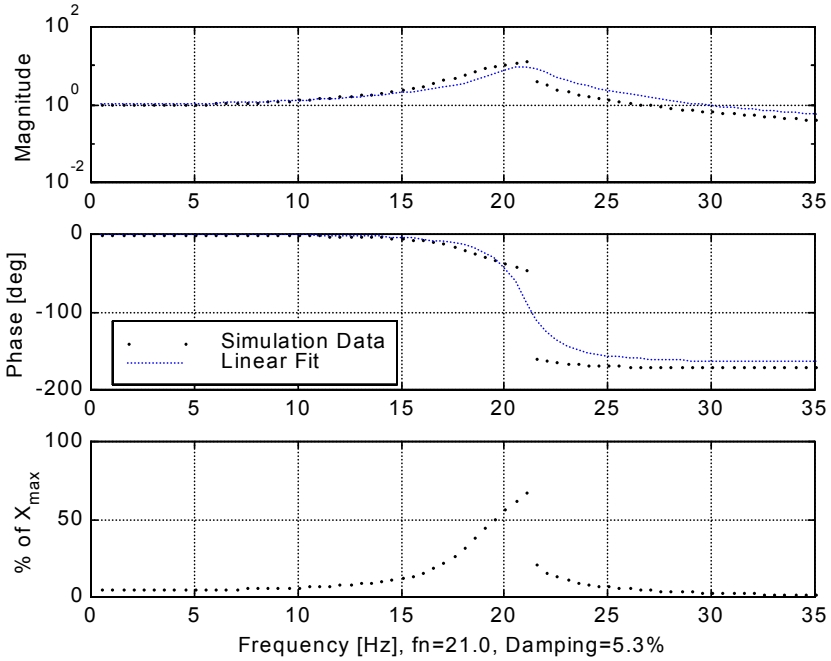

Figure 60: First order TF for non-linear system
[x_0 = 13 mm, Base Displacement = 0.4mm]

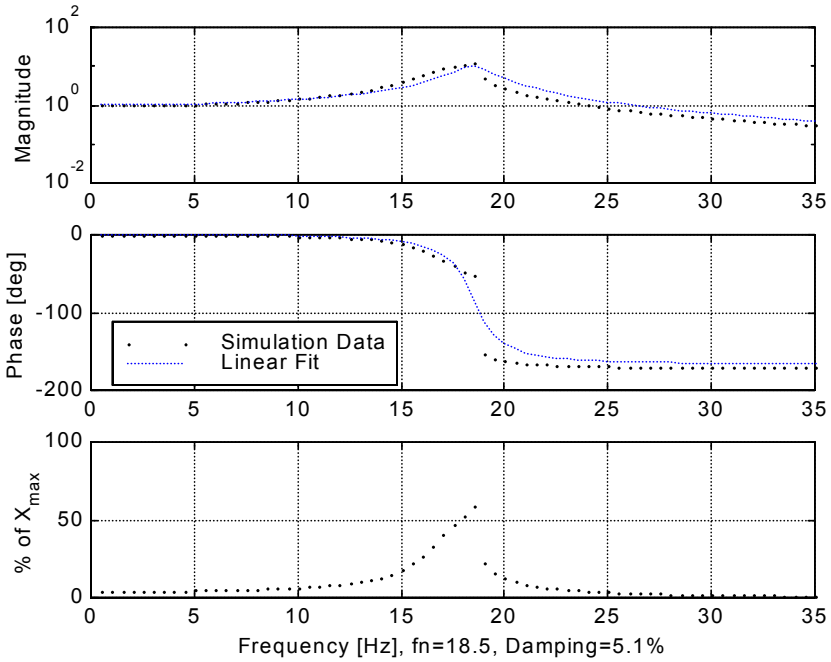

Figure 61: First order TF for non-linear system
[x_0 = 14 mm, Base Displacement = 0.4mm]

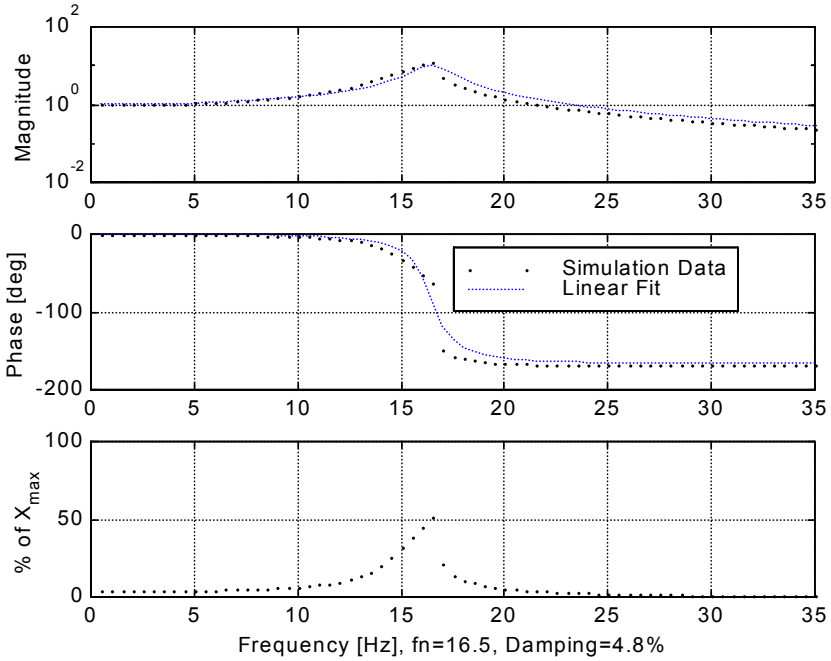

Figure 62: First order TF for non-linear system
[x_0 = 15 mm, Base Displacement = 0.4mm]

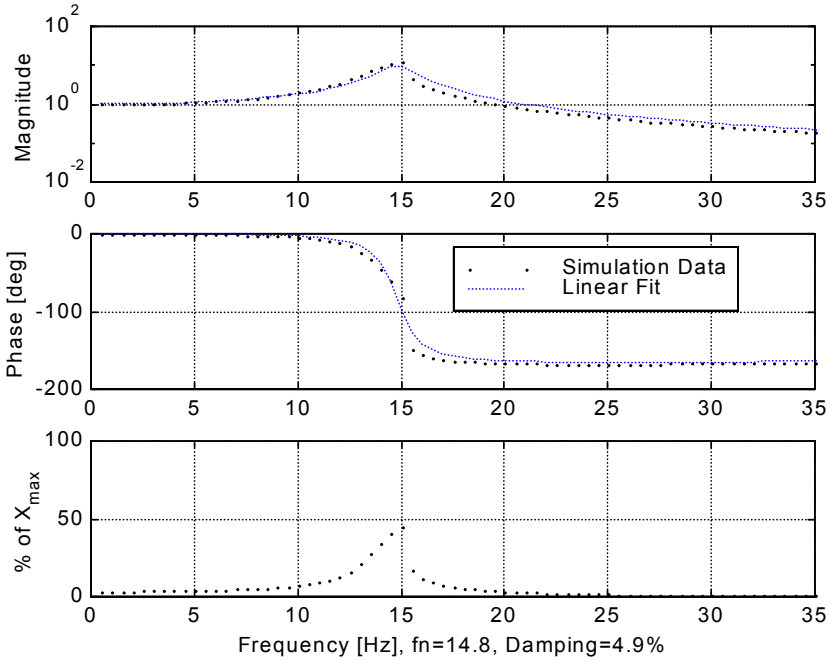

Figure 63: First order TF for non-linear system
[x_0 = 16 mm, Base Displacement = 0.4mm]

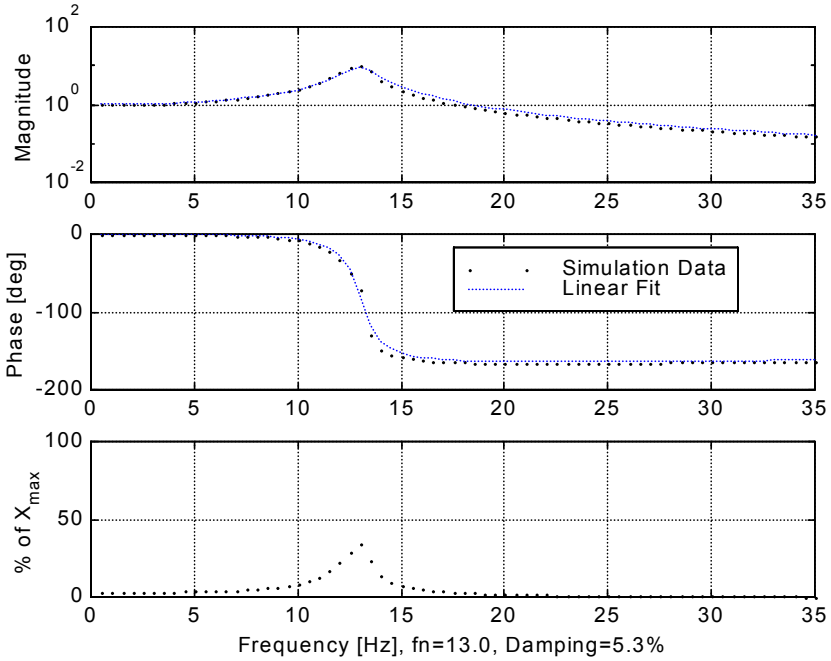

Figure 64: First order TF for non-linear system
[x_0 = 17.2mm, Base Displacement = 0.4mm]

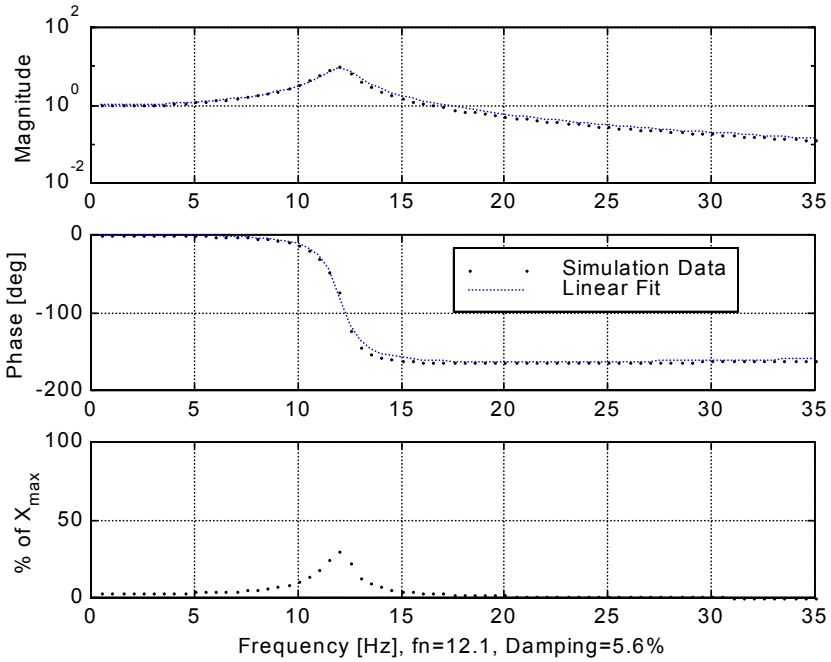

Figure 65: First order TF for non-linear system
[x_0 = 18 mm, Base Displacement = 0.4mm]

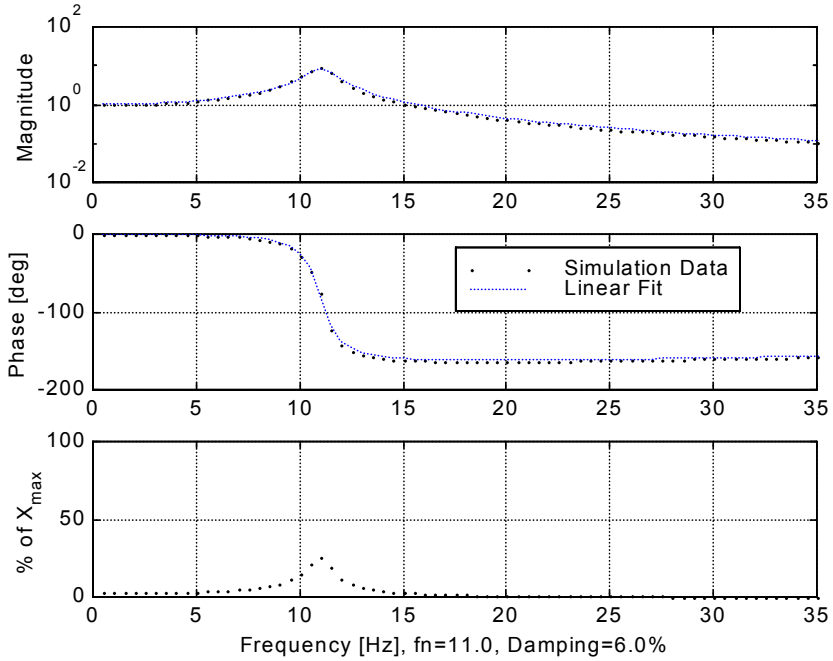

Figure 66: First order TF for non-linear system
[x_0 = 19 mm, Base Displacement = 0.4mm]

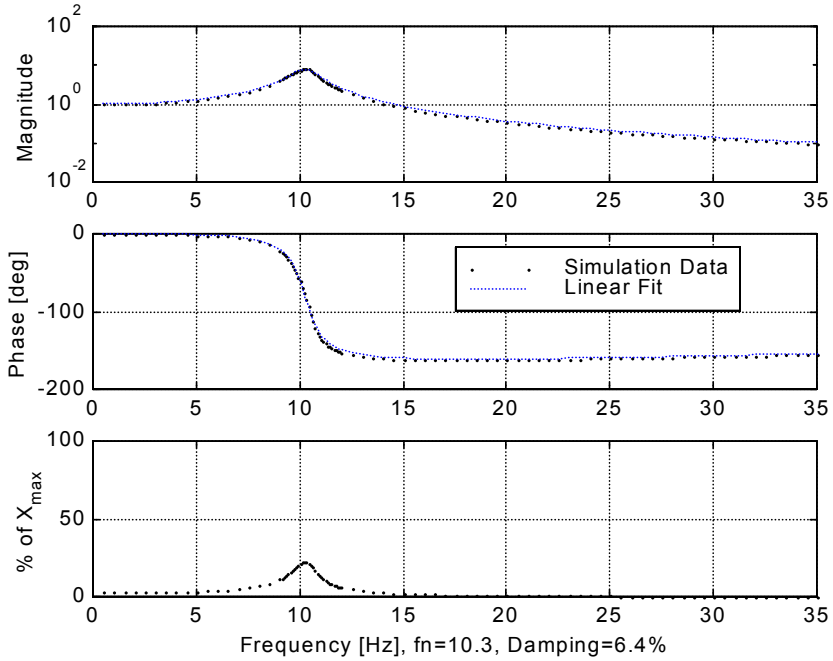

Figure 67: First order TF for non-linear system
[x_0 = 19.9mm, Base Displacement = 0.4mm]

Table 8 shows the parameter variation for various gap spacing. This table shows how the fit natural frequency and damping ratio shift with various gap settings. This table shows that the natural

frequency can be shifted across a large range based on the gap spacing. The advantage of this configuration is that once adjusted, maintaining the same natural frequency does not require additional energy input.

Table 8: Theoretical Variation of Parameters based on Gap Spacing

x_0 Spacing (mm)	Curve Fit Natural Frequency (Hz)	Curve Fit Damping Ratio (%)	Peak Frequency (Hz)
10.3	31.2	8.9	31.2
11	28.0	5.8	28.0
12	24.0	5.4	24.0
13	21.0	5.0	21.0
14	18.5	4.8	18.5
15	16.5	4.8	16.5
16	14.8	4.8	15.0
17.2	13.0	5.2	13.0
18	12.1	5.4	12.0
19	11.0	5.9	11.0
19.9	10.3	6.2	10.0

Higher Order Harmonics

Since the system is nonlinear, additional output frequencies may be generated. The primary, third, and fifth order harmonics are examined for their contribution. Figure 68 shows the nonlinear response to a pure tone excitation for the system. Figure 69 shows the primary, third, and fifth order response. The frequency axis represents is the input pure tone frequency, while the first order graph represents the first order output divided by the primary frequency phasor. The third order graph is the third order output phasor divided by the primary input frequency phasor.

Figure 69 - Figure 71 show that the contribution of the third and fifth order harmonics are small. The largest third order harmonics is 1.5% or the primary, while the fifth order is 0.07% or the primary.

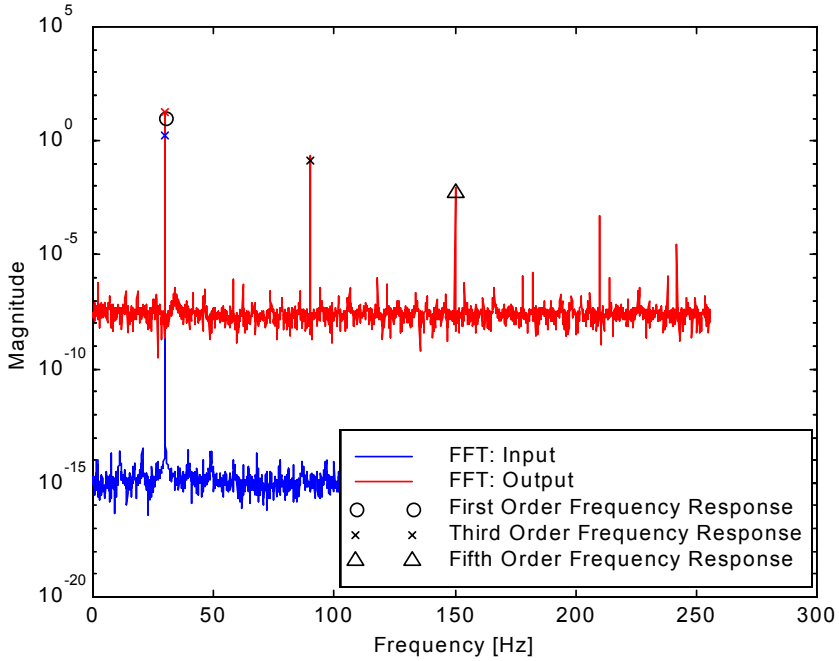

Figure 68: Pure Tone Excitation and Response for non-linear system
[x_0 = 10.3mm, Base Displacement = 0.4mm, Input Freq = 30 Hz]

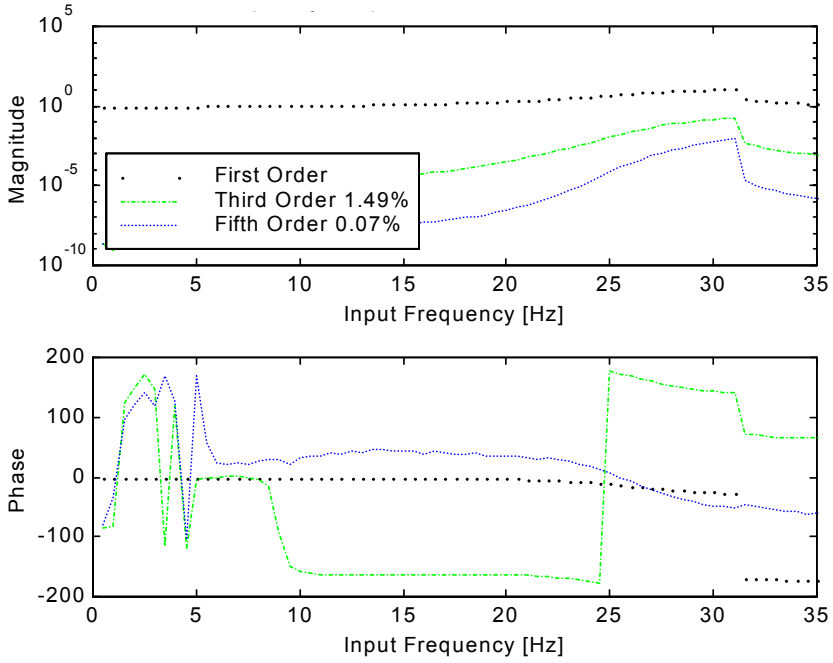

Figure 69: Harmonic TF for non-linear system
[x_0 = 10.3mm, Base Displacement = 0.4mm]

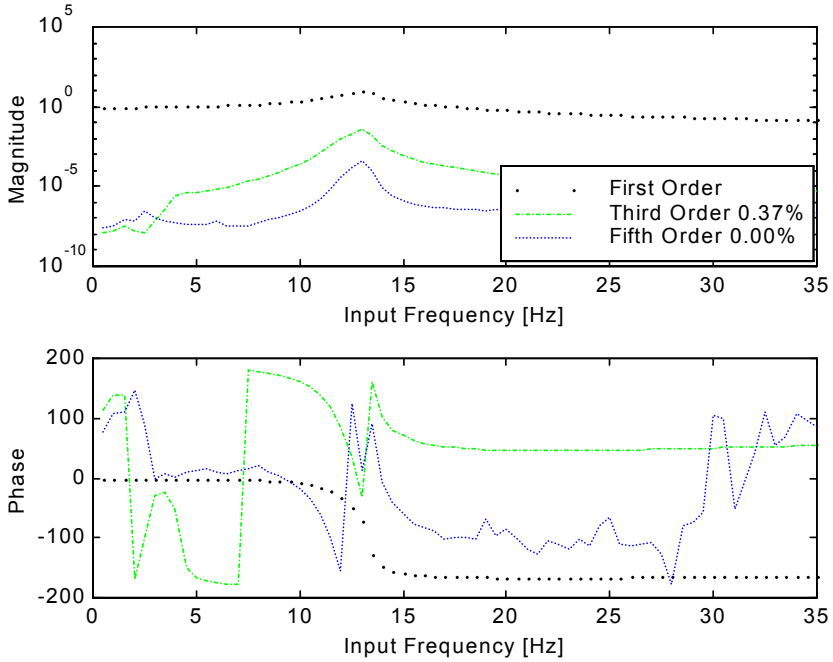

Figure 70: Harmonic TF for non-linear system
[x_0 = 17.2mm, Base Displacement = 0.4mm]

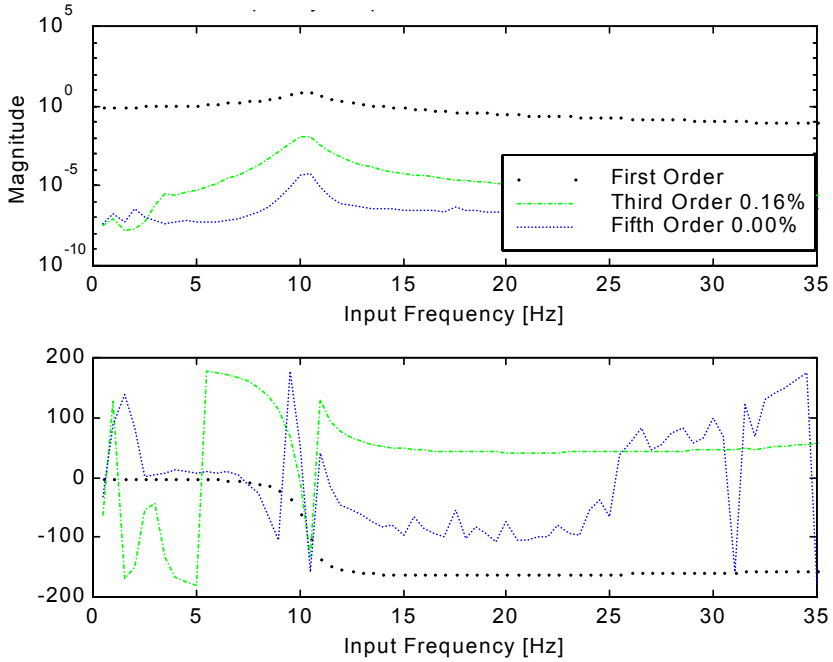

Figure 71: Harmonic TF for non-linear system
[x_0 = 19.9mm, Base Displacement = 0.4mm]

Simulation Summary

The chapter has undertaken the theoretical system simulations using the prior chapters force and damping results. A linear system is simulated as a check system. The first simulation group demonstrates how the increased base excitation level will stiffen the system as expected for the nonlinear spring. The second group shows that some variation of transfer function results in current variation. This small variation can be used in the absorber system to alter the combined system's response. The main factor of concern is that if the absorber damping is low the transfer function change will be more dramatic than if the absorber has a lot of damping.

The third group demonstrates that variation of the stationary permanent magnet positions can be implemented to vary the system transfer functions. The gap variation is appealing since the system may be altered and then no additional energy is necessary to retain the changed system.

This chapter has demonstrated the theoretical transfer function variation. This shows how the absorber system responds to the proposed system variation. The following chapter now examines the experimental setup and fundamental tests to understand the system.

CHAPTER 7. SYSTEM DESIGN AND INITIAL TESTING

This chapter describes the experimental apparatus and a group of introductory experiments. These experiments are designed to quantify and confirm our understanding of the force and damping relationships. The following chapter presents the dynamic tests of the complete absorber.

System Design

The experimental system consists of a non-magnetic rod on which the moving-mass is free to slide. This mass is supported with a Teflon™ bearing to minimize the friction present. On each end, a magnet can be positioned along the threaded portion to alter the spacing and the effective stiffness. The mechanical drawings are in Figure 72, and a system photograph in Figure 73.

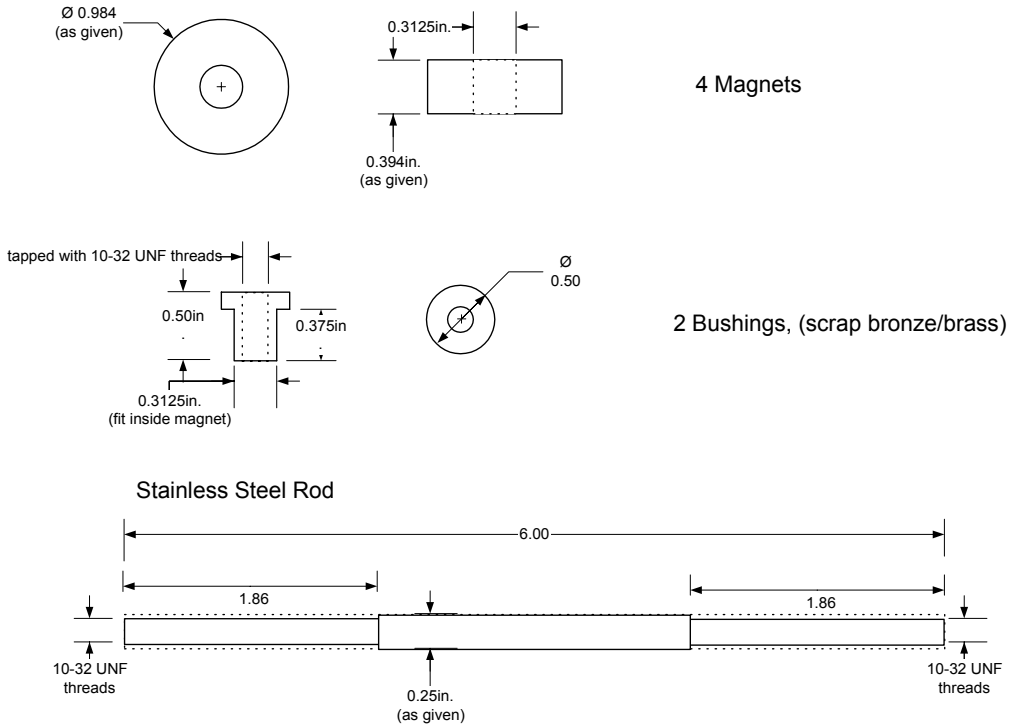

Figure 72: Mechanical Drawings

Figure 73: Apparatus Photograph

The moving-mass consists of a linear bearing encased between two washers and two magnets. The moving mass is 218.0 g and the shaft and end magnets have a mass of 89.0 g.

Force Relationship

The first experimental task undertaken determines the force to displacement relationship for the magnetic spring. This provides confirmation of the electromagnetic spring model developed in Chapter 4 and an estimate of the magnetic leakage. The leakage is a parameter based on the magnetic circuit efficiency; since the circuit is in repulsion the leakage will be close to one. The theoretical model will be selected with the leakage that results in the closest model to the experimental fit. This will provide the magnetic leakage estimate. The test assembles one fixed magnet on the rod and the movable center mass rests above the fixed magnet from the gravity force, depicted in Figure 74. The equivalent free body diagram is in Figure 75, by varying the mass the spring force verses displacement relationship can be found.

The guide rod and lower magnet are first placed on the scale and this weight can be tared out. Then the electromagnet can be added and the rest-position measured. Placing additional masses on top of the electromagnet allows additional force and gap data points to be determined. The measurement task is done with a nonmagnetic plastic/fiberglass caliper to determine the distance since any magnetic materials will alter the displacement measurement.

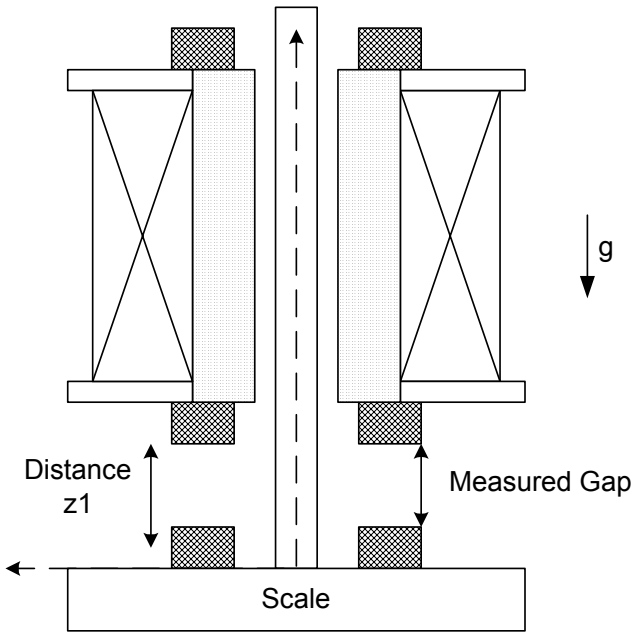

Figure 74: Force vs Displacement Experiment

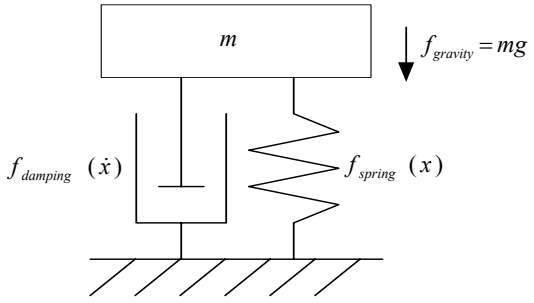

Figure 75: SDOF Force to Displacement Experiment Model

The gap reading is adjusted by the additional distance to the lower magnet center. This is the same reference position used in the theoretical development. The results are plotted in Figure 76. This graph also demonstrates a number of possible curve fit relationship. The inverse square experimental curve fit is in the form

$$F = B_{-2}(z_1)^{-2} \tag{83}$$

The polynomials are in the form

$$F = \sum_{i=0}^{n} B_i (z_1)^i \tag{84}$$

These polynomials have all terms up to and including the n^{th} power. The curve fits are calculated using the least squares methodology. The expected curve fit is an inverse square relationship as developed in Chapter 4. The polynomial fit is more illustrative in the dual-sided case. The best inverse square fit is

$$F = (1.221 \pm 0.048(mN)m^2)(z_1)^{-2} \tag{85}$$

Figure 77 shows the residual's standard deviation decreases as expected with increasing polynomial model order. Examining Figure 76, it is seen that the inverse square fit has the advantage that for extrapolations its behavior is as expected for the physical system. The polynomial curve fits exhibit divergence from expectation when used for extrapolations. The other advantage of the inverse square is that it only uses one coefficient while the polynomials use n+1 degrees of freedom. So even though the fifth order model has less residual standard deviation, it uses 5 more terms than the inverse square relation and the extrapolation is unacceptable. Therefore the most appropriate model is an inverse square model for the single-sided electromagnetic spring force.

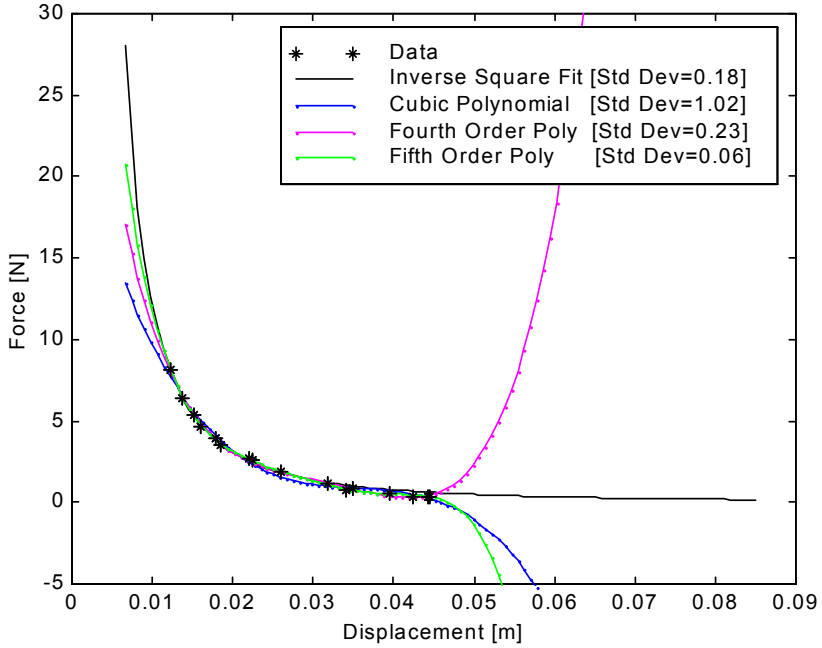

Figure 76: Experimental Data and Curve Fit Selections, no current

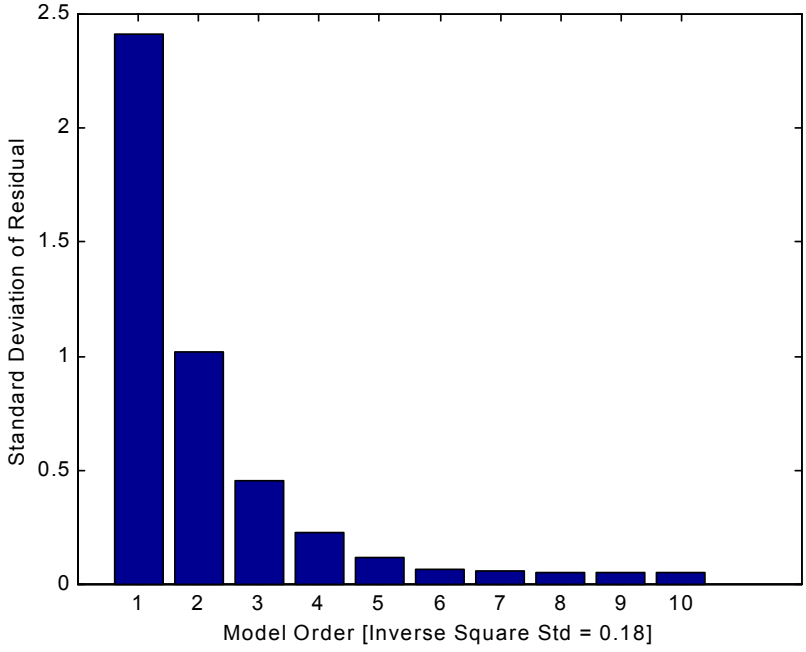

Figure 77: Curve Fit Residual Standard Deviations for Various Polynomials

The theoretical model is then examined in relation to the experimental model. The theoretical model values are calculated using the experimental parameters, and a range for the magnetic leakage. Each theoretic model is curve fit and the fit coefficient is compared with the experimental model. Examining Table 9 it is found that the most appropriate model has a magnetic leakage of 0.87. Figure 78 shows the graph of the experimental and best theoretical relationship.

Table 9: Variation in Theoretic Fit for Variable Leakage

Leakage	Theoretic Fit $[(mN)m^2]$	% Difference from Experimental Fit $[1.221 \pm 0.048\ (mN)m^2]$
0.80	0.989	-19
0.81	1.021	-16.4
0.82	1.053	-13.8
0.83	1.085	-11.2
0.84	1.117	-8.5
0.85	1.149	-5.9
0.86	1.181	-3.3
0.87	1.213 ± 0.024	-0.7
0.88	1.245	+1.9
0.89	1.276	+4.5
0.90	1.308	+7.1

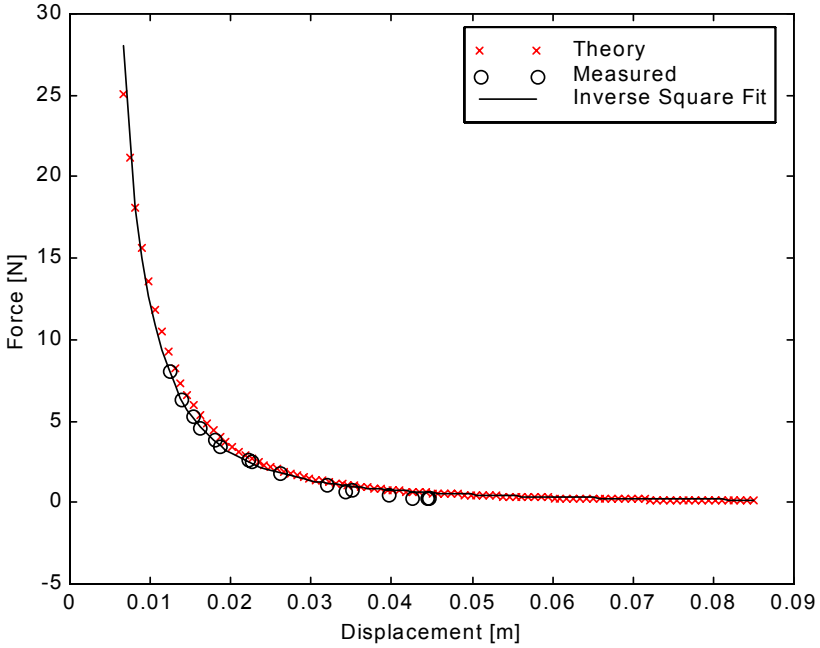

Figure 78: Experimental Force Relationship

Figure 79 plots the dual-sided magnetic spring force is as a result of the inverse square single-sided force. The equation is

$$F = B_{-2}(x_0 + x)^{-2} - B_{-2}(x_0 - x)^{-2} \tag{86}$$

x_0 is the distance from the fixed magnet center to the edge of the moving-mass neutral position; this will vary for different gaps. The curve fits attempted here are a linear, a cubic and linear term, and a fifth order, cubic and linear term. The odd order terms are selected since the function is odd function [f(x)=-f(-x)], the even order terms do not add descriptive power. The cubic and linear term is referred in literature as a Duffing spring. In this case, since the cubic term coefficient is positive, it represents a stiffening spring. Figure 79 shows that the dual-sided magnetic spring may be closely modeled as a Duffing spring. With this similarity we may be able to understand the response of the moving-mass in light of Duffing's work on non-linear systems. In a Duffing system the jump phenomenon is expected in the transfer function; although the high damping will make the jump frequency range small. These dynamic response characteristics will be discussed in more detail when examining the system's dynamic transfer functions.

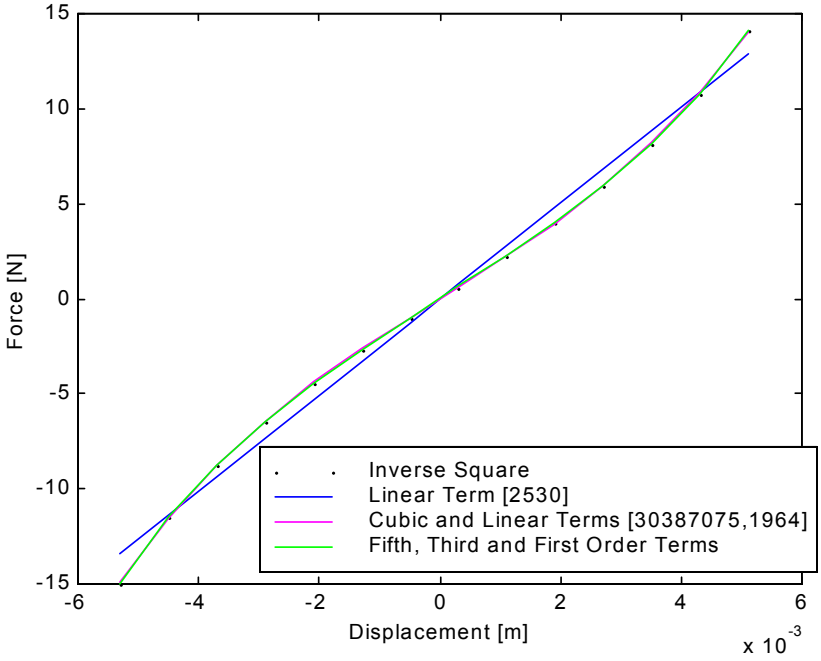

Figure 79: Dual-Sided Absorber and Curve Fit Selections

This first experiment has found the force to distance relation. The next step is to determine the equivalent damping relationship.

Damping Relationship

The absorber damping is very important for the system dynamics and the reduction of the combined system's vibration. Chapter 5 discussed that less absorber damping results in larger maximum attenuation at the anti-node. While more damping widens the attenuator band and reduces the maximum system attenuation. Two tests are undertaken to examine the moving-mass system damping. The tests are designed to allow the separation and identification of the mechanical damping and the electromagnetic damping mechanisms. The first test isolates the mechanical damping in the absorber system without electromagnetic forces. The second experiment separates the electromagnetic damping present in a low mechanical damping cantilevered beam system.

Damping Experiments for Mechanical Springs

To investigate the damping nature further, the response of the bearing and coil (without magnets, 159.5g) suspended with two mechanical springs is recorded. This enables the effects of the mechanical damping mechanism to be observed alone. This experimental setup is pictured in Figure 80.

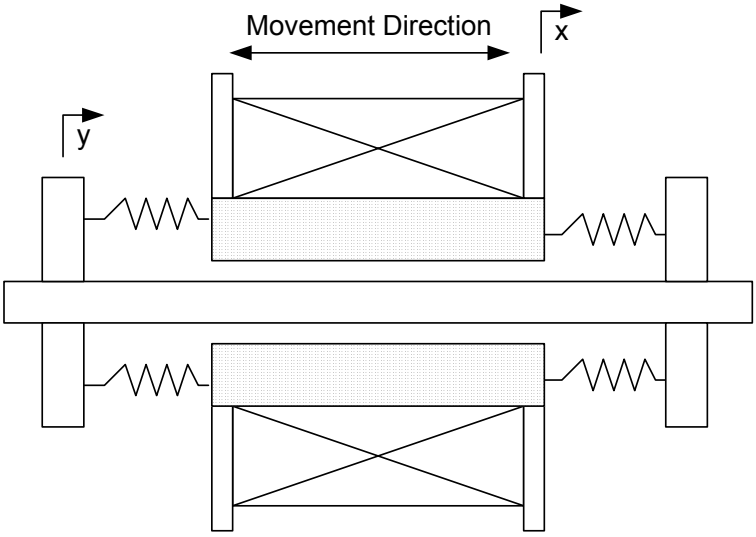

Figure 80: Mechanical Spring System Configuration

Figure 81 & Figure 82 are two transfer functions for the mechanical bearing system. The transfer functions relate the moving-mass acceleration to the base motion acceleration. This should not be confused with an operating shape since the driving force is the base motion. The transfer function curve fit minimizes the sum of the squared residuals magnitudes. The fit equation form is

$$\frac{X}{Y}=\frac{s^2X}{s^2Y}=\frac{\frac{c}{m}s+\frac{k}{m}}{s^2+\frac{c}{m}s+\frac{k}{m}}=\frac{\beta_1 s+\beta_0}{s^2+\beta_1 s+\beta} \tag{87}$$

This is a nonlinear estimation and the equation is evaluated across a grid of potential β_1 and β_0. Evaluating the residuals between each individual fit and the experimental data helps identifies the best fit with the minimum sum of residual magnitudes squared. Based on this single degree of freedom curve fit, the damping estimates are 5.0% and 6.4% in the two tests. In this system there are no electromagnetic fields present, therefore this damping represents the mechanical damping mechanism,

believe to primarily be Coulomb damping. This level of inherent mechanical damping is certainly a drawback in the absorber design.

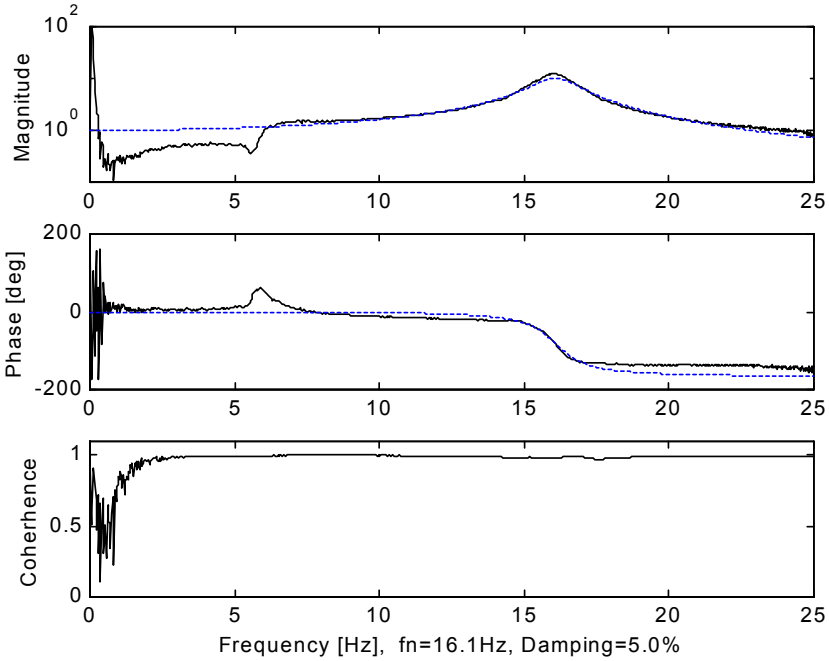

Figure 81: Transfer Function for Bearing with Mechanical Springs [1]

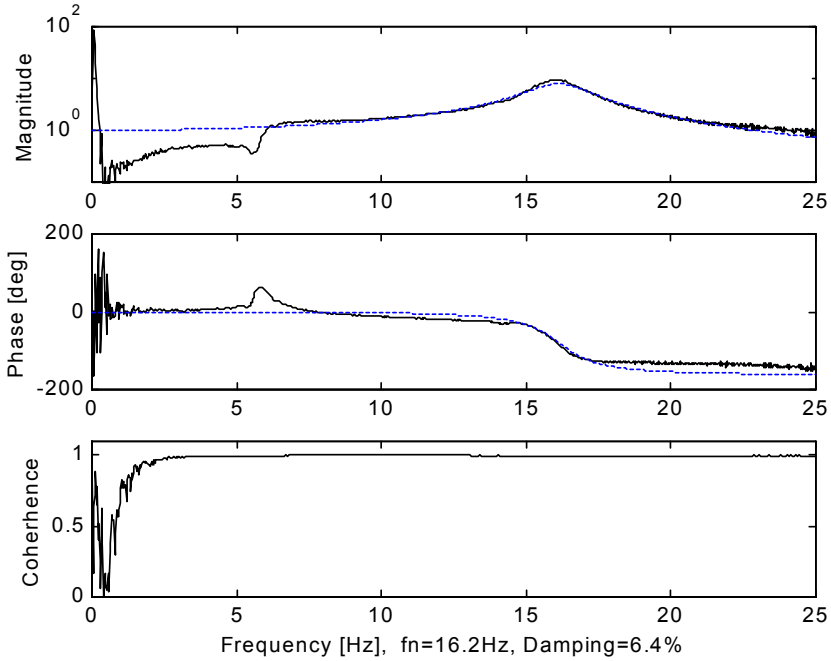

Figure 82: Transfer Function for Bearing with Mechanical Springs [2]

Damping Experiments for Beam with Magnets

This experiment isolates the damping present from electromagnetic mechanisms. This allows the electromagnetic damping to be quantified. A cantilever beam is clamped to a fixed base at one end and a single magnet attached to the far end. A cantilever beam is selected for its inherent low mechanical damping.

The beam's response is then recorded under two different cases. The first case examines the inherent damping in the cantilever beam. The beam acceleration is recorded after excitation of the first beaming mode. The second case places two fixed magnets in repulsion along the nominal movement axis of the cantilevered magnet. This increased the system stiffness due to the additional force added and may alter the damping characteristics. The system diagram is found in Figure 83.

The two responses are graphed in Figure 84. The black line on top represents the estimated decay envelope. This envelope is found by summing the Hilbert Transform and the original signal in the

time domain. The decay envelope follows the expected exponential decay pattern. This expected decay pattern for a linear spring and a viscous damper is

$$D = Xe^{-\zeta\omega_n t} \tag{88}$$

This can be examined in a transformed linear space as

$$\ln D = \ln X - \zeta\omega_n t \tag{89}$$

This equation can be used in a linear fit to estimate the damping ratio, given the damped natural frequency estimation from the impulse response.

The decay envelope is close to the expected exponential decay model. The linearized transformed signal is then plotted in Figure 85. The top graph is for the cantilever beam and the bottom graph includes the stiffening magnets. In this graph a linear equation is expected if the damping was purely viscous and the spring constant linear, the data appears close to linear. This indicates that this method is an appropriate method to estimate the damping. This data appears linear while the time signal has not experienced too much decay. In the lower diagram, it deviates from a linear fit since the signal-to-noise ratio becomes large. The curve fit is then calculated across the time range or 0.2 – 6.0 sec, the portion where the signal has not decayed completely.

The damping estimates for the cantilever alone are 1.4%. Using the magnets to stiffen the system, the total damping becomes 3.0%, and increase of 1.6% damping. This increase is attributable to the electromagnetic mechanisms of damping between permanent magnets.

This demonstrates that the electromagnetic field provides both an increased stiffness as well as increased damping. The electromagnetic damping dissipates energy through eddy current and electromagnetic warming, as discussed in Chapter 5.

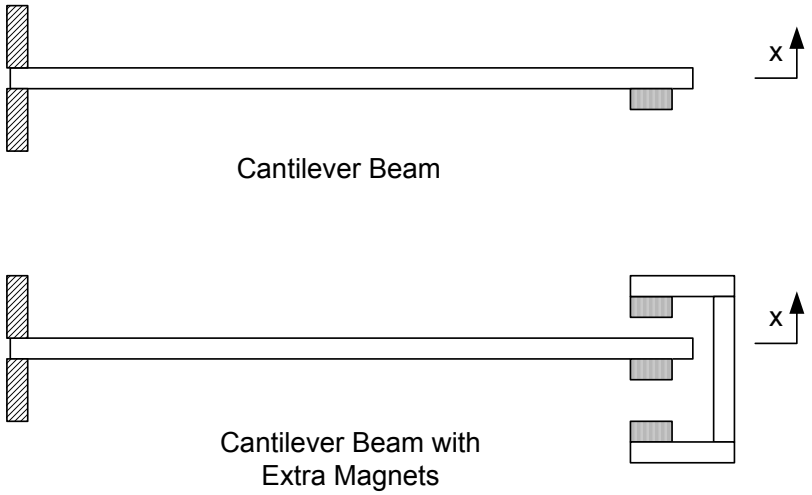

Figure 83: Beam System Diagram

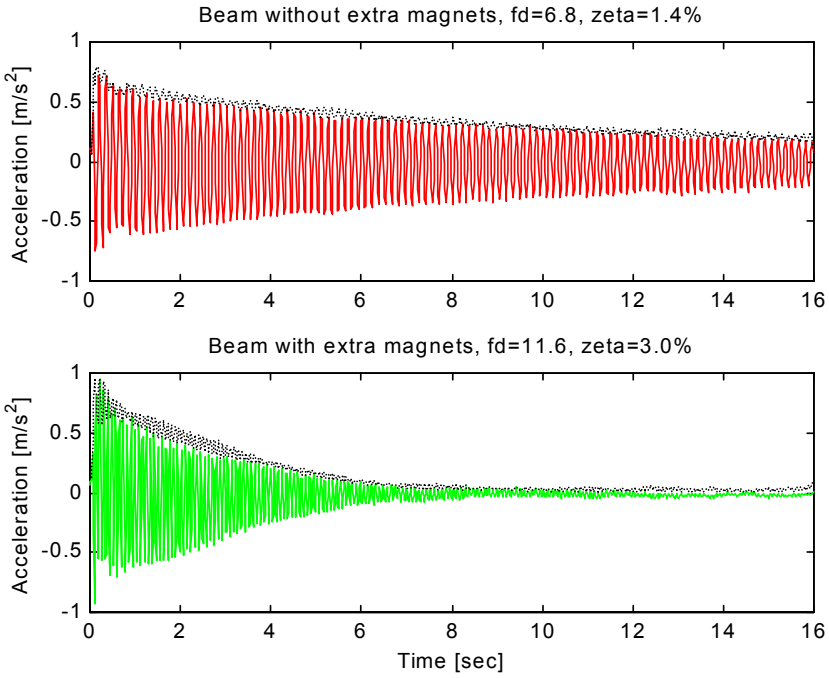

Figure 84: Time Response for Beam Systems

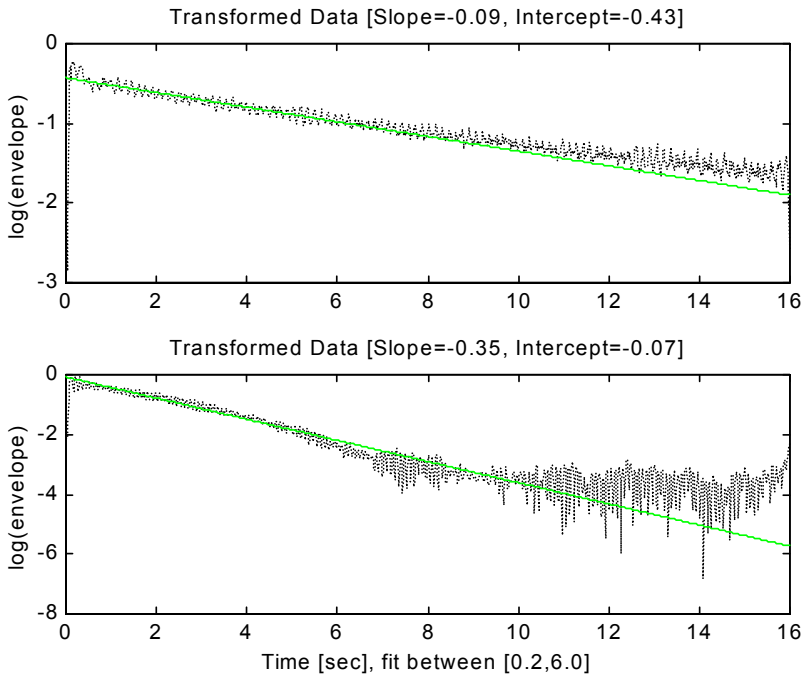

Figure 85: Transformed Data Curve Fit

Summary

This chapter presented initial experiments with the prototype absorber and other setups to characterize the absorber's spring and damping force. The single-sided force is characterized as an inverse square relationship as discussed in Chapter 4. The experimental curve fit values are evaluated from the data recorded. The magnetic leakage is evaluated based on the best fit of the data. The dual-sided absorber spring relation is similar to a Duffing stiffening spring.

It was found that the majority of the absorber damping is mechanical damping from the first damping test. The mechanical damping experienced is between 5-6.4% of critical. Additionally it is found that the magnets not only supply a spring-like restoring force, yet also have electromagnetic damping present. The electromagnetic damping present for just the magnets is on the order of 1.6% of critical damping.

The spring force and the damping force directly related to the absorber's performance and ability to cancel vibration. The spring force is confirmed to be an inverse square relation and the curve fit

coefficient evaluated. The damping is found to be significant in the current design, this may limit the cancellation ability of the current absorber design. The next chapter evaluates the experimental dynamic response for parameter variations. This will demonstrate the absorbers ability to vary its parameters when placed on a primary system.

CHAPTER 8. TVA DESIGN EQUATIONS AND TUNING

Design Equations for Minimum Response

The linear two degree of freedom system as in Figure 86 can be represented with the matrix of frequency response functions (FRFs), as follows:

$$\begin{Bmatrix} X_1 \\ X_2 \end{Bmatrix} = \begin{bmatrix} H_{11}(\omega) & H_{12}(\omega) \\ H_{21}(\omega) & H_{22}(\omega) \end{bmatrix} \begin{Bmatrix} F_1 \\ F_2 \end{Bmatrix} \tag{90}$$

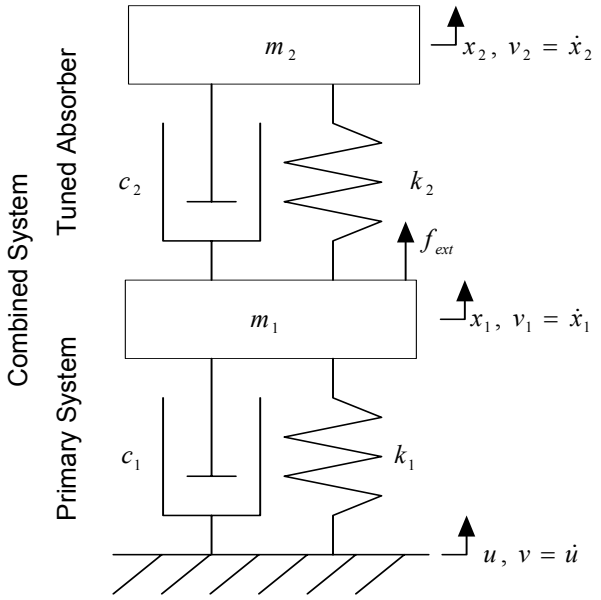

Figure 86: Combined System

In order to minimize the X_1 motion from the applied force F_1 at the frequency ω, $|H_{11}(\omega)|$ must be minimized with a properly tuned actuator. The minimum of $|H_{11}(\omega)|$ is investigated by examining the

minimum of the product with the complex conjugant $H_{11}(\omega)H_{11}^{*}(\omega)=\frac{\overline{N}(\omega)}{\overline{D}(\omega)}$. It's first derivative is evaluated ($Z(\omega)=\partial(HH^{*})/\partial\omega$) and roots are determined. The equation becomes

$$\begin{aligned} Z(\omega) &= \frac{\overline{D}(\omega)\overline{N}'(\omega)-\overline{N}(\omega)\overline{D}'(\omega)}{\overline{D}^{2}(\omega)} \\ &= Z_{11}\omega^{11}+Z_{9}\omega^{9}+Z_{7}\omega^{7}+Z_{5}\omega^{5}+Z_{3}\omega^{3}+Z_{1}\omega=0 \end{aligned} \tag{91}$$

By solving for the roots of $Z(\omega)$ one may determine the frequency at which the extrema points of $H(\omega)H^{*}(\omega)$ occur. The constituent equations $\overline{N}(\omega)$ and $\overline{D}(\omega)$ are expanded below. $Z(\omega)$ is expanded analytically with symbolic math program and the Matlab code is located in the Appendix.

$$\overline{N}(\omega)=\overline{N}_{0}+\omega^{2}\overline{N}_{2}+\omega^{4}\overline{N}_{4} \tag{92}$$

$$\overline{N}_{0}=(k_{2})^{2} \tag{93}$$

$$\overline{N}_{2}=-2m_{2}k_{2}+c_{2}^{2} \tag{94}$$

$$\overline{N}_{4}=m_{2}^{2} \tag{95}$$

$$\overline{D}(\omega)=\overline{D}_{0}+\omega^{2}\overline{D}_{2}+\omega^{4}\overline{D}_{4}+\omega^{6}\overline{D}_{6}+\omega^{8}\overline{D}_{8} \tag{96}$$

$$\overline{D}_{0}=\left(\mathrm{k}_{1}\mathrm{k}_{2}\right)^{2} \tag{97}$$

$$\begin{aligned} \overline{D}_{2} &= -2m_{1}k_{1}k_{2}^{2}-2m_{2}k_{1}^{2}k_{2}-4m_{2}k_{1}k_{2}k_{3} \\ &\quad +c_{1}^{2}k_{2}^{2}+c_{2}^{2}k_{1}^{2}+2c_{3}^{2}k_{1}k_{2}+2c_{1}c_{3}k_{2}^{2}+2c_{2}c_{3}k_{1}^{2} \end{aligned} \tag{98}$$

$$\begin{aligned} \overline{D}_{4} &= +m_{1}^{2}k_{2}^{2}+m_{2}^{2}k_{2}^{2}+m_{2}^{2}k_{1}^{2}+2m_{2}^{2}k_{1}k_{2}+4m_{1}m_{2}k_{1}k_{2}+2m_{1}m_{2}k_{2}^{2} \\ &\quad +c_{1}^{2}c_{2}^{2}-2m_{1}c_{2}^{2}k_{1}-2m_{2}c_{1}^{2}k_{2}-2m_{2}c_{2}^{2}k_{1} \end{aligned} \tag{99}$$

$$\begin{aligned} \overline{D}_{6} &= -2m_{1}^{2}m_{2}k_{2}-2m_{1}m_{2}^{2}k_{1}-2m_{1}m_{2}^{2}k_{2} \\ &\quad +m_{1}^{2}c_{2}^{2}+m_{2}^{2}c_{1}^{2}+m_{2}^{2}c_{2}^{2}+2m_{2}^{2}c_{1}c_{2}+2m_{1}m_{2}c_{2}^{2} \end{aligned} \tag{100}$$

$$\overline{D}_8 = m_1^2 m_2^2 \tag{101}$$

$Z(\omega)$ may be examined for variable k_2 with the other system parameters fixed. The masses, damping coefficient, and base stiffness taken for numeric confirmation are in Table 10. With these parameters the zeros of $Z(\omega)$ can be solved for and plotted for variable k_2. This methodology allows for direct evaluation of the extrema for the frequency response function.

Table 10: Numeric Parameter Confirmation Values

Variable	Value	Units
m_1	1	kg
m_2	0.1	kg
c_1	0.02	N/(m/s)
c_2	0.002	N/(m/s)
k_1	1	N/m
k_2	0.8- 1.2	N/m

Figure 87 and Figure 88 depicts the frequency response relationship for the single degree of freedom system and the extrema when a variable stiffness actuator is implemented.

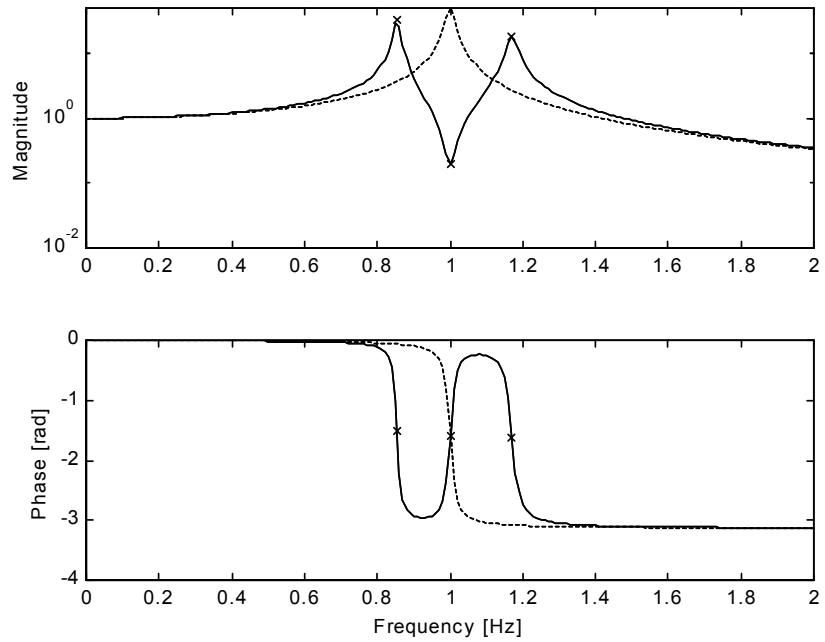

Figure 87: Frequency Response Function for SDOF and standard fixed TVA

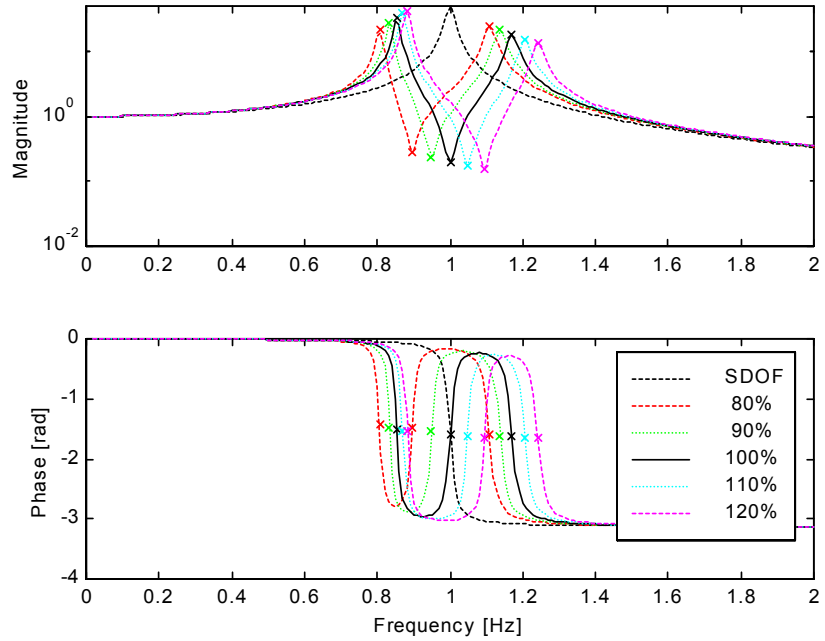

Figure 88: Frequency Response Functions for SDOF and TVA with varied stiffness ($m_1/m_2 = 10, \zeta_1 = \zeta_2 = 1\%$)

The positive real valued frequencies for these extrema points are tabulated in Table 11. This depicts that a 20% change in the stiffness results in close to a 10% change in the minimum response frequency, for a mass ratio of 10:1. These frequency response functions demonstrate that by appropriately altering the tuned vibration absorber stiffness the system response can be shifted lower than simply a passive vibration absorber. Figure 89 and Figure 90 depict the similar results for smaller absorber masses (40:1 and 100:1), these figures demonstrate that a 10% change in natural frequency is possible with a 20% change in stiffness. The frequency response function becomes more sensitive to the excitation frequency as the absorber mass is decreased and the minimum response is larger for a smaller absorber mass.

Table 11: Extrema Values for Magnitude Frequency Response Function

Stiffness Multiplier	Frequency	Magnitude	Phase	Extrema Type
[%]	[Hz]		[rad]	
0% - SDOF	*1.00*	*50.00*	*-1.57*	*Maximum*
80%	1.11	24.80	-1.60	Maximum
	0.90	**0.28**	**-1.47**	**Minimum**
	0.81	21.50	-1.43	Maximum
90%	1.14	21.21	-1.62	Maximum
	0.95	**0.23**	**-1.54**	**Minimum**
	0.83	28.02	-1.48	Maximum
95%	1.15	19.57	-1.62	Maximum
	0.97	**0.22**	**-1.56**	**Minimum**
	0.84	31.08	-1.50	Maximum
100%	1.17	18.06	-1.63	Maximum
	1.00	**0.20**	**-1.58**	**Minimum**
	0.85	33.90	-1.51	Maximum
105%	1.19	16.68	-1.64	Maximum
	1.02	**0.19**	**-1.60**	**Minimum**
	0.86	36.43	-1.52	Maximum
110%	1.21	15.43	-1.65	Maximum
	1.05	**0.17**	**-1.61**	**Minimum**
	0.87	38.67	-1.53	Maximum
120%	1.24	13.30	-1.66	Maximum
	1.10	**0.15**	**-1.64**	**Minimum**
	0.88	42.29	-1.54	Maximum

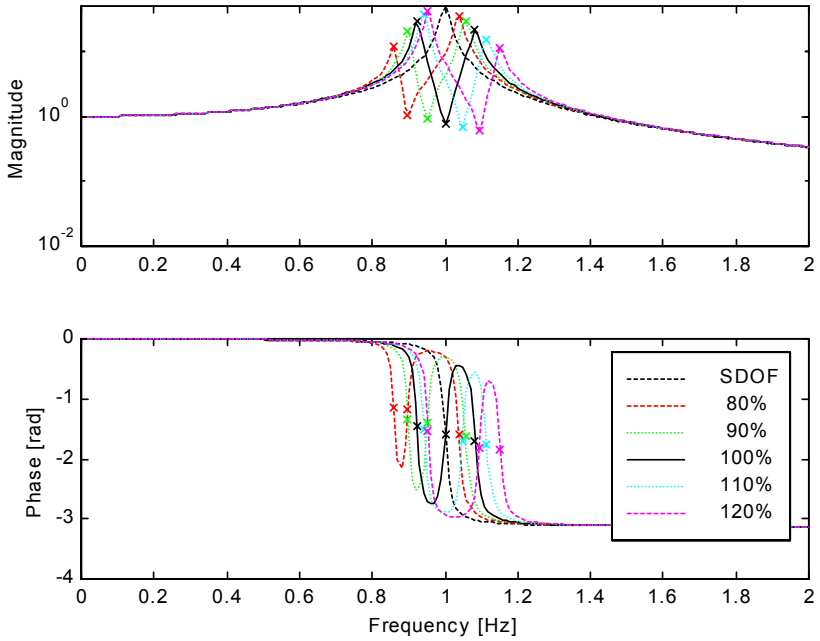

Figure 89: Frequency Response Functions for SDOF and TVA with varied stiffness ($m_1/m_2 = 40, \zeta_1 = \zeta_2 = 1\%$)

Table 12: Extrema Values for Magnitude Frequency Response Function ($m_1/m_2 = 40, \zeta_1 = \zeta_2 = 1\%$)

Stiffness Multiplier	Frequency	Magnitude	Phase	Extrema Type
[%]	[Hz]		[rad]	
0% - SDOF	*1.00*	*50.00*	*-1.57*	*Maximum*
80%	1.04	35.03	-1.59	Maximum
	0.90	**1.05**	**-1.19**	**Minimum**
	0.86	11.99	-1.15	Maximum
100%	1.08	21.45	-1.69	Maximum
	1.00	**0.79**	**-1.58**	**Minimum**
	0.92	29.41	-1.45	Maximum
120%	1.15	11.44	-1.84	Maximum
	1.09	**0.59**	**-1.81**	**Minimum**
	0.95	42.39	-1.53	Maximum

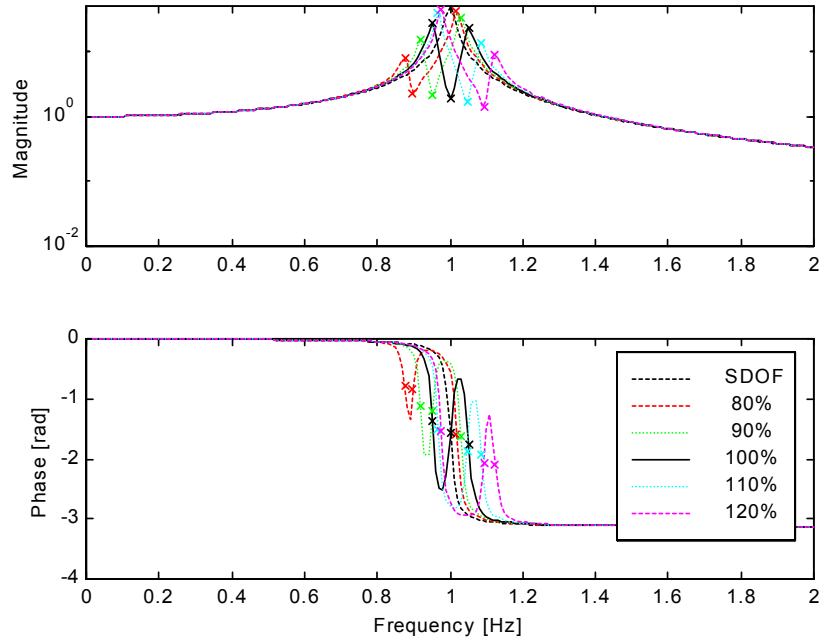

Figure 90: Frequency Response Functions for SDOF and TVA with varied stiffness $(m_1/m_2 = 100, \zeta_1 = \zeta_2 = 1\%)$

Table 13: Extrema Values for Magnitude Frequency Response Function $(m_1/m_2 = 100, \zeta_1 = \zeta_2 = 1\%)$

Stiffness Multiplier	Frequency	Magnitude	Phase	Extrema Type
[%]	[Hz]		[rad]	
0% - SDOF	*1.00*	*50.00*	*-1.57*	*Maximum*
80%	1.02	41.21	-1.58	Maximum
	0.90	**2.21**	**-0.83**	**Minimum**
	0.88	7.96	-0.79	Maximum
100%	1.05	23.02	-1.76	Maximum
	1.00	**1.92**	**-1.58**	**Minimum**
	0.95	28.12	-1.38	Maximum
120%	1.12	8.75	-2.10	Maximum
	1.09	**1.37**	**-2.07**	**Minimum**
	0.98	44.58	-1.54	Maximum

Figure 91 to Figure 93 depict the system frequency response for varied damping coefficients (c_2) of the absorber mass. Figure 91 shows that increased damping coefficient for c_2 causes reduced peaks and increased troughs. Figure 92 & Figure 93 demonstrate varied damping for altered stiffness

parameters. Figure 92 has the stiffness adjusted to 120% while the damping is varied, and Figure 93 has the stiffness set to 80% while the damping is varied.

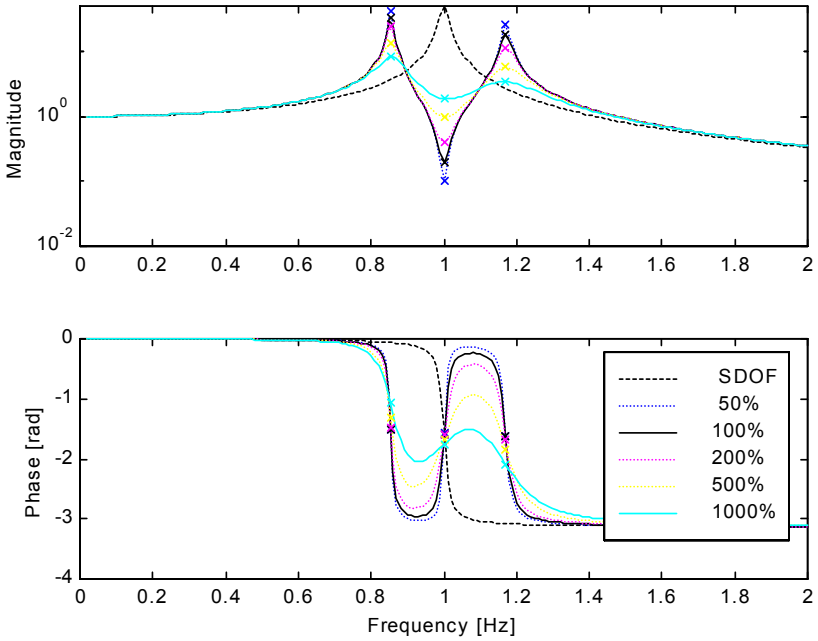

Figure 91: Frequency Response Functions for SDOF and TVA with varied damping ($m_1/m_2 = 10, \zeta_1 = 1\%$)

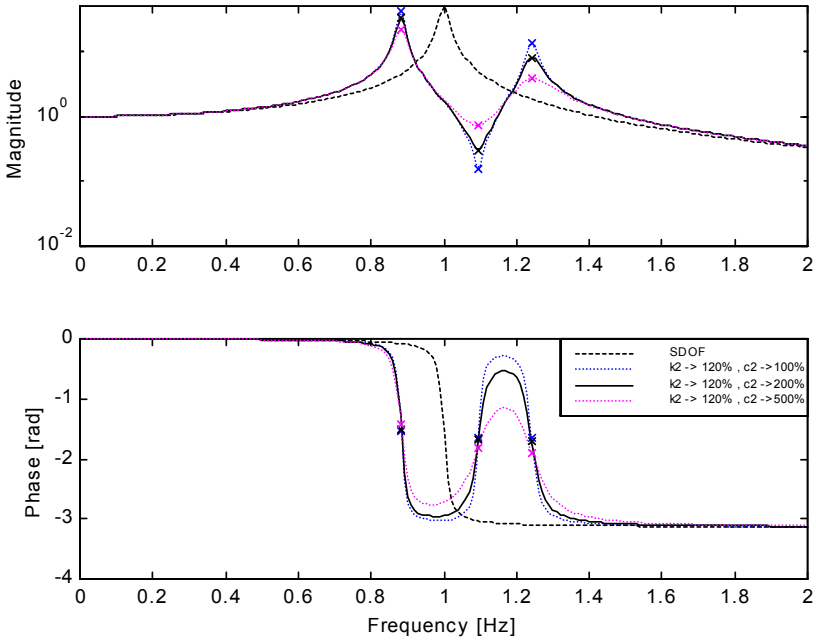

Figure 92: Frequency Response Functions for SDOF and TVA with varied stiffness & damping $(m_1/m_2 = 10, \zeta_1 = 1\%)$

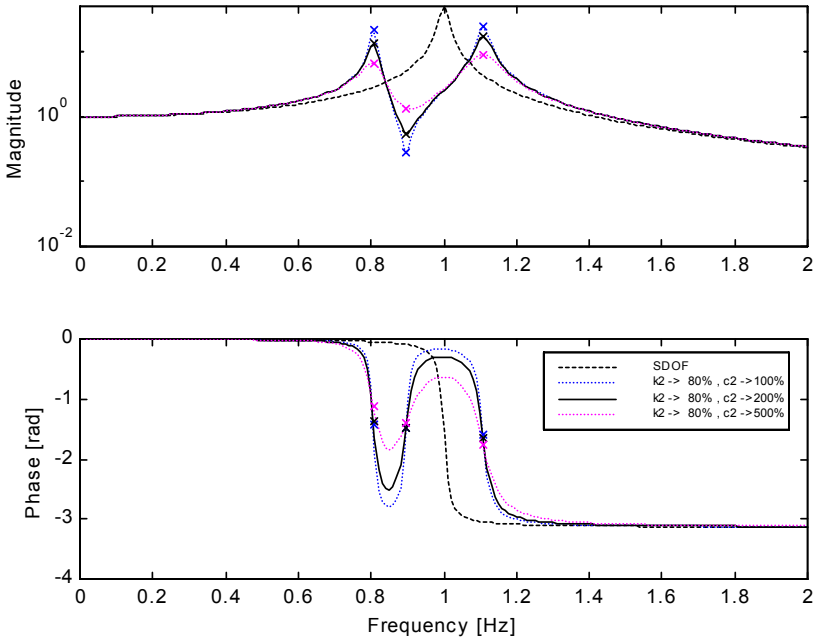

Figure 93: Frequency Response Functions for SDOF and TVA with varied stiffness & damping $(m_1/m_2 = 10, \zeta_1 = 1\%)$

This section has demonstrated the effects on the frequency response function of altering the absorber stiffness, damping, and mass variables. It has shown that a 20% change in stiffness from a tuned passive absorber results in close to a 10% change in the system minimum response frequency. Therefore an active or semi-active tuned absorber can take advantage of this relationship.

System Testing for Variable Gaps

The following experiment compares the expected theoretical stiffness from the earlier experiments with the dynamic stiffness demonstrated in the transfer function. The system is tested with accelerometers on the primary mass and the excitation base. The experimental system parameters are listed in Table 14.

Table 14: Experimental System Parameters

Variable	Value	Units	Measurement Method
m_1	0.8693	kg	Static Measurement
m_2	0.218	kg	Static Measurement
c_1	0.850	N/(m/s)	SDOF Dynamically determined
c_2	variable	N/(m/s)	2-DOF Dynamically determined
k_1	2750	N/m	SDOF Dynamically determined
k_2	variable	N/m	2-DOF Dynamically determined

The system transfer functions between x_1 and u were recorded and curve fit in Figure 95 - Figure 103. These figures depict the experimental transfer functions and the curve fit transfer function. First, the SDOF transfer function (Figure 95) is curve fit to estimate the primary system damping (c_1) and stiffness (k_1). Then, the two degree of freedom transfer functions, Figure 96 to Figure 103, are curve fit to estimate the appropriate varied stiffness and damping coefficients, given that the primary system is unchanged. Table 15 summaries the measured stiffness and the theoretic predicted stiffness. Figure 94 graphs these stiffness values for the various gaps. The experimental achieved values deviate significantly from the theoretical values. These deviations can be caused by significant non-linearity present in the dynamic system and the belief that the dual sided stiffness is indeed an inverse square

relationship. Figure 94 demonstrates that while the stiffness does increase with reduced gap, it appears to be stronger than anticipated for the smaller gaps and less than anticipated for larger gaps, this could indicate that a larger exponent is necessary on the inverse relationship than the 2 that was curve fit.

Table 15: Experimental Stiffness compared to Theoretical Stiffness

Gap, x_0 [mm]	Experimental Stiffness [N/m]	Theoretical Linear Stiffness [N/m]
	$\tilde{k}_1$	
SDOF	2750	
	$\tilde{k}_2$	$\bar{k}_2$
11.0	1245	3130
15.0	957	1250
20.0	714	530
22.0	626	400
24.0	543	309
26.0	461	243
28.0	349	195
30.0	261	159

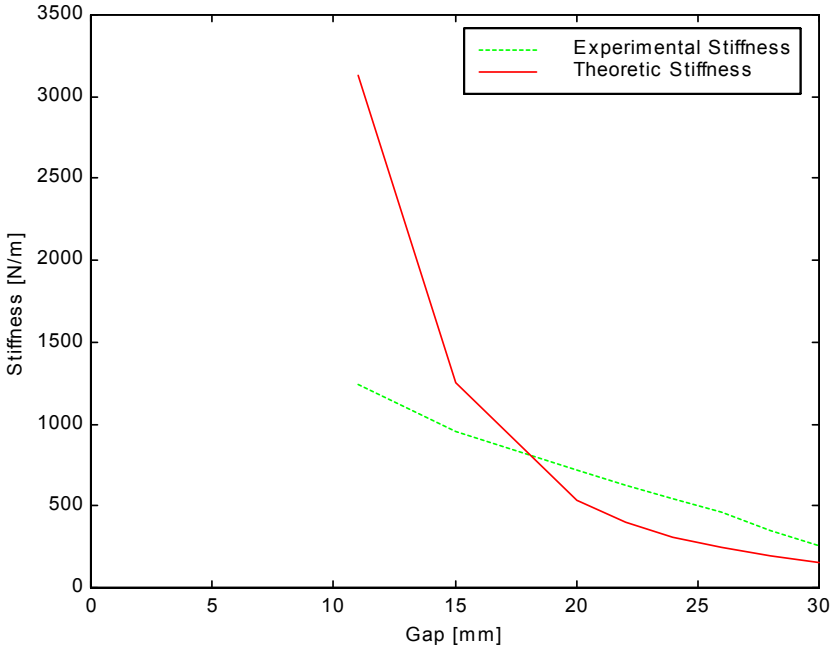

Figure 94: Experimental and theoretic stiffness for various gaps.

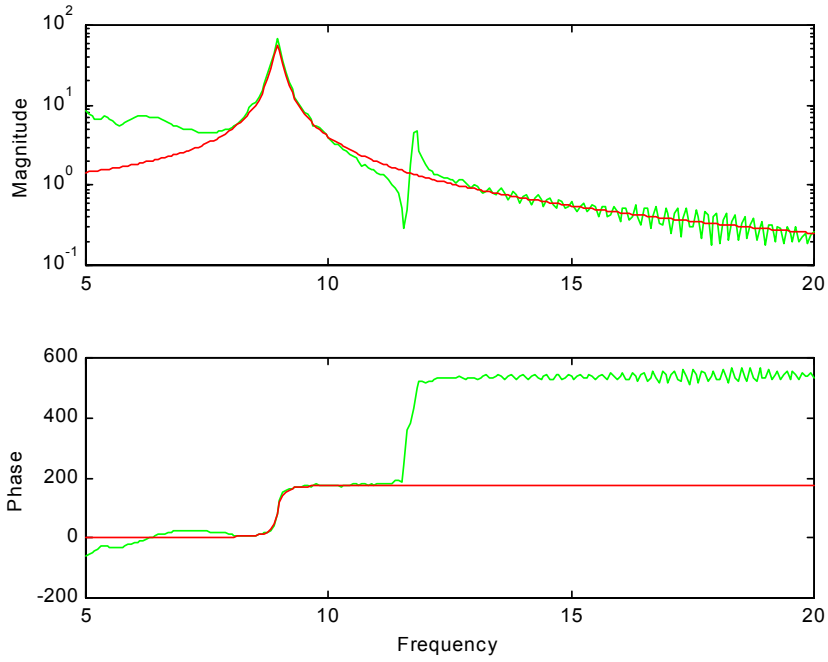

Figure 95: Transfer Function: x_1/u SDOF

m_1=0.8693 kg, $\tilde{c}_1$=0.8497 N/(m/s), $\tilde{k}_1$=2750 N/m

$\tilde{f}_n$=8.95Hz, $\tilde{\zeta}$=0.00869

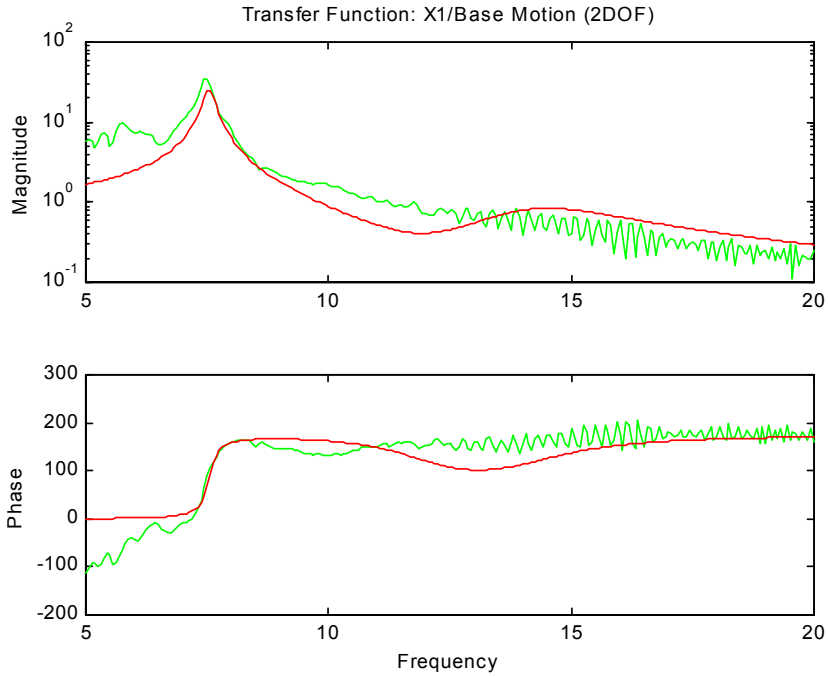

Figure 96: Frequency Response Functions for 2-DOF varied gap – 11.0mm gap
m_2 =0.218 kg, $\tilde{c}_2$ =3.64 N/(m/s), $\tilde{k}_2$ = 1245 N/m

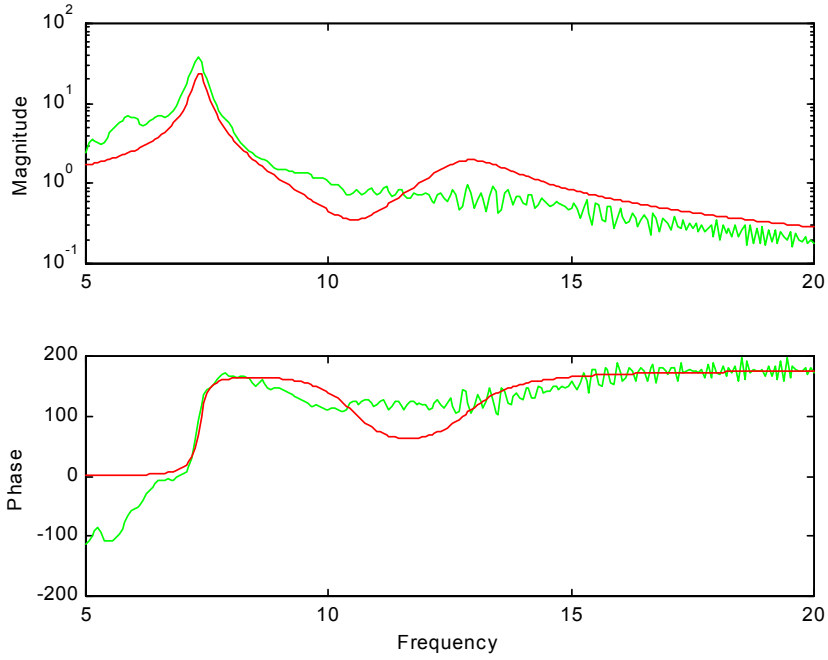

Figure 97: Frequency Response Functions for 2-DOF varied gap – 15.0 mm gap
m_2 =0.218 kg, $\tilde{c}_2$ =1.86 N/(m/s), $\tilde{k}_2$ = 957 N/m

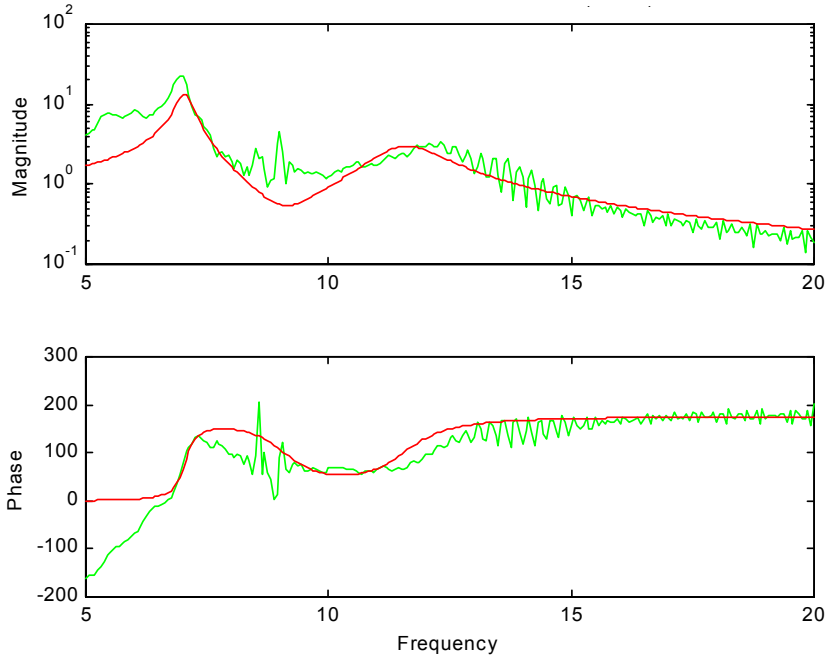

Figure 98: Frequency Response Functions for 2-DOF varied gap – 20.0 mm gap
m_2 =0.218 kg, $\tilde{c}_2$ = 1.80 N/(m/s), $\tilde{k}_2$ = 714 N/m

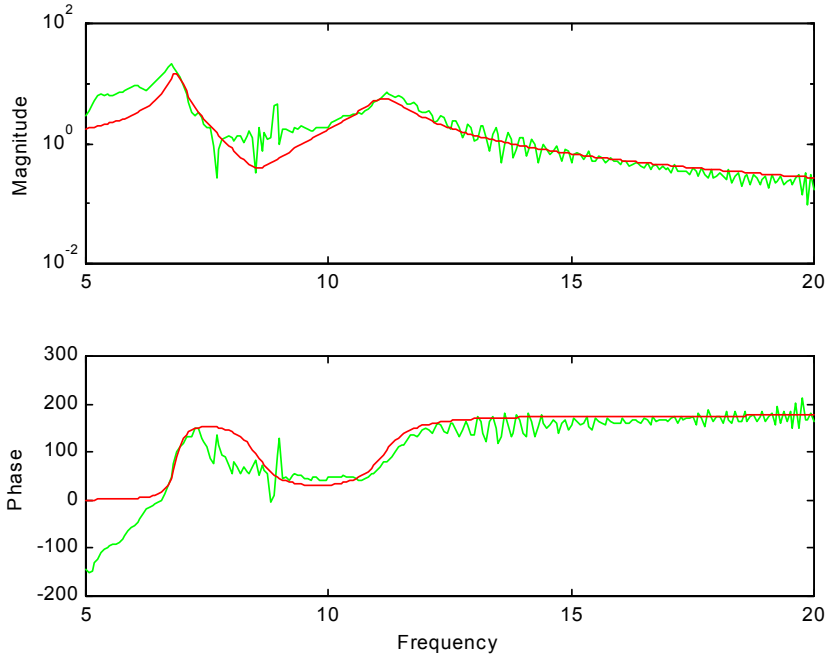

Figure 99: Frequency Response Functions for 2-DOF varied gap – 22.0 mm gap
m_2 =0.218 kg, $\tilde{c}_2$ = 1.07 N/(m/s), $\tilde{k}_2$ = 626 N/m

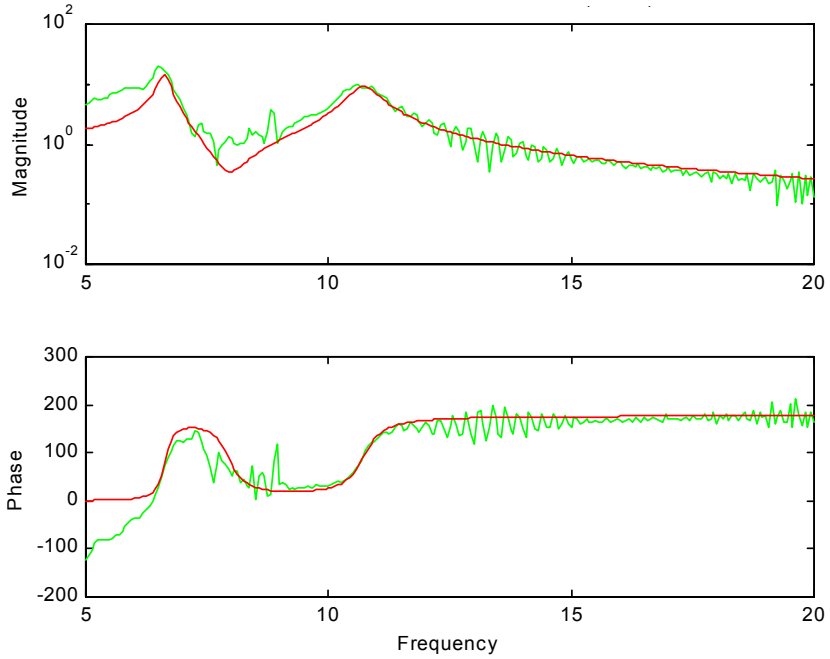

Figure 100: Frequency Response Functions for 2-DOF varied gap – 24.0 mm gap
m_2 =0.218 kg, $\tilde{c}_2$ = 0.74 N/(m/s), $\tilde{k}_2$ = 543 N/m

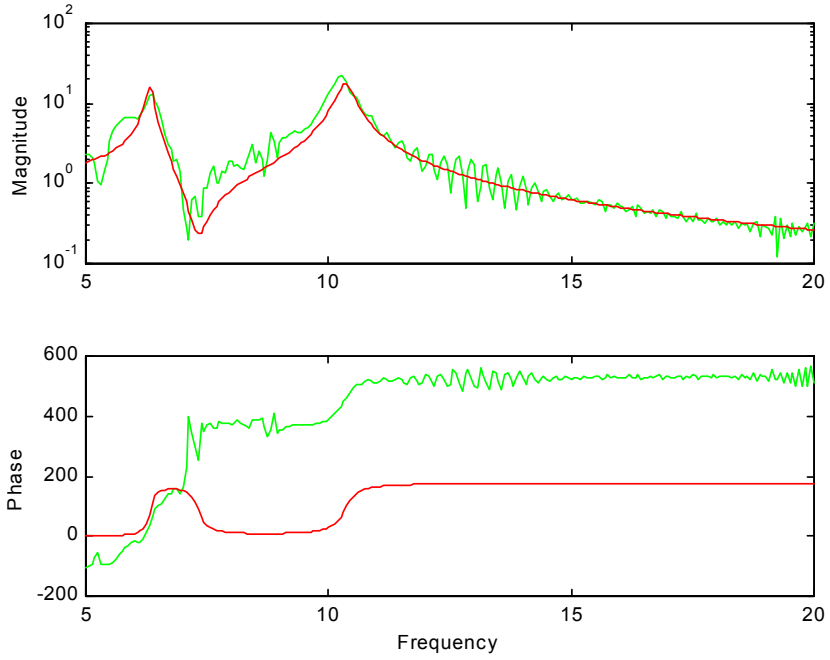

Figure 101: Frequency Response Functions for 2-DOF varied gap – 26.0 mm gap
m_2 =0.218 kg, $\tilde{c}_2$ = 0.39 N/(m/s), $\tilde{k}_2$ = 461 N/m

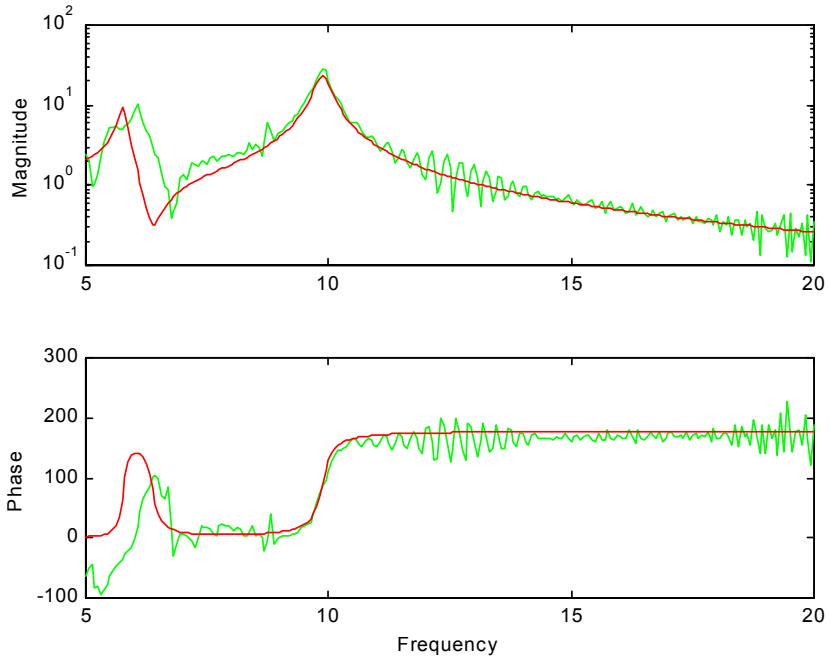

Figure 102: Frequency Response Functions for 2-DOF varied gap – 28.0 mm gap
m_2 =0.218 kg, $\tilde{c}_2$ = 0.35 N/(m/s), $\tilde{k}_2$ = 349 N/m

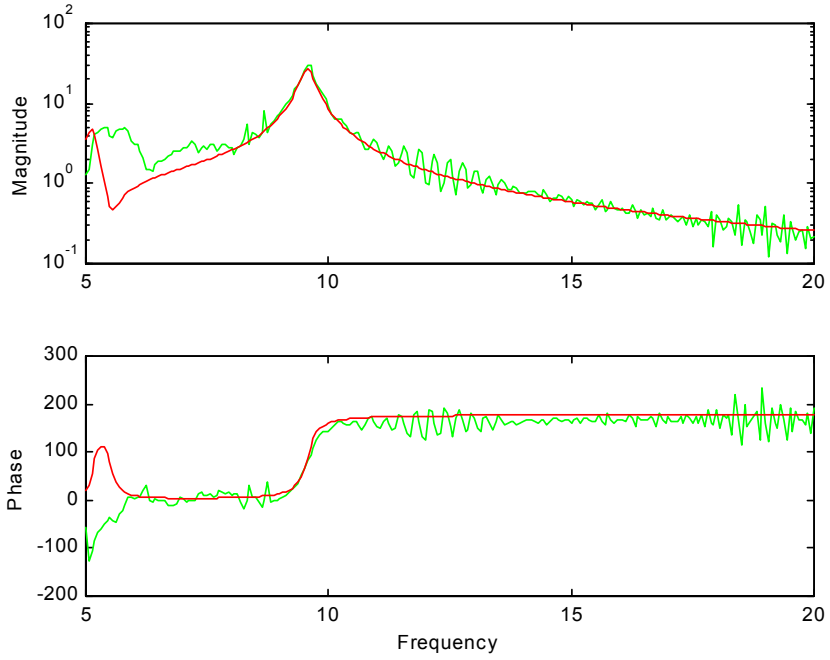

Figure 103: Frequency Response Functions for 2-DOF varied gap – 30.0 mm gap
m_2 =0.218 kg, $\tilde{c}_2$ = 0.37 N/(m/s), $\tilde{k}_2$ = 261 N/m

Conclusions

This chapter has examined the force equations predicted by the inverse square model postulated in Chapter 4 and the relation to the absorber design and dynamic use. Figure 94 demonstrates that while the stiffness does increase with reduced gap, it appears to be stronger than anticipated for the smaller gaps and less than anticipated for larger gaps. This indicates that the inverse square model may not adequately capture the dynamic stiffness that was captured in the transfer functions. The next chapter examines additional dynamic testing of the actuator.

CHAPTER 9. SYSTEM DYNAMIC TESTING

This chapter examines the absorber dynamic testing. The absorber acceleration to base acceleration transfer functions (TF) of the single degree of freedom (SDOF) absorber are presented for different gaps and different current levels. The effects on the absorbers transfer function for changing gap and currents will be demonstrated. These tests demonstrate and isolate the electromagnetic absorber's variable dynamics.

The two degree of freedom tests demonstrate the changing combined system transfer functions (primary system acceleration to base acceleration) for various gaps using a given primary system. These demonstrate how the absorber could be tuned to minimize response based on the excitation frequency.

SDOF Experiments

The magnetic absorber is characterized by the transfer functions between the base acceleration ($\ddot{y}$) and the absorber mass acceleration ($\ddot{x}$). The frequency domain acceleration-to-acceleration transfer function (s^2X/s^2Y) is equivalent to the displacement-to-displacement transfer function (X/Y). These transfer functions are considered since the configuration is comparable to a base excitation problem. The first set of experiments reported are the variable gap system TF. The second experimental set implementing variable current had limited success, as the simulations in Chapter 6 predict very small changes in the system parameters.

The experimental transfer function is best found using a periodic chirp signal for shaker excitation. The acceleration is recorded on the base ($\ddot{y}$) and on the absorber ($\ddot{x}$). The frequency range is 0-25 Hz, 10 averages are taken to limit the random noise effects. The system diagram is presented in Figure 104. These experimental transfer functions are used to determine the absorber system's damping and natural frequency. A least squares curve fit algorithm is used to minimize the error of the experimental data to the theoretical fit. The sum of the residuals are minimized across the range of possible values for the damping and natural frequency.

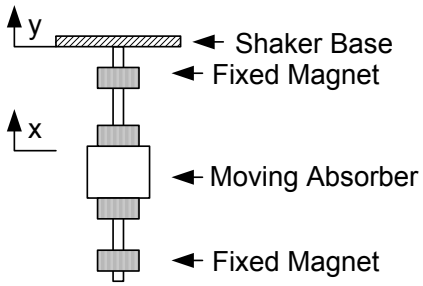

Figure 104: Single DOF Absorber System

Variable Gap

Figure 105 shows the TF of the electromagnetic absorber system with the outer magnets in the closest position. The natural frequency of the equivalent linear curve fit system is 21.8 Hz, with a damping ratio of 6.7%. The TF curve fit that minimizes the residuals is represented in the graph with the smooth line. Figure 106 shows that the experimental test coherence is near to one above 4 Hz. This indicates that the experimental transfer function is reliable above 4 Hz.

The absorber's damping is high, yet as expected based on the prior chapters experiments. Chapter 7 found the mechanical damping between 4.5%-6.0% and the electromagnetic damping around 1.6%. Given a total damping ratio range of 6.1%-7.6%. The mechanical damping present needs to be reduced for future experiments, since this large damping reduces the effective cancellation possible.

Figure 107 is the transfer function for the medium gap setting, with Figure 108 the related coherence function. This demonstrates for a change in x_0 of 7.1 mm (or a total gap widening of 14.2 mm) a frequency shift of 40% results. Figure 109 & Figure 110 are the results from the wide gap experiment. Table 16 summaries the parameter variations based on the variable gap. This table demonstrates the ability to significantly shift the natural frequency of the electromagnetic absorber based on the gap setting. This shift can be used to select the appropriate gap for various excitations.

In the examination of the coherence plots it is noticed that the coherence reduces near resonances as the gap is increased. This indicates that with larger gaps, the first order response is not the only system response. Since the spring force is an inverse square relationship it is expected that frequencies may

appear that did not exist on the vibration input. This nonlinear effect can result in additional vibration at frequency multiples. This can be the result of the increased non-linearity associated with larger gaps.

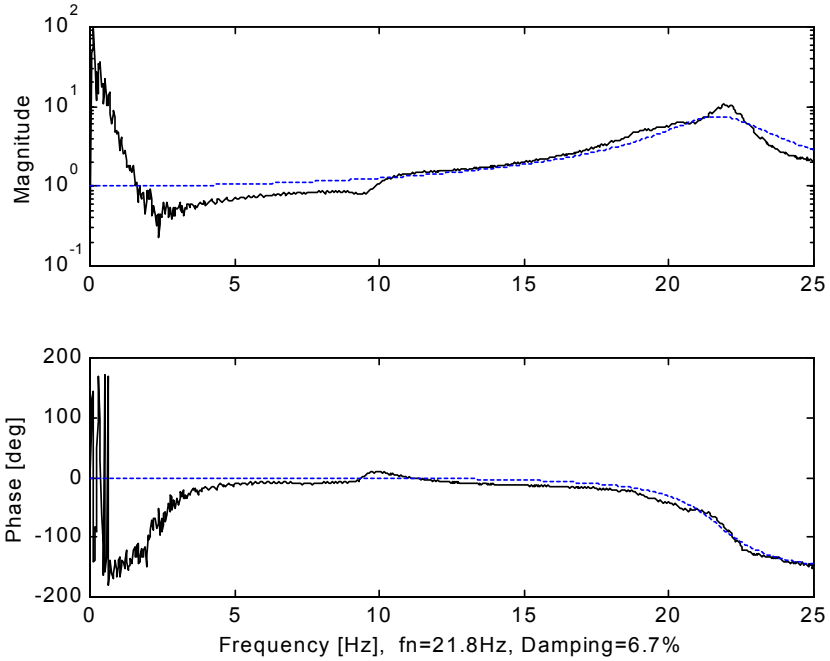

Figure 105: X/Y TF for Smallest Gap
[x_0 = 10.3 mm, f_n=21.8 Hz, ζ =6.7%]

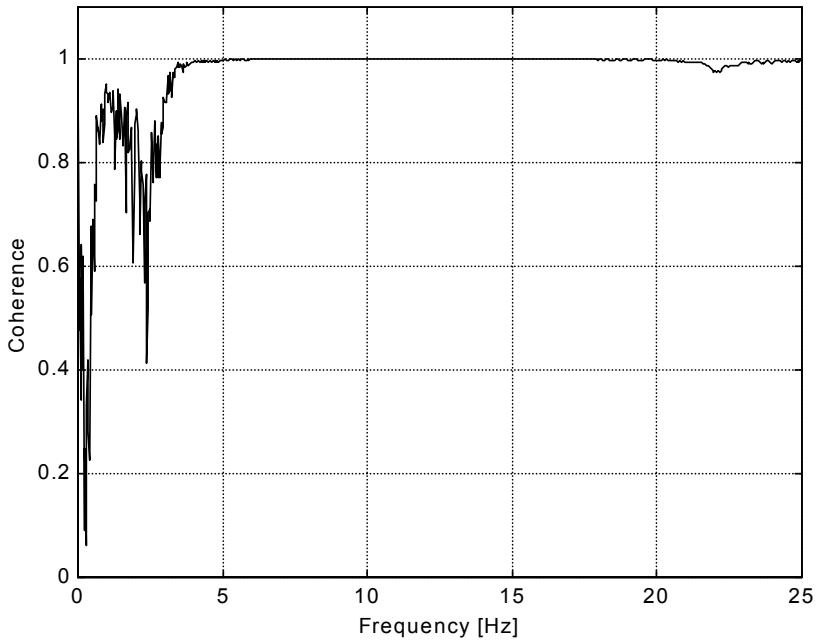

Figure 106: X/Y TF Coherence [x_0 = 10.3 mm]

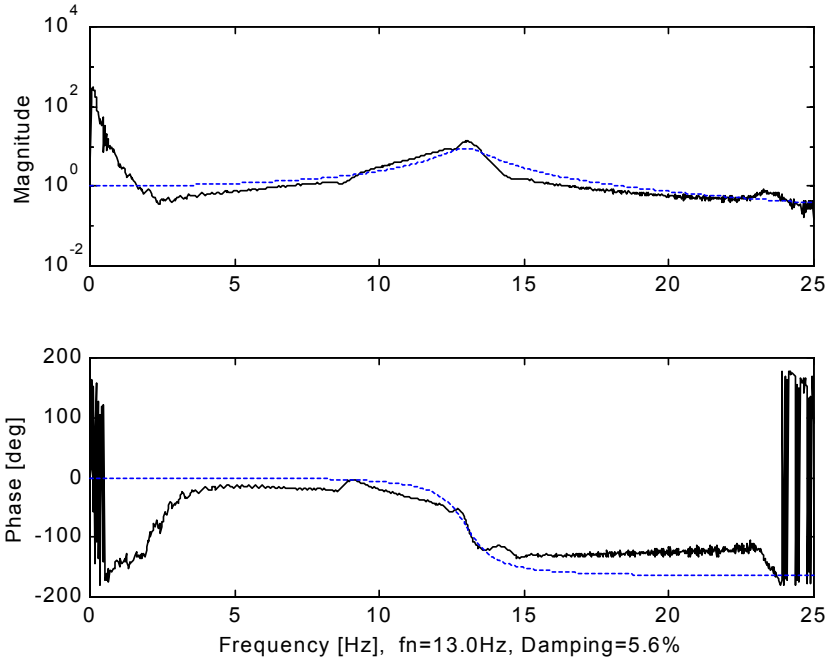

Figure 107: X/Y TF for Medium Gap
[x_0 = 17.2 mm, f_n=13.0 Hz, ζ =5.6%]

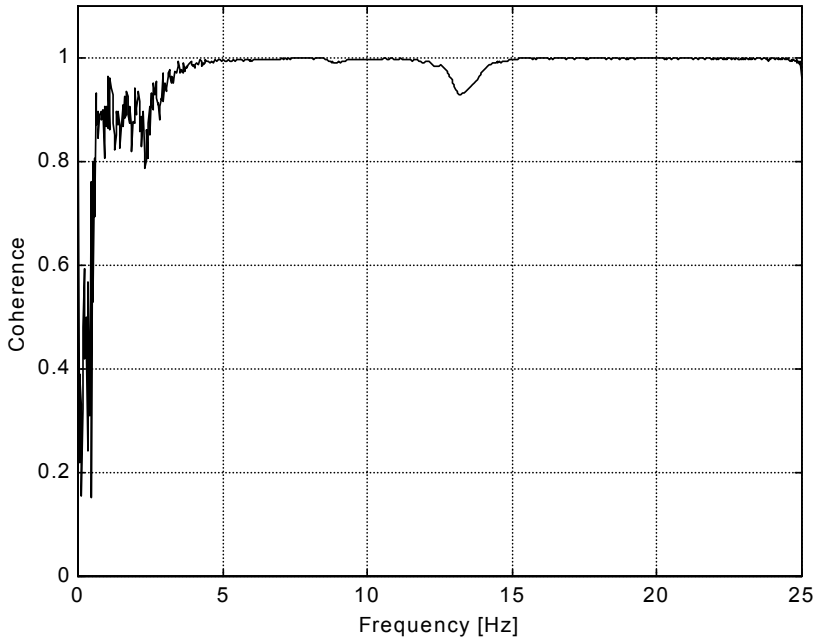

Figure 108: X/Y TF Coherence for Medium Gap
[x_0 = 17.2 mm]

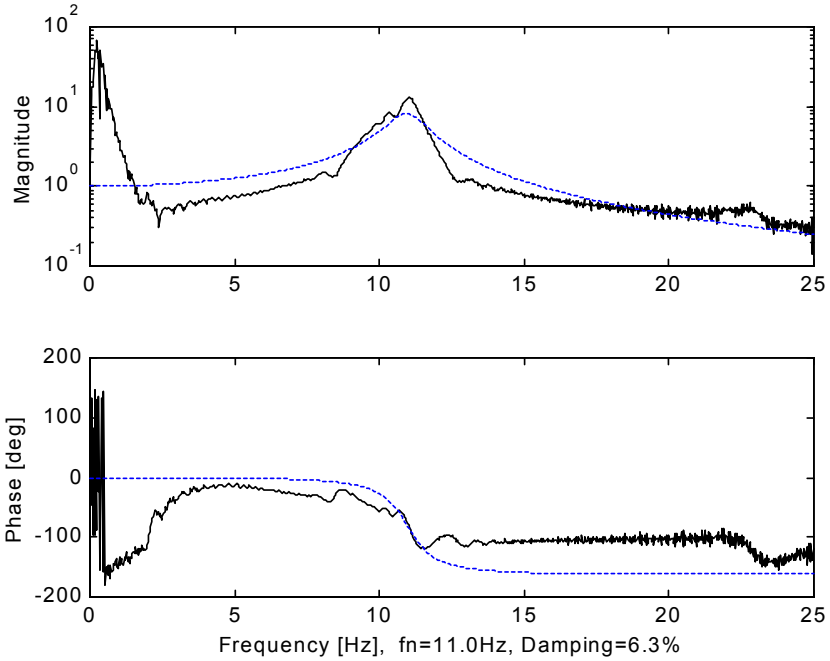

Figure 109: X/Y TF for Wide Gap
[x_0 = 19.9 mm, f_n=11.0 Hz, ζ =6.3%]

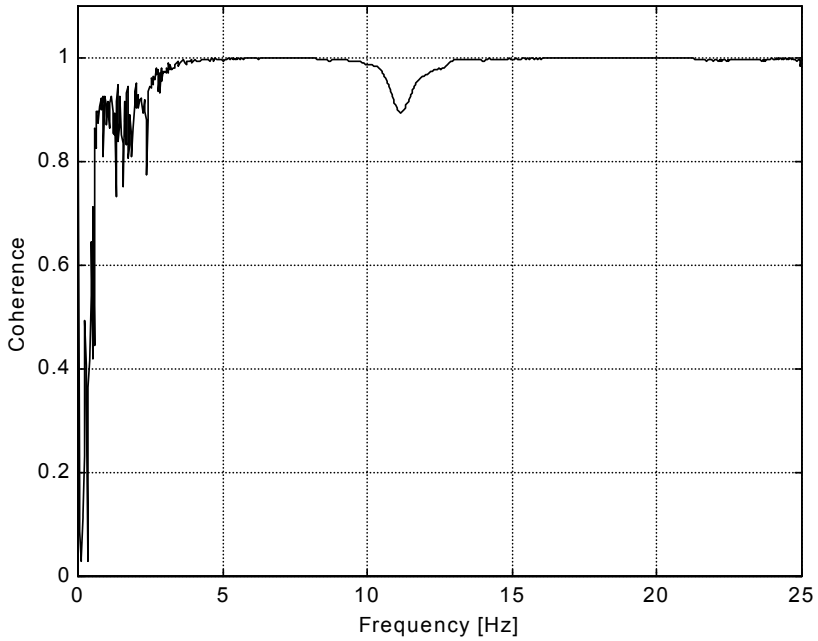

Figure 110: X/Y TF Coherence for Wide Gap
[x_0 = 19.9 mm]

Table 16: Experimental Variation of Parameters for a Variable Gap

Gap [mm]	Curve Fit Natural Frequency [Hz]	Curve Fit Damping Ratio %
10.3	21.8	6.7
17.2	13.0	5.6
19.9	11.0	6.3

Simulations with Experimental Force Relationship

The following simulations are done using the experimental system's measured spring force. This enables comparison between the theory and the experiments. The inverse square force relationship is used along with an estimate of the damping (c=1 Ns/m) from the experiments in Chapter 7. The base motion is simulated as 0.4 mm. Figure 111 shows the simulated transfer function response for the smallest gap. The experimental TFs do not have the discontinuities that are present in the theoretical simulations. Increasing the damping in the simulations will lead to elimination of the jumps. A SDOF curve fit of the simulated data allows the equivalent natural frequency and damping ratio to be calculated.

Figure 111-Figure 113 demonstrate the increased damping coefficients effect on the system. The larger viscous damping simulated the less of a jump is experienced in the magnitude and phase relationship.

Table 17 summaries the equivalent natural frequencies and damping ratios from the simulation and the experimental work. It demonstrates that the natural frequencies estimated are near each other for the theoretic and simulations.

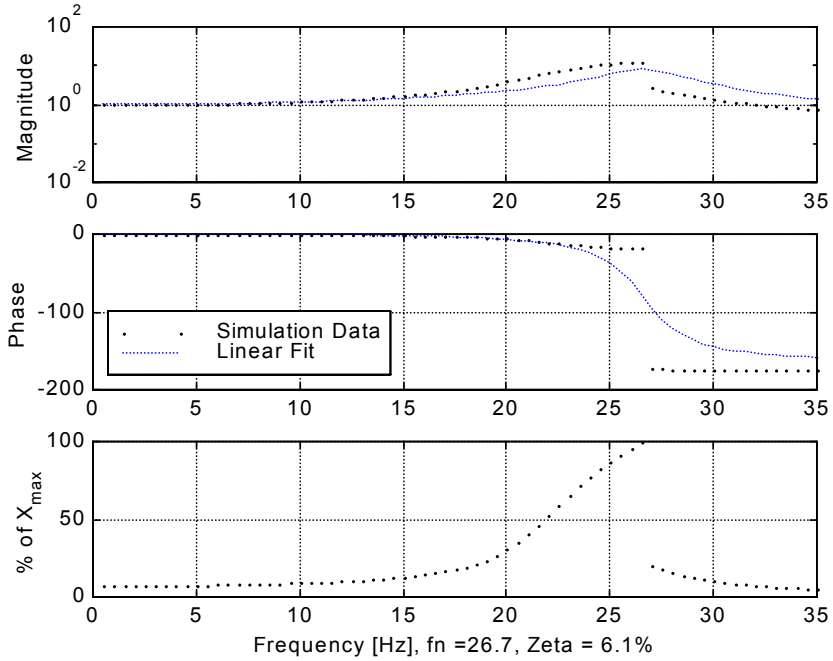

Figure 111: X/Y TF for Smallest Gap Simulation [c=1.0Ns/m] [x_0=10.3 mm, f_n=26.7 Hz, ζ =6.2%]

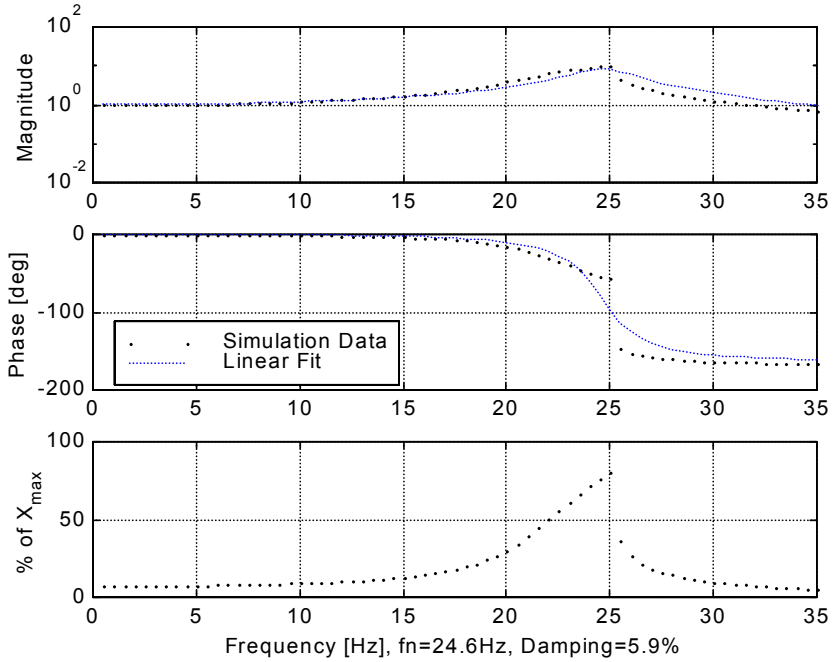

Figure 112: X/Y TF for Smallest Gap Simulation [c=3.0Ns/m] [x_0 = 10.3 mm, f_n=24.6 Hz, ζ =5.9%]

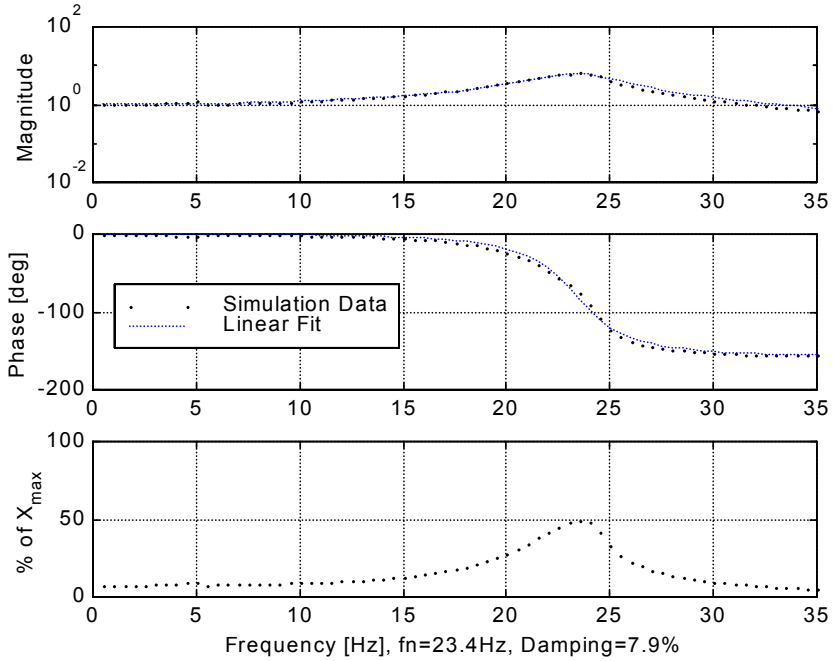

Figure 113: X/Y TF for Smallest Gap Simulation [c=5.0Ns/m]
[x_0 = 10.3 mm, f_n = 23.4 Hz, ζ =7.9%]

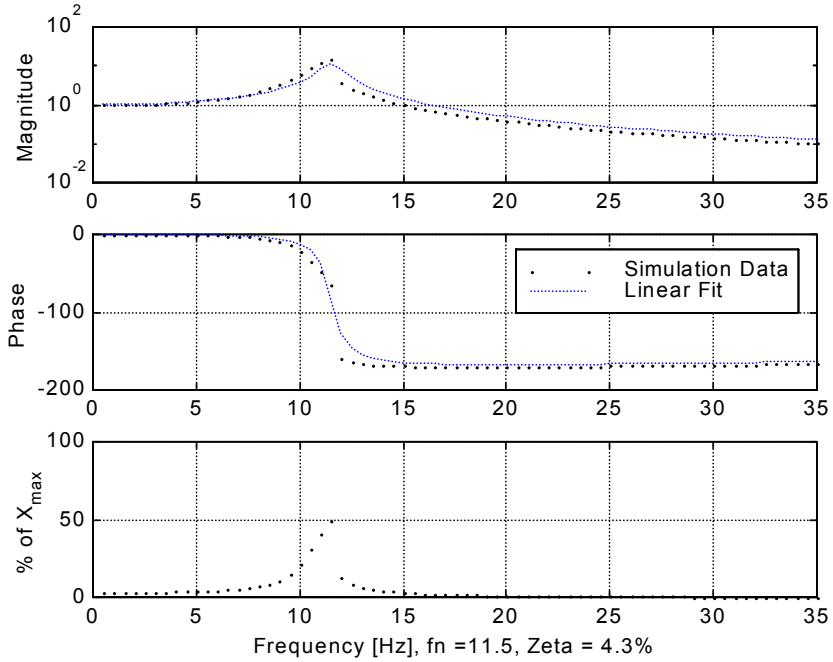

Figure 114: X/Y TF for Medium Gap Simulation
[x_0 = 17.2 mm f_n = 11.5 Hz ζ = 4.3%]

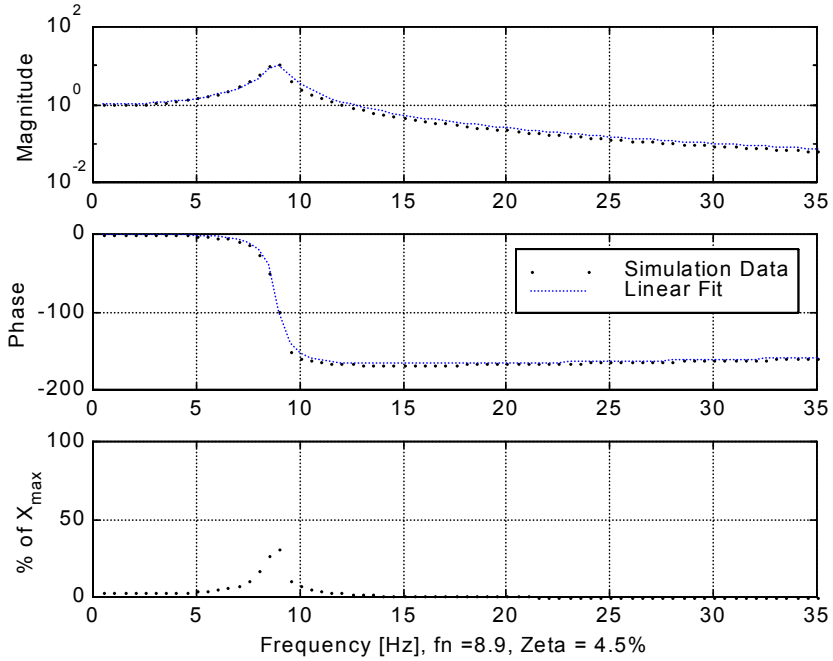

Figure 115: X/Y TF for Wide Gap Simulation
[x_0 = 19.9 mm f_n = 8.9 Hz ζ = 4.5%]

Table 17: Simulated and Experimental Variation of Parameters for Variable Gap

Gap [mm]	Experimental Natural Frequency [Hz]	Experimental Damping Ratio %	Simulation Natural Frequency [Hz]	Simulation Damping Ratio %
10.3	21.8	6.2	26.7	6.2
17.2	13.0	5.0	11.5	4.3
19.9	11.0	5.7	8.9	4.5

Gap [mm]	Experimental Natural Frequency [Hz]	Experimental Damping Ratio %	Simulation Natural Frequency [Hz]	Simulation Damping Ratio %
10.0	22.0	6.4		
10.3	21.8	6.2	26.7	6.2
11.0	20.3	6.2	28.0	5.8
12.0	18.7	5.7		
13.0	17.4	4.4		
14.0	16.1	4.5		
15.0	14.8	4.6		
16.0	14.1	4.6		
17.0	12.7	5.4		
17.2	13.0	5.0	11.5	4.3
18.0	12.3	4.6		
19.0	11.8	3.6		
19.9	11.0	5.7	8.9	4.5
20.0	11.1	3.7		
21.0	10.3	4.2		
22.0	9.7	4.1		
23.0	8.9	4.6		
24.0	8.5	4.7		
25.0	7.6	7.7		

SDOF System with Current Variations

This section examines the system change with a variable DC current input. The simulations from Chapter 6 predict a small shift of the system natural frequency. This small natural frequency shift can be used effectively if the damping was very low, it would provide significant changes in the transfer function. Yet in this case, the large damping does not have allows a dramatic effect in the transfer function minimum. Figure 116 & Figure 117 are the results from the no current case. The coherence

is very poor under 6 Hz. The damping is quite large estimate at just under 10%. Figure 118 & Figure 119 report the results with +5 Amps current supplied to the electromagnet. There is a small shift in the natural frequency as expected. The damping estimate is very high at just under 20%. The experiments show that a small shift can be implemented with the current input, yet this will also increase the electromagnetic damping present.

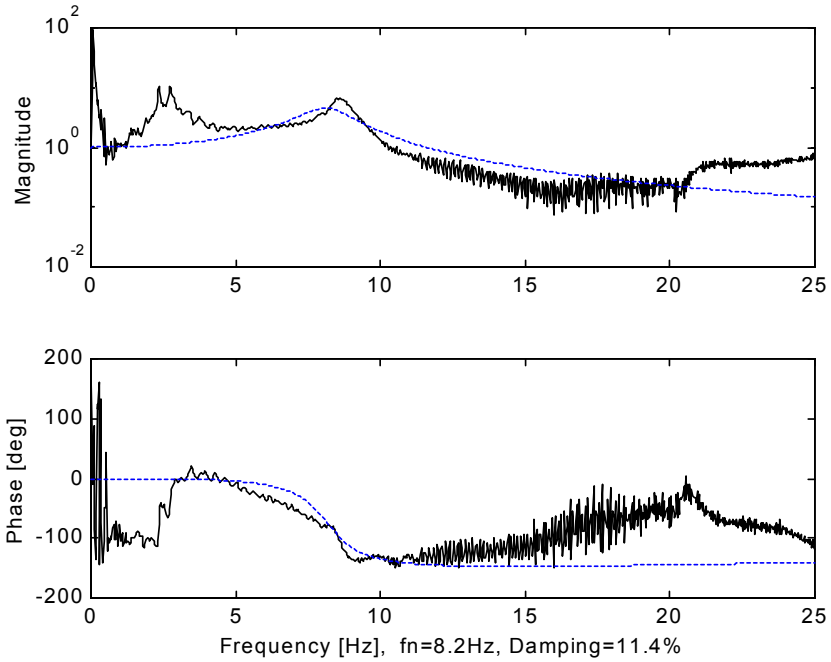

Figure 116: X/Y TF for No Current
[x_0=23.3mm, f_n=8.2Hz, ζ=11.4%]

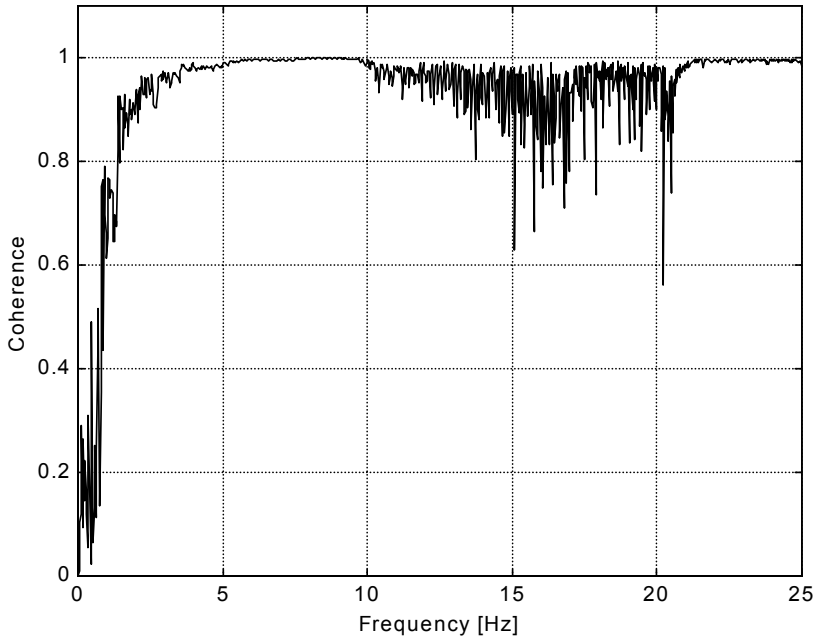

Figure 117: X/Y TF Coherence for No Current
[x_0=23.3mm]

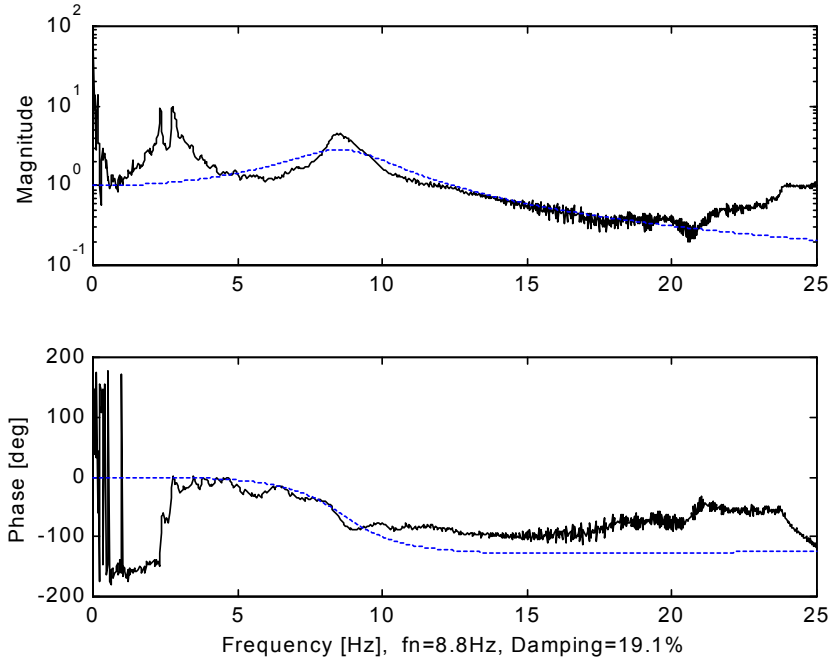

Figure 118: X/Y TF for +5 Amps Current
[x_0=23.3mm, f_n=8.8Hz, ζ =19.1%]

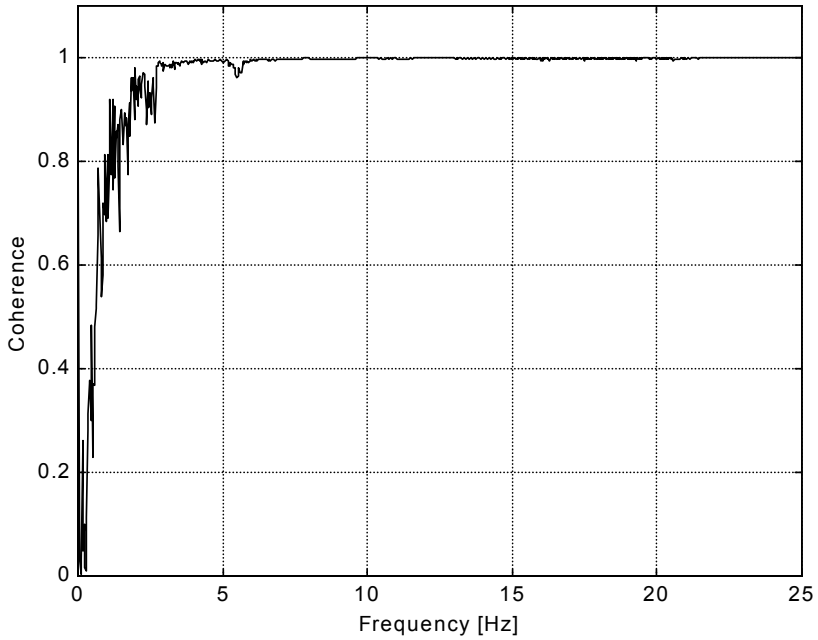

Figure 119: X/Y TF Coherence for +5 Amps Current
[x_0=23.3mm]

2-DOF Experiments

A two degree of freedom system is constructed to test the variable gap settings and its effect on the system frequency response. This primary system consists of a spring, mass and the fixed portion of the TVA. This primary system (w/TVA casing) is a simple one-degree of freedom system (780.3g + 89.0g). The combined system has the moving actuator mass suspended within the electromagnetic field. This combined system is depicted in Figure 120.

Figure 121-Figure 133 depict the change in transfer function response as the magnetic gap is widened. Figure 121 shows the stiffest absorber system. The addition of the absorber shifts the peak response lower by over 1 Hz. It also lessens the response at the prior peak. A second peak response is not present across this frequency range as expected. This primary system vibration response declines between 7.5 Hz and 13 Hz. The phase response has a –180 degree roll off. This stiff absorber system will be the comparison for the other absorber systems.

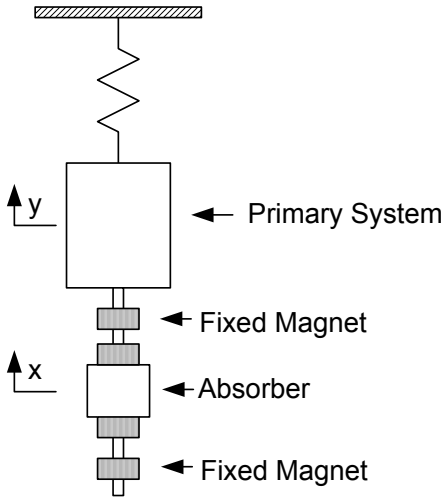

Figure 120: 2-DOF System

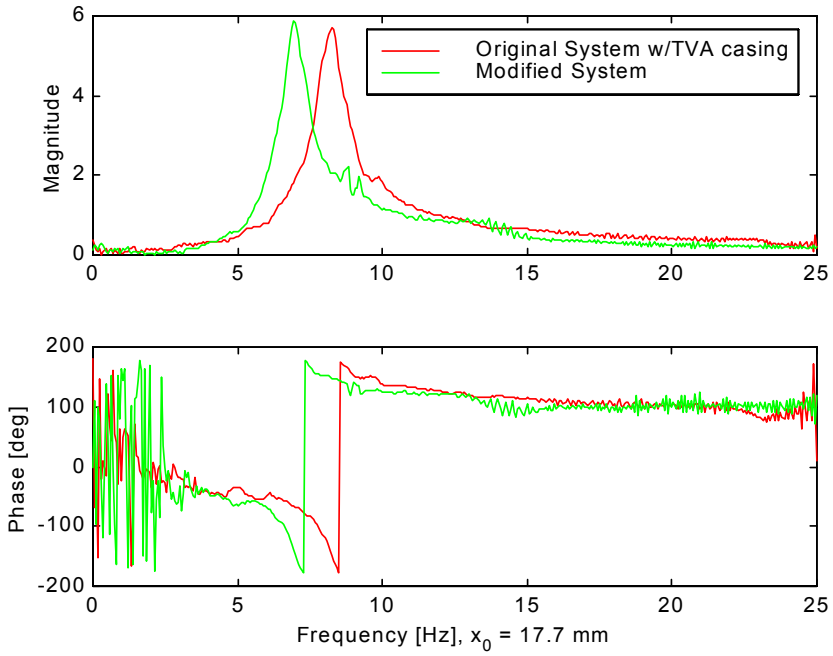

Figure 121: Experiment TF for SDOF and 2-DOF system [x_0 = 17.7mm]

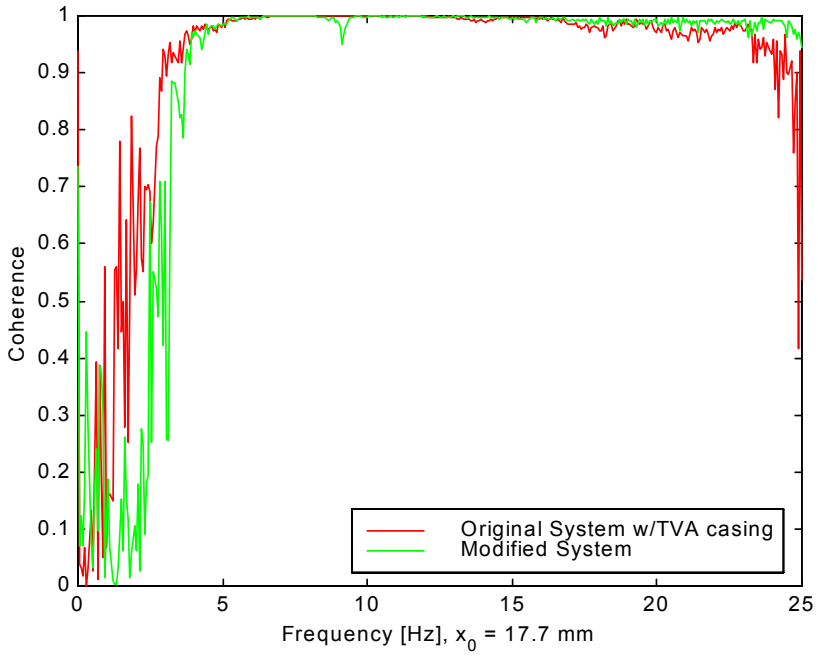

Figure 122: Experiment Coherence for SDOF and 2-DOF system [x_0 = 17.7mm]

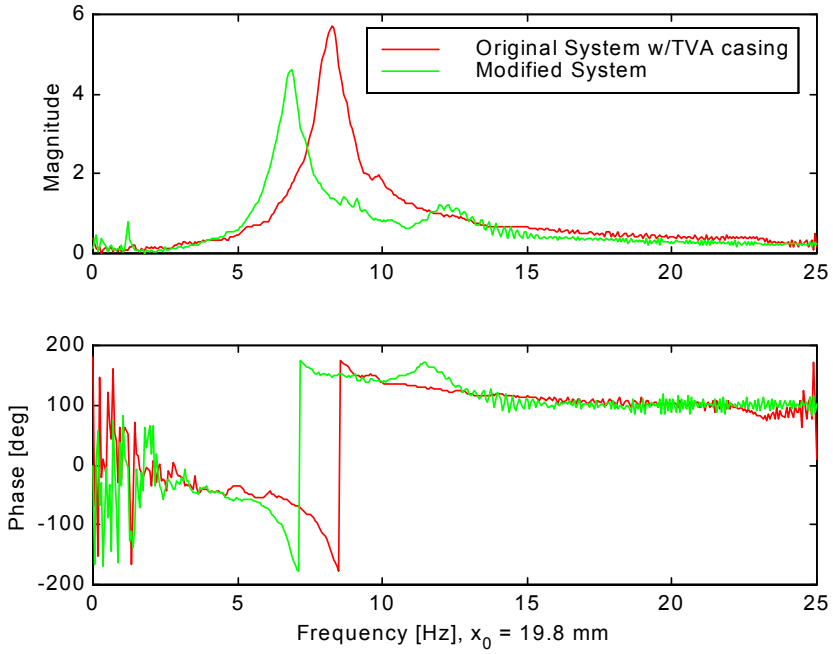

Figure 123: Experiment TF for SDOF and 2-DOF system [x_0 = 19.8 mm]

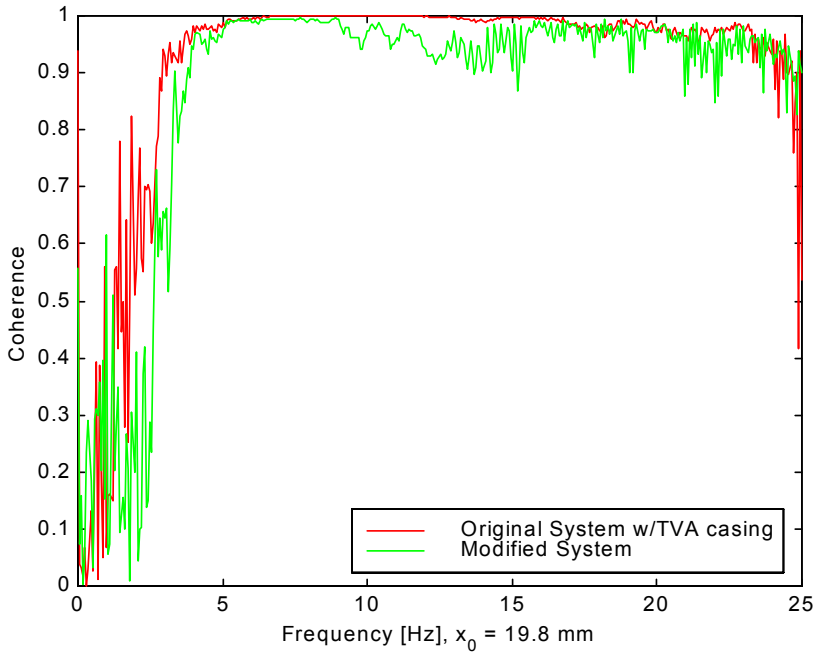

Figure 124: Experiment Coherence for SDOF and 2-DOF system [x_0 = 19.8mm]

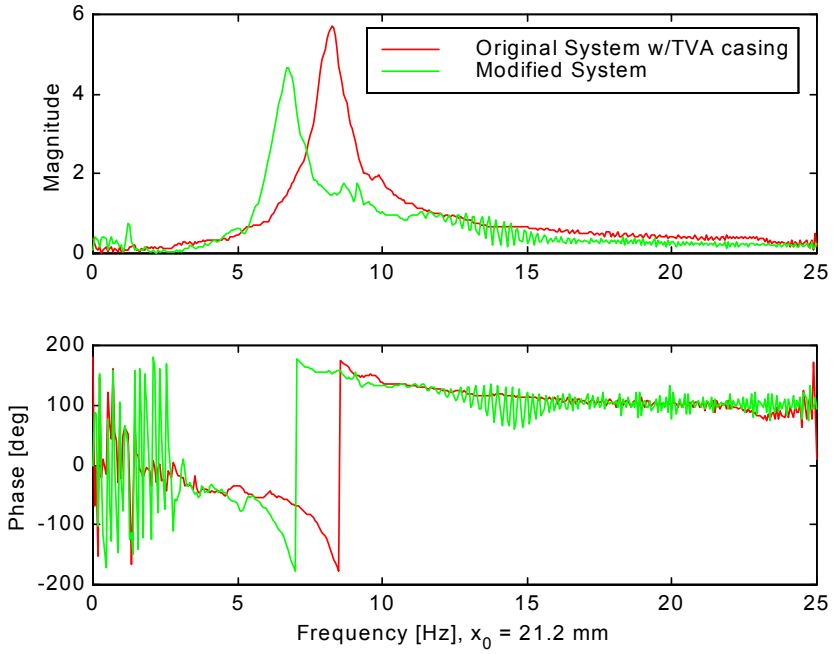

Figure 125: Experiment TF for SDOF and 2-DOF system [x_0 = 21.2mm]

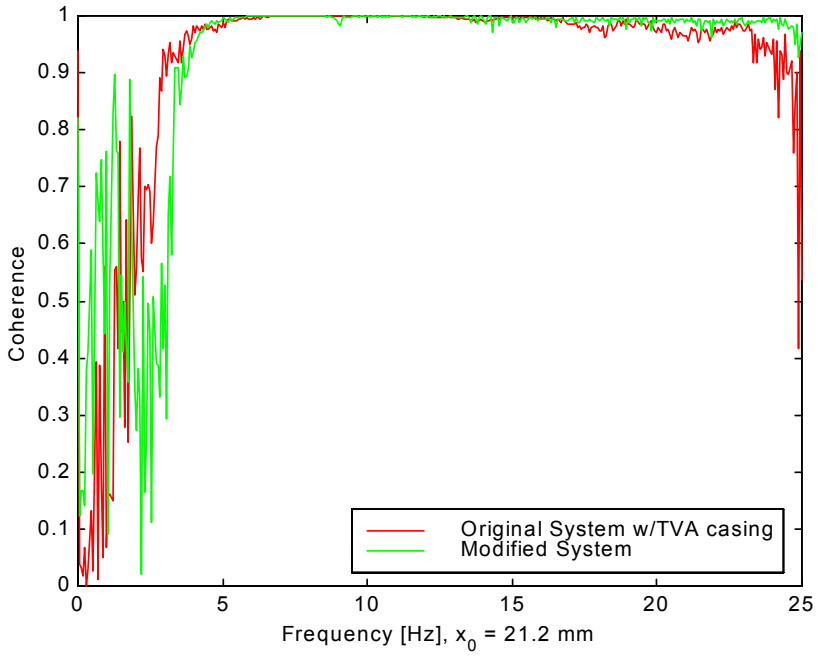

Figure 126: Experiment Coherence for SDOF and 2-DOF system [x_0 = 21.2mm]

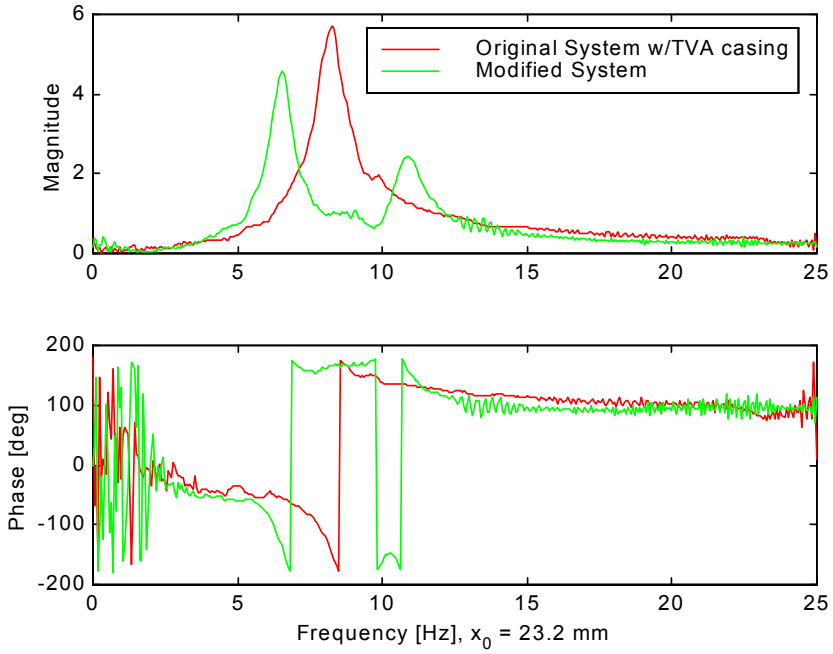

Figure 127: Experiment TF for SDOF and 2-DOF system [x_0 = 23.2mm]

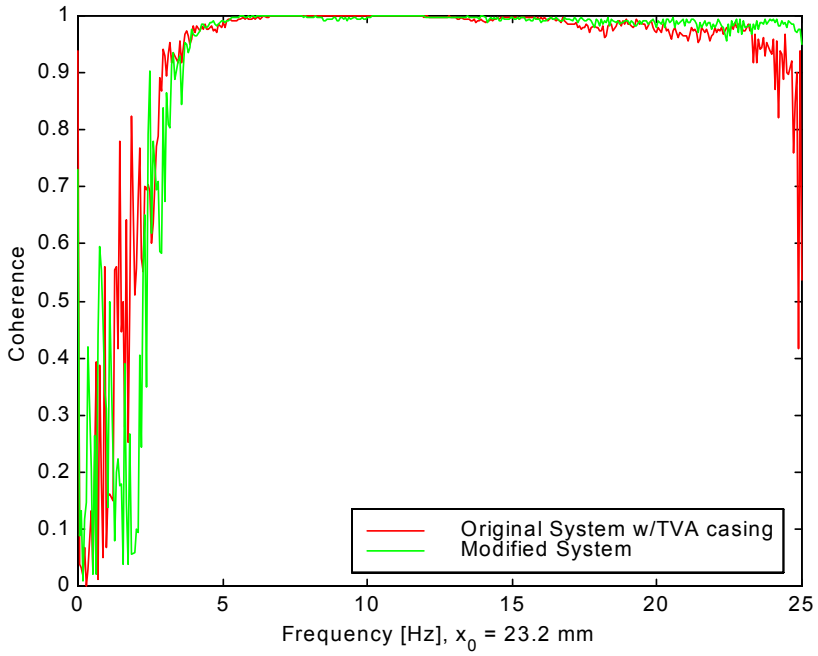

Figure 128: Experiment Coherence for SDOF and 2-DOF system [x_0 = 23.2mm]

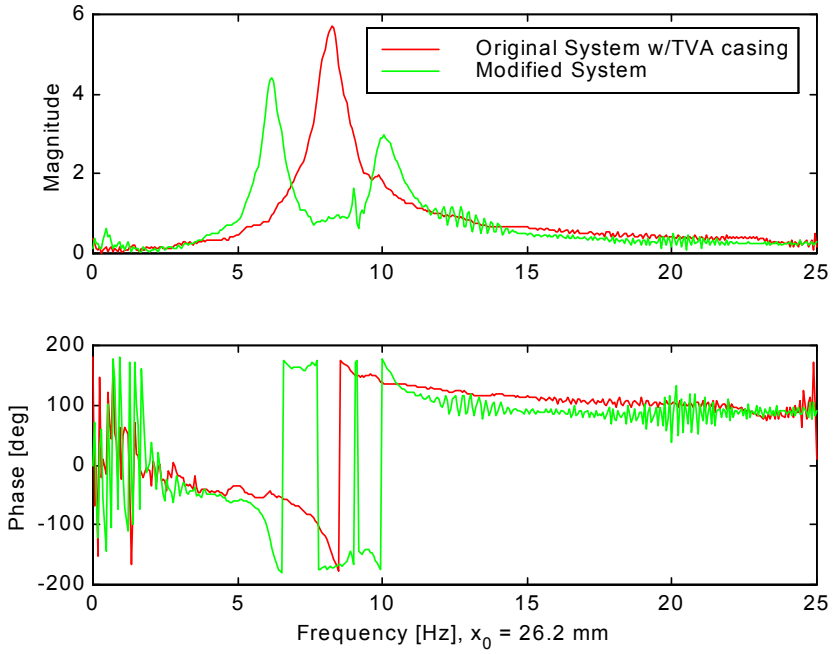

Figure 129: Experiment TF for SDOF and 2-DOF system [x_0 = 26.2mm]

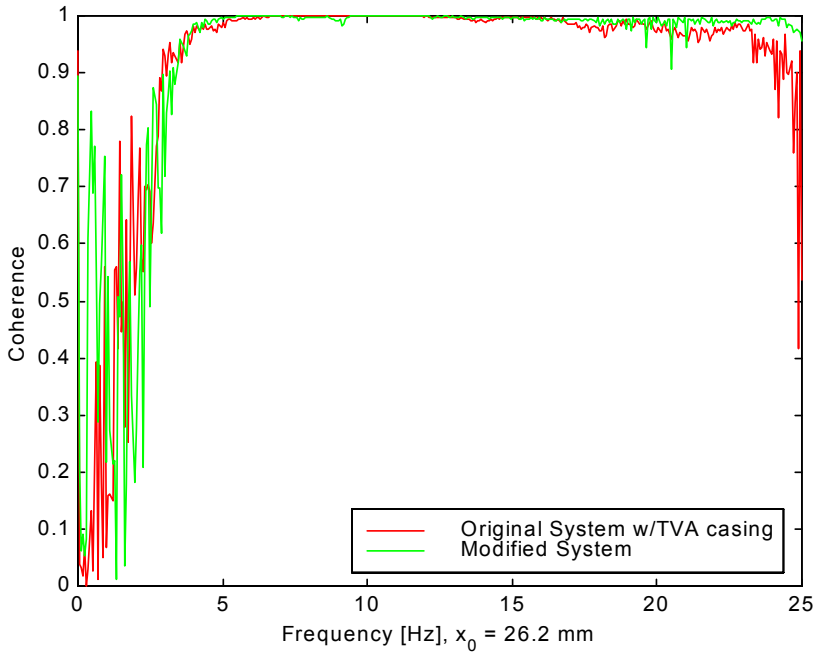

Figure 130: Experiment Coherence for SDOF and 2-DOF system [x_0 = 26.2mm]

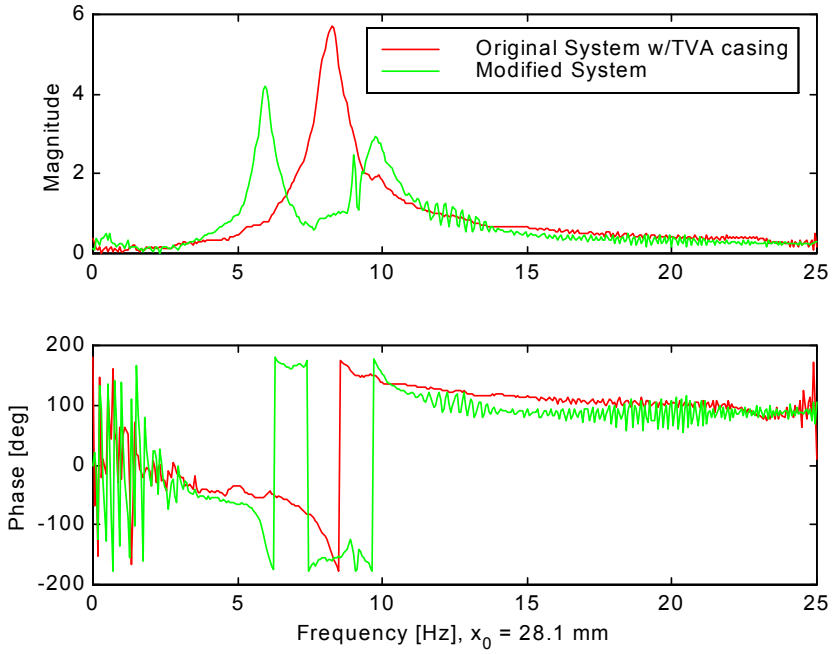

Figure 131: Experiment TF for SDOF and 2-DOF system [x_0 = 28.1mm]

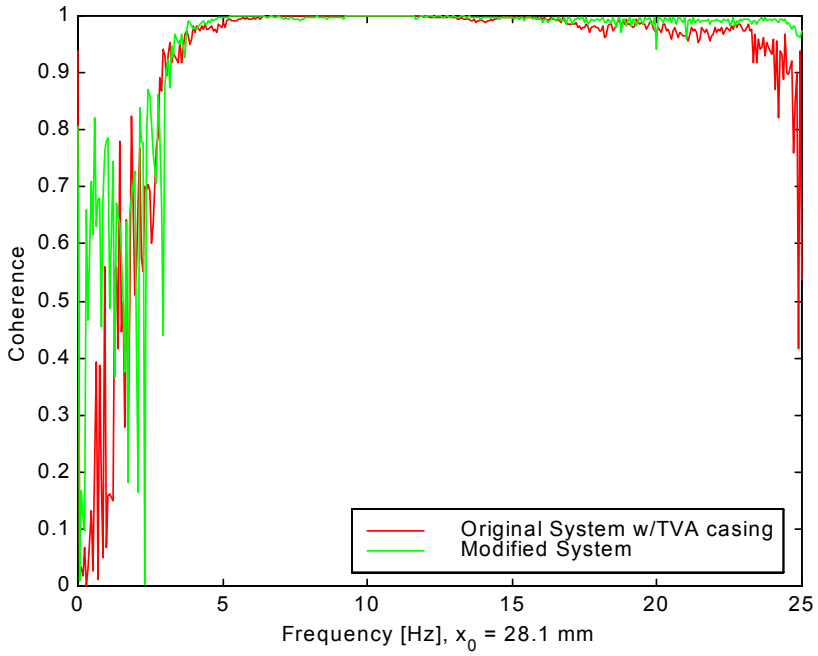

Figure 132: Experiment Coherence for SDOF and 2-DOF system [x_0 = 28.1mm]

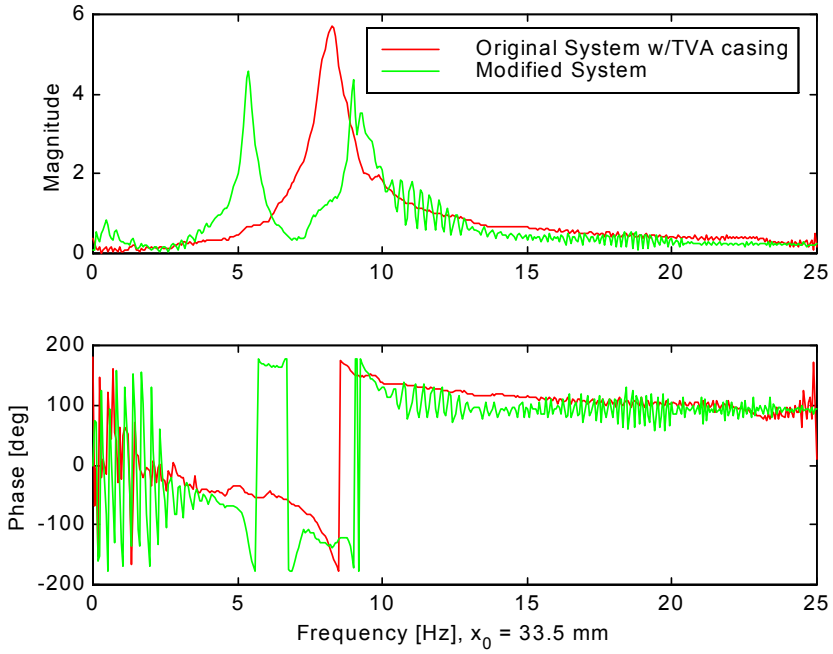

Figure 133: Experiment TF for SDOF and 2-DOF system [x_0 = 33.5mm]

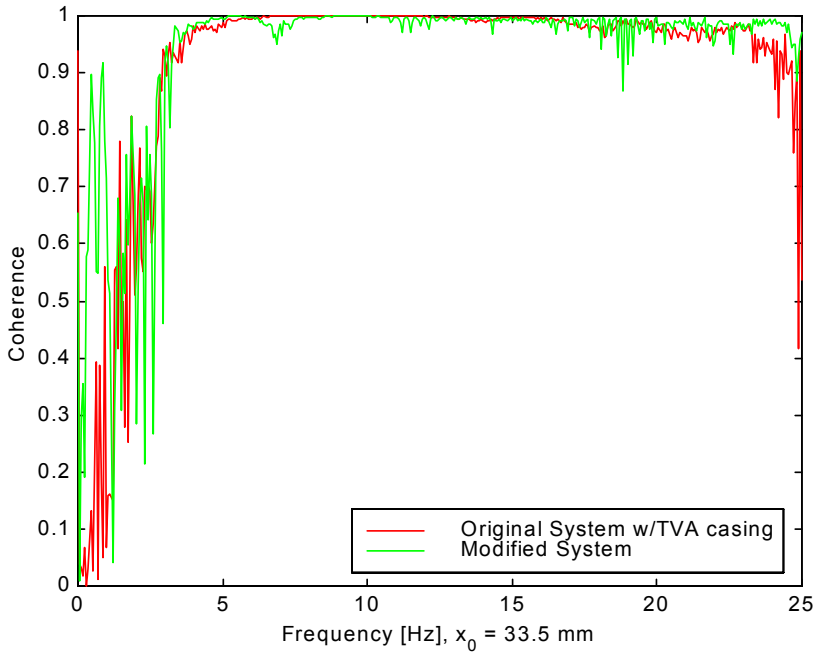

Figure 134: Experiment Coherence for SDOF and 2-DOF system [x_0 = 33.5mm]

Table 18 summarizes the vibration reduction range for adding the absorber mass and adjusting the gap. This shows that as the gap is widened and the effective stiffness drops the reduction band moves to lower frequencies. This demonstrates that the electromagnetic absorber can be effectively varied with the gap setting.

Table 18: Minimized Range for Various Experimental Gaps

x_0 [mm]	Minimized Range Low Point [Hz]	Minimized Range High Point [Hz]
17.7	7.5625	12.875
19.8	7.3750	11.75
21.2	7.3125	11.6875
23.2	7.125	10.375
26.2	6.8125	9.625
28.1	6.625	9.375
33.5	6.125	8.875

Summary

This chapter has reviewed the experimental work done on the electromagnetic absorber. First the absorber's transfer function was characterized with both DC current variation and varying gaps. The DC current variations provided small equivalent linear system parameter variations, this was as predicted by the theoretical development. The varied gap was highly successful with a change in natural frequency of 50% over the range examined.

The two degree-of-freedom system demonstrates the transfer functions variation with various gaps. This system is shown to reduce vibration across a frequency range as determined by the gap spacing and the applied current. The following chapter summaries the contributions of the work.

CHAPTER 10. CONCLUSIONS

Tuned Vibration Absorbers have been in use since the early 1900's. These passive devices have proven useful to reduce vibration at specific design frequencies. A large body of research exists on design variations of Tuned Vibration Absorbers. These papers address the effects of mass ratios, absorber damping, different designs, and additional control methods. This research has addressed the use of an electromagnetic absorber to control vibration. This device can be operated with varying currents or varying mechanical gaps. It was found that the variable gap is a viable method to tune the absorber to different excitation frequencies for extended periods, while varying the current allows quick adjustments.

Theoretical Work

Chapter 3 develops the electromagnetic field equations necessary to predict the electromagnetic force. The electromagnetic field is arrived at by superposition of the constituent contributions. The contributions calculated for the four different components present: the absorber magnets, the absorber coil, the absorber core and the stationary magnets. Chapter 4 takes the resultant electromagnetic field and converts it to a force relationship for various displacements and current levels. This provides the theoretical force to displacement relationship; using continuum mechanics and electromagnetic field relationships. The best fit is an inverse square relation between the displacement and the force between the stationary permanent magnet and the electromagnetic absorber.

Chapter 5 examines the damping mechanisms and how they may affect the experimental work. It discusses a number of damping mechanisms that could be present in the system. Chapter 6 has system dynamics simulations using the parameters found from Chapter 4 & 5. This chapter calculates the SDOF linear equivalent system parameters for the simulations.

Experimental Work

The experimental tests are examined in Chapter 7 - 9. Chapter 7 depicts the absorber design and initial tests to characterize the force and damping relationships. Chapter 7 compares the mechanical and electromagnetic damping present in the absorber system. The spring force relation is confirmed and found to closely be an inverse square relation. The damping is quantified with experiments on the absorber to determine the mechanism responsible. It was found that the mechanical damping is very high and provided 5.0-6.4% of critical damping. Chapter 8 reports experiments related to the actuator design and the challenges of modeling the dynamic stiffness adequately. Chapter 9 covers additional dynamics testing done using the absorbers and their success. The large damping present in the test absorber is the most significant drawback encountered in the current experimental setup. It is demonstrated how the transfer functions shift for decreasing absorber electromagnetic stiffness. This shows how the anti-node can shift providing the minimum response for different excitation frequencies.

Future Work

Two primary tasks follow the research presented here. First, to improve this electromagnetic absorber, the mechanical damping must be reduced. This could be in an entirely different design or in refining the current design. This could also consist of adding additional mass to the absorber to reduce the effective damping ratio. This will allow more cancellation because of lower absorber damping.

Secondly, the control law needs to be developed and implemented to provide the minimum response for a specified frequency range. This control law selected will depend on the experiment situation that is addressed. One possible example is transient machinery startup, where the cancellation frequency should track the running speed.

Summary

The theory has been developed to determine the electromagnetic field and force available for an electromagnetic absorber. An electromagnetic absorber is shown how it can impact system transfer functions to yield a lower system response. It is demonstrated that the semi-active mode with a

variable gap can be used to significantly alter the transfer function and minimize the primary system response.

References

[1] Frahm, H. "Device for Damping Vibrations of Bodies," US Patent No. 989958, 1911.

[2] Wang K. W., and J. S. Lai. "Control of an Adaptable Dynamic Absorber for Transient Vibration Suppression," *Proceedings of the Second Conference on Recent Advances in Active Control of Sound and Vibration*. 1993, 506-515.

[3] Zimmerman, D. C and D. J. Inman. "On the Nature of the Interaction Between Structures and Proof-Mass Actuators," *Journal of Guidance*, Vol. 13, 1990, No. 1, 82-88.

[4] Zimmerman, D. C., G. C. Horner, and D. J. Inman. "Microprocessor Controlled Force Actuator," *Journal of Guidance and Control*, Vol. 11. May-June 1989, 230-235.

[5] Nagaya, K. and N. Arai. "Analysis of a Permanent Magnet Levitation Actuator with Electromagnetic Control," *Journal of Dynamic Systems, Measurement, and Control*. September 1991, 113, 472-478.

[6] Nagaya, Kosuke and Mitsunori Sugiura. "A Method for Obtaining a Linear Spring for a Permanent Magnet Levitation System Using Electromagnetic Control," *IEEE Transactions on Magnetics*, 31, 3, May 1995, 2332-2338.

[7] Waterman, E. H. "Vibration Absorber with Controllable Resonance Frequency." US Patent 4,724,923, Issued February 16, 1988.

[8] Leibovich, Gregory. "Proportional Permanent Magnet Force Actuator," US Patent 4928028. Issued May 22, 1990.

[9] Ormondroyd, J., and den Hartog, J. P. "The Theory of the Dynamic Vibration Absorber," *Transactions of the ASME*, 1928, 49/50 A9-A22.

[10] Thomson, William T. *Theory of Vibration with Applications*, Third Edition, 1988.

[11] Korenev, Boris G. and Leonid M. Reznikov. *Dynamic Vibration Absorbers: Theory and Technical Applications*. Wiley, 1993.

[12] Einstein, George and Krzysztof Wernerowski. "Multi-mass Absorbers Effective in Wide Frequency Band," *Vibration Isolation, Acoustics and Damping in Mechanical System*, ASME, DE-Vol 62, 1993, 43-50.

[13] Sun, J. Q., M. R. Jolly, and M. A. Norris. "Passive, Adaptive and Active Tuned Vibration Absorbers -- A Survey," *Transactions of the ASME*, 117, June 1995, 234-242.

[14] Soom, A and Lee, Ming-san. "Optimal Design of Linear and Nonlinear Vibration Absorbers for Damped Systems," *Journal of Vibration, Acoustics, Stress, and Reliability in Design*. 105. January 1983. 112-119.

[15] Özgüven, H. N. and B. Çandir. "Suppressing the First and Second Resonances in Beams by Dynamic Vibration Absorbers," *Journal of Sound and Vibration* (1986) 111 (3), 377-390.

[16] Kobayashi, H. and S. Aida. "Development of a Houde Damper Using Magnetic Damping," *Design Engineer, vol 62, Vibration Isolation, Acoustics, and Damping in Mechanical Systems*, ASME, 1993.

[17] Yamashita, S. and K Seto. "Vibration and Noise control using dual dynamic absorbers with magnetic damping," *Electromagnetic Force and Application*, J. Tani and T. Takagi (editors), 1992, 489-492.

[18] Yamashita, S., K. Sawatari, and K. Seto. "Vibration Control of a Piping System by Dual Dynamic Absorbers," American Society of Mechanical Engineers, Pressure Vessels and Piping Division (Publication) PVP. Publ by American Soc of Mechanical Engineers (ASME), New York, NY, USA. v 179. 117-122.

[19] Takita, Y. and K. Seto. "An Investigation of adjustable pendulum-type vibration controlling equipment (semi-active vibration control by application of an anti-resonance point)." American Society of Mechanical Engineers, Pressure Vessels and Piping Division (Publication) PVP. Publ by American Soc of Mechanical Engineers (ASME), New York, NY, USA. v 179. 109-115.

[20] Moyka, Ana S. *Adaptive Vibration Absorber*. Virginia Polytechnic Institute and State University Thesis. 1996.

[21] Walsh. P. L. and J. S. Lamancusa. "A Variable Stiffness Vibration Absorber for Minimization of Transient Vibrations," *Journal of Sound and Vibration* (1992) 158 (2), 195-211.

[22] Hubbard, Mont and Donald Margolis. "The Semi-Active Spring: Is it a Viable Suspension Concept?" *ASME Intersociety Conference on Transportation*. 4. 1976. 1-7.

[23] Ryan, Matthew W., Matthew Franchek, and Robert Bernhard. "Adaptive-Passive Vibration Control of Single Frequency Excitations Applied to Noise Control," *Proceedings of Noise-Con 94*. 461-466.

[24] Slavicek, Jan and J. G. Bollinger. "Design and Application of a Self-Optimizing Damper for Increasing Machine Tool Performance," *Advances in Machine Tool Design and Research: Proceedings of the Tenth International Machine Tool Design and Research Conference*. 1969. 71-81.

[25] Buhr, C., M. A. Franchek, and R. J. Bernhard. "Non-collocated Adaptive-Passive Vibration Control," *Journal of Sound and Vibration* (1997) 206 (3), 371-298.

[26] Karnopp, D., M. J. Crosby, and R. A. Harwood. "Vibration Control Using Semi-Active Force Generators," *Journal of Engineering for Industry*. May 1974. 619-626.

[27] Hrovat, Davorin, Pinhas Barak, and Michael Rabins. "Semi-Active Verses Passive or Active Tuned Mass Dampers for Structural Control," *Journal of Engineering Mechanics* (1983) 109, 691-705.

[28] Tanaka, N. and Y Kirushima. "Impact Vibration Control Using a Semi-Active Damper," *Journal of Sound and Vibration* (1992) 158 (2) 277-292.

[29] Rakheja, S. and S. Sankar. "Vibration and Shock Isolation Performance of a Semi-Active 'On-Off' Damper," Journal of Vibration, Acoustics, Stress and Reliability in Design, Vol 107, October 1985, 398-403.

[30] Hrovat, D., D. L. Margolis and M. Hubbard. "An Approach toward the Optimal Semi-Active Suspension." *Journal of Dynamics Systems, Measurement, and Control*. September 1988, Vol. 110, 288-296.

[31] Miller, Lane R. "Tuning Passive, Semi-Active, and Fully Active Suspension Systems," *Proceedings of the 27th Conference on Decision and Control*, IEEE, December 1988, 2047-2053.

[32] Stephens, L. S., K. E. Rouch, and S. G. Tewani. "Theory for an Active Dynamic Vibration Absorber," DE- Vol 34, *Structural Vibration and Acoustics*, ASME 1991, 89-94.

[33] Seto, K., K. Sawatari, and Y. Takita. "Vibration Control of Mechanical Structures by an Active Dynamic Absorber with a Software Control System," 147-153.

[34] Seto, K. and K. Sawatari. "Active Dynamic Absorber with Electromagnetic Force and its Vibration Control Effort," *Electromagnetic Forces and Applications*, 485-488.

[35] Heilmann, John. *A Dual Reaction-Mass Dynamic Vibration Absorber for Active Vibration Control*. Virginia Polytechnic Institute and State University Thesis, 1996.

[36] Burdisso, R. A. and J. D. Heilmann. "A New Dual-Reaction Mass Dynamic Vibration Absorber Actuator for Active Vibration Control," *Journal of Sound and Vibration* (1998), 214(5), 817-831.

[37] von Flotow, Andreas H., Andrew Beard, and Don Bailey. "Adaptive Tuned Vibration Absorbers Tuning Laws, Tracking Agility, Sizing, and Physical Implementations," *Proceedings of Noise-Con 94*. 437-454.

[38] Bonesho, James A and John G Bollinger, 'Theory and Design of a Self-optimizing Damper." *Advances in Machine Tool Design and Research: Proceedings of the Seventh International Machine Tool Design and Research Conference*. 1966. 229-241.

[39] Bonesho, James A and John G Bollinger. "Dual Variable Self-Optimizing Vibration Damper Theory." *Advances in Machine Tool Design and Research: Proceedings of the Ninth International Machine Tool Design and Research Conference*. 1968. 635-646.

[40] Sato, Y. "Dynamic Absorber Using a Hollow Rotor Partially Filled with Liquid," *JSME International Journal Series*, 1990, Vol. 33, 135-140.

[41] Okada, Y., K. Matsuda, and H Hashitani. "Self-sensing Active Vibration Control using the Moving-Coil-Type Actuator," *Journal of Vibrations and Acoustics*, Vol 117, October 1995, 411-415.

[42] Chang, James C. H. and Tsu T. Soong. "Structural Control Using Active Tuned Mass Dampers," *Journal of the Engineering Mechanics Division*, December 1980, 1091-1098.

[43] Nishimura, Isao, et al. "An Intelligent Tuned Mass Damper (An Experimental Study of an Active-Passive Composite Tuned Mass Damper)," *Proceedings of AIAA/ASME Structures, Structrual Dynamcis, and Materials Conference*, 1993, 3561-3569, AIAA-93-1709-CP.

[44] Olgac, Najat and Brian T. Holm-Hansen. "A New Direction in Active Vibration Absorption: Delayed Resonator," DSC-VOL 50/PED-Vol 63, *Symposium on Mechatronics*, ASME 1993, 15-20.

[45] Olgac, Nejat and Brian T. Holm-Hansen. "Design Characteristics of a Novel Tunable Active Vibration Absorber," DE-Vol 75, *Active Control of Vibration and Noise*, ASME 1994. 477-483.

[46] Sommerfeldt, Scott D. and Jiri Tichy. "Adaptive Control of a Two-stage Vibration Mount," *Proceedings of the 27th Conference on Decision and Control*, December 1988, 2039-2044.

[47] Sommerfeldt, Scott D. and Jiri Tichy. "Adaptive Control of a Two-stage Vibration Isolation Mount," *Journal of the Acoustical Society of America* 88 (2), August 1990, 938-944.

[48] Hyde, T. Tupper and Eric H. Anderson. "Actuator with Built-In Viscous Damping for Isolation and Structural Control," *AIAA Journal*, Vol. 34, No. 1, January 1996, 129-135.

[49] Okada, Y. and R. Okashita. "Adaptive Control of an Active Mass Damper to Reduce Structural Vibration," American Society of Mechanical Engineers, Pressure Vessels and Piping Division (Publication) PVP. Publ by American Soc of Mechanical Engineers (ASME), New York, NY, USA. v 179. p 129-133.

[50] Craik, Derek. *Magnetism: Principles and Applications*. Wiley, 1995.

[51] Woodson, Herbert H and James R Melcher. *Electromechanical Dynamics, Part II: Fields, Forces, and Motion*. Wiley, 1968.

[52] Thomson, William T. *Theory of Vibration with Applications*, Third Edition, 1988, 43.

[53] Craik, Derek. *Magnetism: Principles and Applications*. Wiley, 1995, 111.

[54] Thomson, William T, Theory of Vibration with Applications, Third Edition, 1988, p 406-407.

VITA

Lawrence B. Tentor was born to Richard and Arundel Tentor on March 2, 1968 in Schenectady, New York. He grew up in Niskayuna, New York, where he pursued computers, pole vaulting, and alpine skiing as his activities of greatest interest. He spent his undergraduate years (1986-1990) in Buffalo, New York at the State University of New York at Buffalo earning a Mechanical Engineering degree and pursuing leadership activities in Theta Chi Fraternity. His graduate work began in 1990 at Virginia Tech due to its faculty reputation in dynamic systems. In order to provide funding during his graduate years he was trained and sold educational books with the Southwestern Company. This lead to a two year full time appointment as a Field Sales Manager. After this he returned to complete his graduate studies in Mechanical Engineering and undertake a Master's program in Finance. Funding was provided for Teaching Assistant activities and engineering consulting with Durability, Inc. He has now entered the financial modeling arena where he applies advanced mathematics to solve valuation problems in the energy trading business.